Fiber Optics Point-Source for Digital Holographic Microscopy Lensless

Brayan de Jesús Patiño Jurado

Universidad Nacional de Colombia

Facultad de Ciencias, Escuela de Física

Medellín, Colombia

2019

Fiber Optics Point-Source for Digital Holographic Microscopy Lensless

Brayan de Jesús Patiño Jurado

Tesis presentada como requisito parcial para optar al título de:
Magister en Ciencias - Física

Supervisor:
Ph.D. Juan F. Botero Cadavid

Línea de Investigación:
Óptica
Grupo de Investigación:
Óptica y Procesamiento Opto-Digital

Universidad Nacional de Colombia
Facultad de Ciencias, Escuela de Física
Medellín, Colombia
2019

A mis padres

Resumen

El trabajo investigativo llevado a cabo para la producción de esta tesis de maestría tiene como objetivo fundamental el desarrollo de una alternativa tecnológica al sistema de iluminación *pinhole* comúnmente empleado en microscopía holográfica digital sin lentes (MHDSL). El sistema de iluminación *pinhole* tiene como principal problema el alto costo de asociado a la complejidad de su fabricación e implementación. Como alternativa de solución el desarrollo de una fuente puntual a fibra óptica para MHDSL es detalladamente descrito a lo largo de este trabajo.

El desarrollo de fuentes puntuales a fibra óptica para MHDSL propuesto se basa en la creación de extremos conificados en fibras ópticas convencionales. En el análisis geométrico de la apertura numérica de dichas fibras ópticas con extremos cónicos se presenta una metodología de diseño modelada por una ecuación paramétrica, la cual permite sintonizar la apertura numérica como función del ángulo de conicidad de la punta de la fibra. Adicionalmente, se propone y se evalúa un método de fabricación por ataque químico, en el cual se consideran los efectos de largos períodos de difusión de ácido fluorhídrico en una capa de protección de aceite con el objetivo de producir puntas cónicas en fibras ópticas con ángulos grandes y con buen acabado superficial.

Un análisis en simulación de trazado de rayos y de propagación ondulatoria, permite comprobar la dependencia de la apertura numérica con el ángulo de conicidad de la punta de las fibras ópticas.

Se presenta, además, la evidencia experimental donde se acopla luz de un láser a las fibras ópticas modificadas y se evalúa la apertura numérica. Finalmente, se realiza una completa caracterización de la resolución y las fibras ópticas cónicas son exitosamente implementadas como fuentes puntuales de ondas esféricas para MHDL.

Palabras clave: Apertura numérica, fuente puntual, fibras ópticas, puntas cónicas, microscopía holográfica digital.

Abstract

The undertaken research work for this thesis dissertation aims for a technological alternative to the pinhole illumination system commonly employed in digital lenseless holographic microscopy (DLHM). This traditional method presents as a main difficulty the high fabrication cost and implementation of a hole of such small dimensions. As an alternative solution to this problem, a point-source based on fiber optics is developed in this work.

Fiber optics based point-source for DLHM here proposed relies on the fabrication of conical tips in conventional optical fibers, In the analysis of the dependency of the numerical aperture on the conical geometry of the cone tips a simple and compact design equation to tailor the numerical aperture of the cone-shaped optical fibers is presented. Additionally, a chemical etching fabrication method and model that considers the long term diffusion effects of hydrofluoric acid on a protective oil layer is proposed and the scope is to obtain tapered tips with very smooth surface and large conical angles.

Ray tracing and wave propagation studies were carried out and allowed us to prove the numerical aperture ability to be tailored and dependency on the cone angle of a step-index optical fiber.

The results of this studies were experimentally confirmed by coupling laser light into the chemically etched cone tips and measuring the numerical aperture. Finally, these cone tips were implemented as point sources of spherical waves for DLHM. The resolution characterization of the DLHM with cone tips was carried out. The results were very encouraging and supported the viability of the cone tips fiber as a technological alternative to the pinhole illumination system for DLHM.

Keywords: Numerical aperture, point-source, fiber optics, cone tips, digital holographic microscopy.

Contents

List of figures

Pág.

List of symbols and abbreviatures

Symbols with Latin letters

Symbol	Term	Units SI	Definition
C	Speed of light in vacuum	$\dfrac{\text{m}}{\text{s}}$	Equation (2.6)
N	Refractive index	1	Equation (2.7)
k_0	Wavenumber of the vacuum	$\dfrac{1}{\text{m}}$	Section 2.2
B	Normalized propagation constant	1	Equation (2.35)
L	Coherence length	M	Equation (2.47)
D	Diffusion coefficient	$\dfrac{\text{m}^2}{\text{s}}$	Equation (4.1)
M	Molar mass	$\dfrac{\text{mol}}{\text{m}^3}$	Section 4.1
G	Gravitational acceleration	$\dfrac{\text{m}}{\text{s}^2}$	Section 4.1
K	Rate of reaction	$\dfrac{\text{m}}{\text{s}}$	Section 4.1
P	Pressure	$\dfrac{\text{N}}{\text{m}^2}$	Section 4.1
F	Volume force	$\dfrac{\text{N}}{\text{m}^3}$	Section 4.1

Symbols with Greek letters

Symbol	Term	Units SI	Definition
μ_0	Permeability of the vacuum	$\dfrac{\text{F}}{\text{m}}$	Section 2.1.1
ε_0	Permittivity of the vaccum	$\dfrac{\text{H}}{\text{m}}$	Section 2.1.1
ω	Angular frequency	$\dfrac{\text{rad}}{\text{s}}$	Section 2.1.1

Symbol	Term	Units SI	Definition
κ_0	Wavenumber of the vacuum	$\frac{1}{m}$	Section 2.1.1
β	Wave vector	$\frac{1}{m}$	Equation (2.3)
α	Attenuation coefficient	$\frac{dB}{m}$	Section 2.2
ν	Normalized frequency	1	Section 2.2
λ	Wavelength	m	Section 1.1
ρ	Density	$\frac{kg}{m^3}$	Section 4.1

Subscripts

Subscript	Term
eff	Effective
cl	Cladding
co	Core
max	Maximum
c	Critical
I	Incident
T	Theoretical
E	Experimental

Abbreviatures

Abbreviature	Term
SEM	Scanning electron microscopy
NSOM	Near-field optical scanning microscopy
STM	Scanning tunneling microscopy
AFM	Atomic force microscopy

Abbreviature	Term
DHM	Digital holographic microscopy
DLHM	Digital lensless holographic microscopy
PSTM	Photon scanning tunnelling microscope
ESTM	Electron scanning tunnelling microscopy
NA	Numerical Aperture
SMF	Single mode fiber
MMF	Multimode fiber
HF	Fluorhydric acid
FWHM	Full width at half maximum

List of tables

Pág.

1. Introduction

1.1 Introduction

In the microscopy realm exploration one of the oldest and most widely spread techniques is the optical microscopy. However, this is subject to a diffraction limit. The maximum resolving power of conventional light microscopes is limited, at the most, to 200 and 500 nm in the lateral and axial planes, respectively [1]. However, around the middle of the 20th century a series of discoveries laid the foundation for modern microscopy techniques, which allowed information under 200 nm to be detected. Among these methods are included: Near-field optical scanning microscopy (NSOM) [2], [3], Scanning electron microscopy (SEM) [4], Atomic force microscopy (AFM) [5], and Scanning tunneling microscopy (STM) [6]. Over recent decades, fundamental principles were established for the fluorophore localization microscopy technique, which provides a powerful tool for understanding the dynamic of biology at the nanometer scale via fluorescence [7].

These super-resolution microscopy techniques are, however, generally limited to take two-dimensional images. This means that three-dimensional phenomena can not be completely described using these techniques. One example of these kind of undescribed realms is the dynamic evolution of biological specimen at the micrometer and nanometer scale, since the microorganisms inhabit a three-dimensional world. This becomes more critical when the sample is fast moving in its environment, since three-dimensional view of the samples implies taking images in real time.

The problem of the three-dimensional (3-D) visualization of biological specimens has been addressed by a technique of microscopy developed over the last decades, the digital holographic microscopy (DHM). This technique of microscopy allows 3-D images of tissues and living cells to be obtained in their environment in a non-intrusively manner, based on

the information obtained from the phase and the amplitude of the object's wavefront, which is digitally recorded in a hologram [8].

To realize digital holographic microscopy two systems are required: an optical system to obtain the hologram, and a digital system to reconstruct the taken image. In particular, in a special configuration of DHM called digital lensless holographic microscopy, using an in-line configuration, just a point-source light and a digital registry system are the only elements required to obtain both phase and amplitude information of the microscopic specimen [9].

Optimizing each of the systems that comprise the digital lensless holographic microscopes has been a technological challenge around which a wide field of research has been developed over recent decades. Particularly in the case of the light source, illumination of the specimen with spherical waves is required to obtain the magnification of the diffraction pattern in the recording process of the hologram [10]. The traditional way to produce these spherical waves involves using a monochromatic light source, usually a laser of wavelength λ, that is focused into a pinhole of linear dimensions of the order of λ. Although in theory, the pinhole illumination system is a very simple method to generate spherical waves, in practice, the implementation of this system in DLHM is very cumbersome. In addition to the difficulties and their high manufacturing costs, the main experimental difficulty with pinholes arises from the rigorous alignment process needed to ensure spherical waves generation, which many times requires the use of ultra-precision opto-mechanical elements [11]. In response to these difficulties and taking advantage of the good features of the fiber optics such as the installation flexibility, low cost, and the relative ease of coupling light, a shaped optical fiber tip as illumination source for Digital Lensless Holographic Microscopy is developed in this work.

1.2 Background

Fiber optics have been incorporated in many different research fields during the last two decades. The telecommunications booming has resulted not only in a growing interest of doing research and development in this area, but also in alternative applications of the optical fibers as sensor and light sources. The versatility of the optical fibers is due among others, to features such as their good overall durability, low weight, installation flexibility, possibility of remote sensing, low decay due to corrosion, temperature resistance, and electromagnetic interference immunity [12]. Furthermore, thanks to its wide use in

telecommunications, optical fibers have decreased in cost as well as increased their accuracy, composition, and precise dimensions.

An optical fiber end tip, or simply a fiber tip, is an optical microsystem shaped on the end of an optical fiber which is used to modify the manner in which light behaves while interacting with the surrounding environment at the end of the fiber [13]. By modifying the geometry of the distal end of a cylindrical optical fiber in which the light of a monochromatic laser is being propagated, it is possible to adjust how light emerges from this tip to the surrounding environment. Light emerges from the the optical fiber in such a way that said distal end can be implemented as a point-source of spherical waves [14]. In this respect, a wide variety of methods have been reported to alter the geometry of the fiber optics ends. These include mechanical processes [15]–[18], thermal processes [19], laser processing [20], [21] and chemical etching processes [22]–[27].

Shaped optical fiber tips are versatile and useful to change how light behaves at the ends of the optical fibers. Therefore, much research has been undertaken on fiber tips which in turn has motivated the development of numerous medical and industrial applications. These include, but are not limited to, material processing, laser ablation of body tissue, light coupling in communication links, microscopy, and spectroscopy [28]. The most common fiber tips are cone, ball, helical groove, and angled tips. The main functions of these fiber tips can include: increase the spot size [29], increase or decrease the light divergence (lenses) [30], achieve omnidirectional illumination (360°) through the sides of the fiber tip [31], redirect light sideways, and increase or reduce back reflection .

Some microscopy techniques have incorporated cone-shaped optical fibers as scanning probe. In particular, the Near-field scanning optical microscopes (NSOM) are designed so that a cone tip fiber probe scans the sample by illuminating a nanometric local area, and the transmitted or reflected light in the near field zone is then detected [3], [15], [18], [24], [26], [32]–[35]. Another microscopy technique called Photon scanning tunnelling microscope (PSTM) is analogous to the Electron scanning tunnelling microscopy (ESTM), with the difference that PSTM involves tunnelling of photons instead of electrons from the sample surface to the probe tip. In this form of microscopy, the distribution of the evanescent field is produced by the effect of total internal reflection, modulated by the sample and detected into a tapered optical fiber probe [36]–[38].

In referring to digital lensless holographic microscopy (DLHM), an exhaustive search of literature related to the development and implementation of a point-source based on fiber optics did not match any articles; with the exception of the doctoral dissertation referenced in [39]. Although that dissertation includes a full chapter on fiber sources for digital holographic microscopy, an in-depth analysis is not presented for the dependency of neither the numerical aperture, nor the resolution obtained in the registered hologram [6], on the modification of the geometry of the fiber. In addition, no clear and complete experimental results were presented to show the advantages of using cone-shaped optical fiber instead of an illuminated slit as point-source for DLHM. Despite the fact that the above-mentioned work presents poor experimental results in respect of fiber optics as point-source, this constitutes an important starting point since it has been identified that in order to implement fiber optics as illumination sources for DLHM, it is needed to develop techniques that increase the numerical aperture of the fiber.

A design methodology to tailor the numerical aperture of step-index optical fiber is precisely the main objective that is addressed in this dissertation. Thus, this monograph presents the mathematical and physical preliminaries of the light propagation and the principles involved in holography and DLHM, followed by the analytical, geometrical, and simulation analysis of the numerical aperture dependency on the conical geometry of the fiber.

2. Fiber Optics and Theory of Digital Holographic Microscopy

2.1 Mathematical Preliminaries

2.1.1 Wave Nature of Light

The wave behavior of the light is governed by a set of four equations, which were formulated by James Clark Maxwell in 1865 [40]. In their differential form, and in the absence of charges and currents, these equations are:

$$\nabla \times \vec{E} = -\mu \frac{\partial \vec{H}}{\partial t}, \tag{2.1}$$

$$\nabla \cdot \vec{E} = 0, \tag{2.2}$$

$$\nabla \times \vec{H} = \varepsilon \frac{\partial \vec{E}}{\partial t}, \text{ and} \tag{2.3}$$

$$\nabla \cdot \vec{H} = 0; \tag{2.4}$$

where $\vec{E}$ is the electric field vector, $\vec{H}$ is the magnetic field vector, μ the permittivity, and ε the permeability of the medium of propagation.

Under the assumptions that the medium of propagation is linear, homogeneous, isotropic, non-dispersive, and non-magnetic, the behavior of the individual components of the electric and magnetic fields are identical. Thus, the Maxwell equations can be reduced to a single scalar wave equation:

$$\nabla^2 U(x,y,z,t) - \frac{n^2}{c^2} \frac{\partial^2 U(x,y,z,t)}{\partial t^2} = 0 \tag{2.5}$$

where $U(x, y, z, t)$ is any of the scalar field components, c is the speed of the electromagnetic wave in the vacuum, and it is defined as:

$$c = \sqrt{\frac{1}{\mu_0 \varepsilon_0}}.$$
(2.6)

n is the refraction index of the medium and it is defined as:

$$n = \sqrt{\frac{\varepsilon}{\varepsilon_0}}.$$
(2.7)

Here μ_0 and ε_0 are, respectively, the permeability and permittivity of the vacuum.

For a monochromatic wave, the scalar field component may be represented as:

$$. U(x, y, z, t) = R\{\widetilde{U}(x, y, z) e^{-i\omega t}\}.$$
(2.8)

With ω being the angular frequency of the wave. $\widetilde{U}(x, y, z)$ can be expressed as:

$$\widetilde{U}(x, y, z) = |U(x, y, z, t)| e^{i\phi(x, y, z)},$$
(2.9)

where $|u(x, y, z, t)|$ and $\phi(x, y, z)$ are the amplitude and the phase of the wave, respectively.

By substituting the Equation (2.9) into the Equation (2.8) and subsequently substituting the resultant equation into Equation (2.5), the following time-independent equation is obtained:

$$\nabla^2 \widetilde{U}(x, y, z) - k^2 \widetilde{U}(x, y, z) = 0..$$
(2.10)

Here $k = \frac{n\omega}{c}$ is called the wavenumber and the Equation (2.10) is known as the Helmholtz equation.

2.1.2 Scalar Diffraction Theory

The phenomenon of diffraction, which is the apparent bending of light at boundary interfaces, can be studied from a scalar theory. This formulation is an approximation that dismisses the vectorial nature of the electromagnetic field, and by doing so, the field satisfies the Helmholtz equation, Equation (2.10).

The problem of diffraction through an aperture in an opaque screen is a phenomenon of great interest in optics, and particularly in holography. A form of illustrating the diffraction of a spherical wave through an aperture is by using the Huygens' principle. According to this

principle, every point on a wavefront becomes a secondary source of spherical wavelets. All these wavelets give the form of the diffracted wave at any given time, as illustrated in Figure 2-1. Mathematically, the problem of finding the complex position function of the scalar field, $\widetilde{U}(x,y,z,) = |U(x,y,z,t)|e^{i\phi(x,y,z)}$, at a particular point in space after the wave has diffracted through an aperture can be analyzed from the Green's theorem:

$$\iiint_V \left(\widetilde{U}\nabla^2\widetilde{G} - \widetilde{G}\nabla^2\widetilde{U}\right)dV = \iint_S \left(\widetilde{U}\frac{\partial\widetilde{G}}{\partial n} - \widetilde{G}\frac{\partial\widetilde{U}}{\partial n}\right)dS, \tag{2.11}$$

where $\widetilde{G}$ is also a complex function of position, V is a volume surrounded by a closed surface S, and $\frac{\partial}{\partial n}$ is a partial derivative in the outward normal direction of the surface.
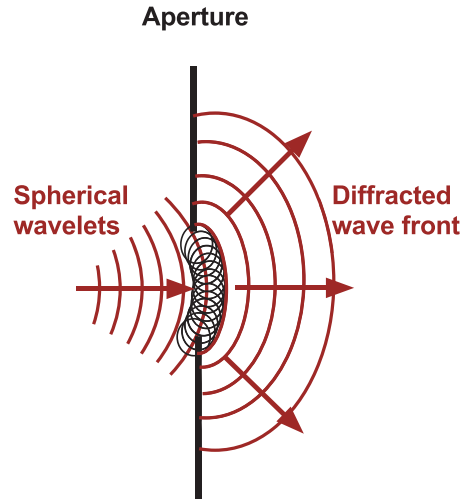
Aperture

Figure 2-1: A spherical wave diffracts through an aperture. The shape of the diffracted wave is illustrated using the Huygens' principle.

According the Green's theorem, to find $\widetilde{U}$ a suitable selection of the Green's function $\widetilde{G}$ should be carried out. In particular, Gustav Kirchhoff chose as Green's function an spherical wave of unit amplitude and radius R:

$$\widetilde{G} = \frac{e^{ikR}}{R}. \tag{2.12}$$

The analysis of diffraction through an aperture, denoted as Σ, in an opaque screen using the Green's theorem is shown in Figure 2-2. In this situation, the chosen surface S has been divided into two components: a planar surface S_1 lying on the aperture, and a spherical cap of radius ρ, S_2, centered on the point of observation $\rho_0 = (x_0,y_0,z_0)$. The Green's

functions for S_1 and S_2 in this case corresponds to $\tilde{G}(\rho_1) = \frac{e^{ikr_{01}}}{r_{01}}$ and $\tilde{G} = \frac{e^{ikR}}{R}$. Here $r_{ij} = |\rho_j - \rho_i|$ is the magnitude of the vector that connects the points j and i. Furthermore, with the Kirchhoff's boundary conditions, $\tilde{U}$ and $\frac{\partial \tilde{U}}{\partial n}$ are zero in the opaque region on the screen, and assuming that illumination of the aperture is a spherical wave:

$$\tilde{U}(\rho_1) = \frac{Ae^{ikr_{21}}}{r_{21}}. \tag{2.13}$$

The solution of the surface integrals on the right hand side of Equation (2.11) yields to what is known as the 'Fresnel-Kirchhoff diffraction formula' [41]:

$$\tilde{U}(\rho_0) = \frac{A}{i\lambda} \iint_\Sigma \frac{e^{ik(r_{21}+r_{01})}}{r_{21}r_{01}} \left(\frac{\cos(\vec{n}, r_{01}) - \cos(\vec{n}, r_{21})}{2} \right) ds. \tag{2.14}$$

Where $\cos(\vec{n}, r_{ij})$ represents the cosine of the angle between outward normal $\vec{n}$ and the vector $r_{ij} = \rho_j - \rho_i$, which connects the points j and i.
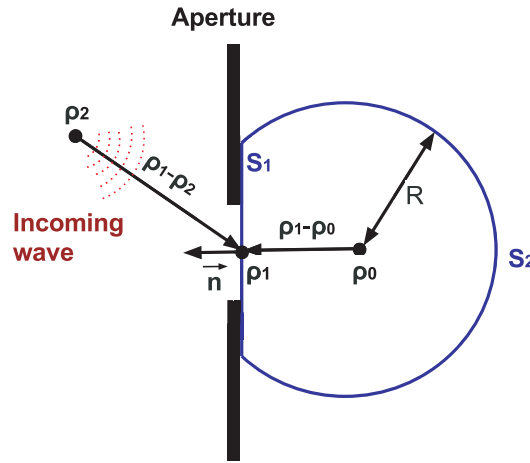
Figure 2-2:   The geometry of Kirchhoff formulation to diffraction through an aperture.

Kirchhoff formulation is a commonly employed approach in digital holographic applications [9], [10], [42]–[45]. However, this formulation presents a mathematical inconsistency when both the field and its normal derivative are assumed zero at the opaque plane boundary. In order to avoid this inconsistency, an alternative formulation can be used. The Rayleigh-Sommerfeld formulation which solves the inconsistencies in the Kirchhoff boundary conditions. This approach assumes illumination at the aperture by simultaneous spherical waves generated at point ρ_0 and at a mirror image of this point on the other side of the

aperture ρ'_0 , as shown in Figure 2-3. These point sources can oscillate in phase (+) or with a phase difference of π, (−), resulting in the following Green's function:

$$\tilde{G}(\rho_1) = \frac{e^{ik\,r_{01}}}{r_{01}} \pm \frac{e^{ikr_{01}}}{r_{01}}.$$

(2.15)
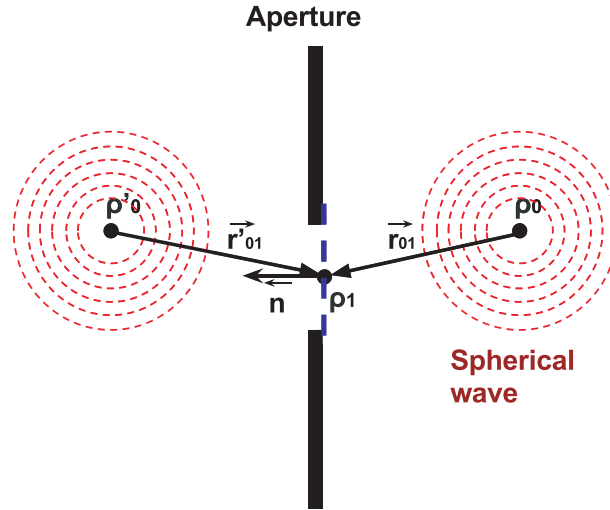
Aperture

Figure 2-3:   The Rayleigh-Sommerfeld formulation of diffraction by an aperture.

One of these Green's functions can be used in the Equation (2.11) to solve $\tilde{U}(\rho_0)$, resulting in the Rayleigh-Sommerfeld integral:

$$\tilde{U}(\rho_0) = \frac{1}{i\lambda} \iint_\Sigma \tilde{U}(\rho_1) \frac{e^{ikr_{01}}}{r_{01}} \cos(\vec{n}, r_{01}) ds.$$

(2.16)

Where $\cos(\vec{n}, r_{01})$ is the cosine of the angle between outward normal $\vec{n}$ and the vector which connects the center of the aperture and the point of observation. $\tilde{U}(\rho_1)$ is any scalar field at the aperture corresponding to an spherical wave diverging from a point source at position ρ'_0. With $\tilde{U}(\rho_1)$ expressed as the Equation (2.13) and assuming that this integral can be written as follows:

$$\tilde{U}(\rho_0) = \frac{A}{i\lambda} \iint_\Sigma \frac{e^{ikr_{21}+ikr_{01}}}{r_{01}r_{21}} \cos(\vec{n}, r_{01}) ds.$$

(2.17)

Complete details of this formulation can be found in Chapter 3 of reference [41].

2.1.3 Fresnel Diffraction and Fraunhofer Diffraction

Fresnel's and Fraunhofer's diffraction integrals are derived in this section. In these approximations the screen and observation planes are assumed planar and parallel. Firstly, according to the Fresnel-Huygens principle Equation (2.17) can be written as [41]:

$$\widetilde{U}(\rho_0) = \iint_\Sigma h(\rho_0, \rho_1)\widetilde{U}(\rho_1)ds, \tag{2.18}$$

where

$$h(\rho_0, \rho_1) = \frac{1}{i\lambda}\frac{e^{ikr_{01}}}{r_{01}}\cos(\vec{n}, r_{01}). \tag{2.19}$$

With the assumption that the dimensions of the aperture a and the observation region are much smaller than the observation distance $r_{01} = |\rho_1 - \rho_0|$, the oblique factor can be approximated by $\cos(\vec{n}, r_{01}) \cong 1$ and the quantity r_{01} in the denominator is approximated to z ($r_{01} \cong z$). Under these conditions the weighting function can be written as follows:

$$h(\rho_0, \rho_1) = \frac{1}{i\lambda}\frac{e^{ikr_{01}}}{z}. \tag{2.20}$$

It is important to note that the quantity r_{01} in the exponent cannot be approximated to z since the error that introduces this approximation increases exponentially it can induce to errors greater than 2π. Instead, to approximate r_{01} a series expansion can be used:

$$r_{01} = \sqrt{(x_0 - x_1)^2 + (y_0 - y_1)^2 + z^2} = z \cdot \sqrt{\left(\frac{x_0 - x_1}{z}\right)^2 + \left(\frac{y_0 - y_1}{z}\right)^2 + 1} \tag{2.21}$$

$$\cong z\left[1 + \frac{1}{2}\left(\frac{x_0 - x_1}{z}\right)^2 + \frac{1}{2}\left(\frac{y_0 - y_1}{z}\right)^2\right].$$

Then function h, also called impulse response, can be rewritten as:

$$h(\rho_0, \rho_1) = \frac{1}{i\lambda z}e^{ikz}e^{\frac{ik}{2z}[(x_0 - x_1)^2 + (y_0 - y_1)^2]}. \tag{2.22}$$

This impulse response function is called the 'Fresnel approximation' and gives rise to what is known as Fresnel-Frauhofer diffraction formula:

$$\widetilde{U}(\rho_0) = \frac{e^{ikz}}{i\lambda z}e^{\frac{ik\rho_0^2}{2z}} \iint_\Sigma e^{\frac{ik(x_1^2 + y_1^2)}{2z}}\widetilde{U}(\rho_1)e^{\frac{-ik(x_0 x_1 + y_0 y_1)}{2z}}dx_1 dy_1. \tag{2.23}$$

This equation can be further reduced introducing the Fraunhofer approximation that states:

$$z >> \frac{k\rho_1^2}{2} = \frac{k(x_1^2 + y_1^2)}{2}.$$

Fraunhofer approach describes the behaviour of diffracting light in the far-field.. Thus, Equation (2.23) becomes:

$$\tilde{U}(\rho_0) = \frac{e^{ikz}}{i\lambda z} e^{\frac{ik\rho_0^2}{2z}} \iint_{\Sigma} \tilde{U}(\rho_1) e^{\frac{ik(x_0 x_1 + y_0 y_1)}{2z}} dx_1 dy_1. \qquad (2.24)$$

which is the Fraunhofer diffraction integral.

2.1.4 Spatial Frequencies Analysis

Images can be analyzed in the Fourier domain, which is also known as frequency-space. According to the Fourier theorem, any signal can be expressed as a sum of simple sine waves with different frequencies and can also be decomposed into its composite frequencies by taking the Fourier transform of the signal [46]. Mathematically, a two-dimensional (2D) Fourier transform ($\mathcal{F}$) can be taken of an image leading to a 2D representation of the spatial frequencies of the image k_x and k_y:

$$\mathcal{F}(k_x, k_y) = \int_{-\infty}^{\infty} \int_{-\infty}^{\infty} f(x,y) e^{-i2\pi(k_x x + k_y y)} dx dy. \qquad (2.25)$$

Here high spatial frequencies correspond to spatial changes in the image, such as edges of the object, and low spatial frequencies correspond to bulk areas of similar intensity in the image.

The numerical aperture is a dimensionless value that characterizes the range of angles over which the system can accept or emit light from a specimen. This value is defined as:

$$NA = n \sin \theta, \qquad (2.26)$$

where n is the index of refraction of the medium and θ is the half-angular width of the maximum cone of light captured by the system. In an optical system, the ability to capture spatial frequencies is defined through the optical transfer function (OTF). This is a Fourier function in coordinates k_x and k_y, and is also dependent on the numerical aperture (NA). The OTF describes the resolution of the optical system Δr as [46]:

$$\Delta r = \frac{2\pi}{\Delta k_T}. \qquad (2.27)$$

Here $r = (x, y)$ and $k_T = (k_x, k_y)$. For an ideal system with no aberrations, $\Delta k_T = 2k\theta$. By applying the paraxial approximation, $sin\theta \sim \theta$, and recalling the definition for the wavenumber, $k = \frac{2\pi}{\lambda}$, the numerical aperture expressed in terms of spatial bandwidth is given by:

$$. NA = \frac{n\lambda\Delta k_T}{4\pi}. \tag{2.28}$$

Making a substitution for Δk_T, the spatial resolution of an imaging system is expressed as:

$$\Delta r = \frac{\lambda}{2NA}. \tag{2.29}$$

Equation (2.29) expresses what is known as diffraction-limited resolution.

2.2 Fiber Optics

A fiber optics is a cylindrical waveguide made of dielectric materials such as silica glass. It consists of a central core, in which the light is guided, surrounded by an outer cladding of a material with a slightly lower refractive index, as shown in Figure 2-4. In this, light beams incident on the interface between the core and cladding at angles greater than the critical angle undergo total internal reflection and are guided through the core without suffering refraction [12].
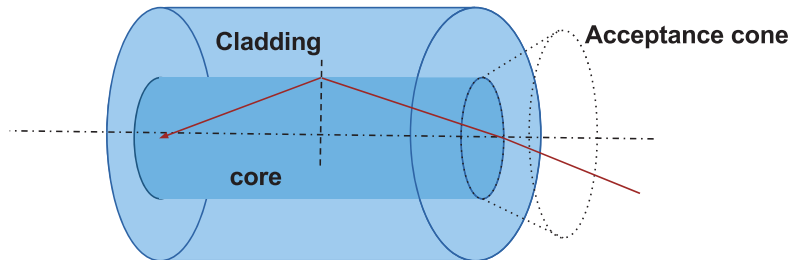
Figure 2-4:   Scheme of an optical fiber.

Optical waveguides can be divided into various types, according to structure (planar, cylindrical, birrefringent), number of modes (single or multimode), refractive index profile (step-index or gradient-index fiber), material (glass, plastic or semiconductor), dispersion (natural dispersion, dispersion shifted fiber DSF, dispersion widened fiber DWF) and polarization (classic, polarizing optical fiber) [47], [48].

Considering the number of propagating modes, optical fibers can be divided into single-mode or multimode fibers. The fiber geometry and composition determine the discrete set of electromagnetic fields that can propagate through the fiber. These set of electromagnetic fields can be calculated using Maxwell equations and adequate boundary conditions. The solutions obtained using Maxwell equations are Bessel functions, while boundary conditions arise from the characteristic equation for propagation constant β [49].

Solutions of the Maxwell equations for Transversal Electric (TE)-modes can be obtained assuming the waveguide dimension along the y-axis is infinite, the light propagates along the z-axis and wave field is restricted only in the direction of the x-axis. Therefore all derivatives with respect to y equal zero, thus

$$H_y = E_x = E_z = 0. \tag{2.30}$$

$$\frac{\partial^2 E_y}{\partial x^2} + h^2 E_y = 0. \tag{2.31}$$

$$h^2 = \gamma^2 + n^2 \kappa_0^2 = 0 \quad \text{where} \quad \gamma = \alpha + i\beta. \tag{2.32}$$

In this last equation, α represents attenuation. In addition, propagation constant, β, has the physical meaning of a wave vector and it is of crucial importance for electrodynamics analysis of modal propagation in fiber optics. This quantity is given by:

$$\beta = \frac{\omega}{v} = \frac{2\pi}{\lambda} = \kappa_0 n_{\text{co}} \sin \theta, \tag{2.33}$$

where κ_0 represents the wavenumber in vacuum, n_{co} is the core refractive index and θ is the incident angle at the core-cladding interface.

Solving with the proper boundary conditions of continuity for E_y and derivative $\frac{\partial E_x}{\partial x}$ at the core-cladding interface, the normalized frequency can be obtained:

$$v = \frac{h_0}{2} \sqrt{n_1^2 + n_2^2} = 2 \sqrt{\frac{1}{1 - B}} \left[\frac{m\pi}{2} + \arctan \sqrt{\frac{B}{1 - B}} \right] \quad m = 0, 2, 4, 6. \ldots \tag{2.34}$$

In the anterior expression, B represents the normalized propagation constant given by:

$$B = \frac{n_{\text{eff}}^2 - n_2^2}{n_1^2 - n_2^2}. \tag{2.35}$$

With $n_{\text{eff}} = \frac{\beta}{\kappa_0}$ and n_2 the cladding refractive index.

Single mode fibers (SMF): The normalized frequency condition $0 < v < \pi$ is satisfied. These fibers are typically characterized by a core diameter ranging from 5 to 10 μm in the wavelength range of telecommunications (1300 to 1600 nm), and from 4 to 6 μm for the visible range (380 to 720 nm).

Multimode fibers (MMF): The normalized frequency condition $v > \pi$ is satisfied. These fiber optics are characterized by a core diameter from 50 to 62,5 μm in the wavelength range of telecommunications (1300 to 1600 nm).

2.3　Holography

2.3.1 Principles of Holography

Holography is a process where a light field is captured and reproduced [41]. In the capture stage, also known as 'writing' the hologram, the amplitude and phase of an electromagnetic wave scattered off, or diffracted by, an object is recorded. This is achieved by illuminating the object with a coherent light source and interfering the resulting scattered or diffracted light with a mutually coherent reference beam, to finally record the resulting interference pattern [50], as illustrated in Figure 2-5. Classical holography records the interference pattern on holographic film. On the other hand, digital holography records the pattern on a charge-coupled device (CCD) or a metal-oxide semiconductor (CMOS) chip [51].
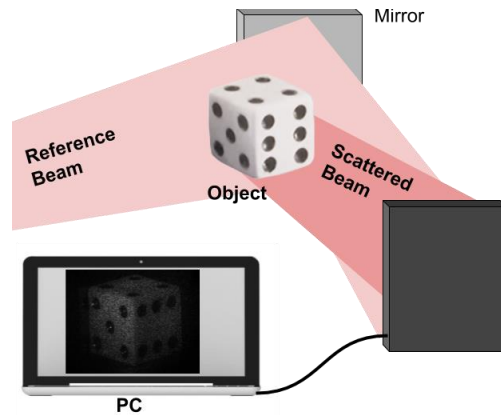
Figure 2-5:　　The principle of recording a hologram.

In general, if it is considered that the light emanating from the object and the reference source obey the time-independent Helmholtz equation, Equation (2.10). Then, the object and reference waves can be defined, respectively, as [52]:

$$\bar{A}_O(x,y,z,) = |A_O(x,y,z)|e^{i\phi_O(x,y,z)} \tag{2.36}$$
$$\bar{A}_R(x,y,z,) = |A_R(x,y,z)|e^{i\phi_R(x,y,z)}.$$

where ϕ_O and ϕ_R are the respective phase factors.

The intensity on the hologram plane is the intensity of the superposition of these two waves:

$$I_H(x_H, y_H, z_H) = |\bar{A}_O(x_H, y_H, z_H) + \bar{A}_R(x_H, y_H, z_H)|^2 \qquad (2.37)$$
$$= |A_O(x_H, y_H, z_H)|^2 + |A_R(x_H, y_H, z_H)|^2$$
$$+ \bar{A}_O^*(x_H, y_H, z_H)\bar{A}_R(x_H, y_H, z_H) + \bar{A}_O(x_H, y_H, z_H)\bar{A}_R^*(x_H, y_H, z_H).$$

Here the subscript H identifies the points in the hologram plane and the asterisk indicates the complex conjugate function associated.

On the other hand, in the reproducing stage, also known as 'reading' the hologram, the hologram is reconstructed into an image by extracting the term $\bar{A}_O$. In this procedure, the interference pattern that contains the information of phase and amplitude is decoded to obtain the three-dimensional image of the object. If classical holography is developed, the obtained film is illuminated from the opposite side with the same light source in order to reconstruct the object beam. Mathematically, this implies [52]:

$$I_H(x_H, y_H, z_H)\bar{A}_R^*(x_H, y_H, z_H) = |A_O(x_H, y_H, z_H)|^2 \bar{A}_R^*(x_H, y_H, z_H) \qquad (2.38)$$
$$+ |A_R(x_H, y_H, z_H)|^2 \bar{A}_R^*(x_H, y_H, z_H)$$
$$+ \bar{A}_O^*(x_H, y_H, z_H)|A_R(x_H, y_H, z_H)|^2$$
$$+ \bar{A}_O(x_H, y_H, z_H)\bar{A}_R^{2*}(x_H, y_H, z_H).$$

In this result, the third term corresponds to a real image in the position of the original object that the viewer can observe [41].

In digital holography, however, multiplication the intensity on the hologram by the reference beam is not required. Most techniques treating the hologram as an aperture and applying scalar diffraction theory in a numerical environment [42].

2.3.2 In-line Holography

This configuration is referred to as Gabor holography and it allows partially coherent light to be used instead of a fully coherent source [53]. The setup used in recording and reconstructing in-line holograms is shown in Figure 2-6. The scattered beam from the object interferes with the reference beam, forming an interference pattern that incides directly on the recording plane. Subsequently, the obtained hologram is illuminated from the opposite

side with the same reference beam in order to reconstruct the object beam. The approaches to the Equation (2.38) are discussed below.
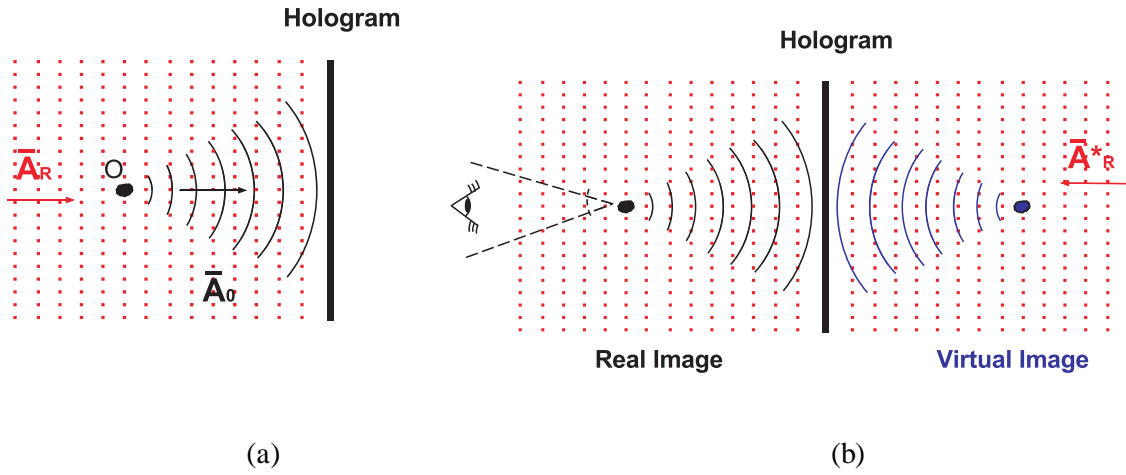
Figure 2-6:   Setup used in (a) recording and (b) reconstructing in-line holograms.

The first term, $|A_R(x_H, y_H, z_H)|^2$, corresponds to the background and it is related to the un-diffracted illumination beam. The second term, $|A_O(x_H, y_H, z_H)|^2$, corresponds generally to noise. For its part, the third term is a focused real image and the four term corresponds to an out-of-focus virtual image. These real and virtual images are superimposed on the digital hologram and it is not easy to separate them. Generally a spatial or temporal phase-shifting method is required [41]. This problem could increase the error in localizing objects along the direction of the optical axis. However, by introducing a small angular separation between the two interfering beams in an off-axis configuration, the focused real and out-of-focus virtual images are separated as shown below.

2.3.3 Off-axis Holography

In off-axis holography the reference beam is set at an angle with respect to the scattered beam. Figure 2-7 illustrates one possible setup for capturing and reconstructing the off-axis hologram. At the recording plane, the sum of two mutually coherent beams is observed, one representing the scattered beam from the object and the other the reference beam.

In particular, the reference beam could be a plane wave with a phase factor which includes the angle θ that it makes relative to the scattered beam [52], $\bar{A}_R(x_H, y_H, z_H) = |A_R(x_H, y_H, z_H)|e^{-ikx\sin\theta}$. In this way, the captured intensity at the recording plane is :

$$I_H(x_H, y_H, z_H) = |A_O(x_H, y_H, z_H)|^2 + |A_R(x_H, y_H, z_H)|^2 \tag{2.39}$$
$$+ \bar{A}_O^*(x_H, y_H, z_H)|A_R(x_H, y_H, z_H)|e^{-ikx\sin\theta}$$
$$+ \bar{A}_O(x_H, y_H, z_H)|A_R(x_H, y_H, z_H)|e^{-ikx\sin\theta}.$$

According to this, a linear phase shift along the x-axis of the recording plane is introduced by the effect of the angle of the scattered beam θ relative to the reference beam.

In the reconstruction, the obtained hologram is illuminated at the same angle with the same reference beam in order to separate the real and virtual images. From Equation (2.39), the reconstruction of the third term produces a real image that is deflected away from the reference beam axis at an angle θ. Likewise, the reconstruction of the fourth term produces a virtual image that is deflected away from the reference beam axis at an angle $-\theta$.

(a)   (b)
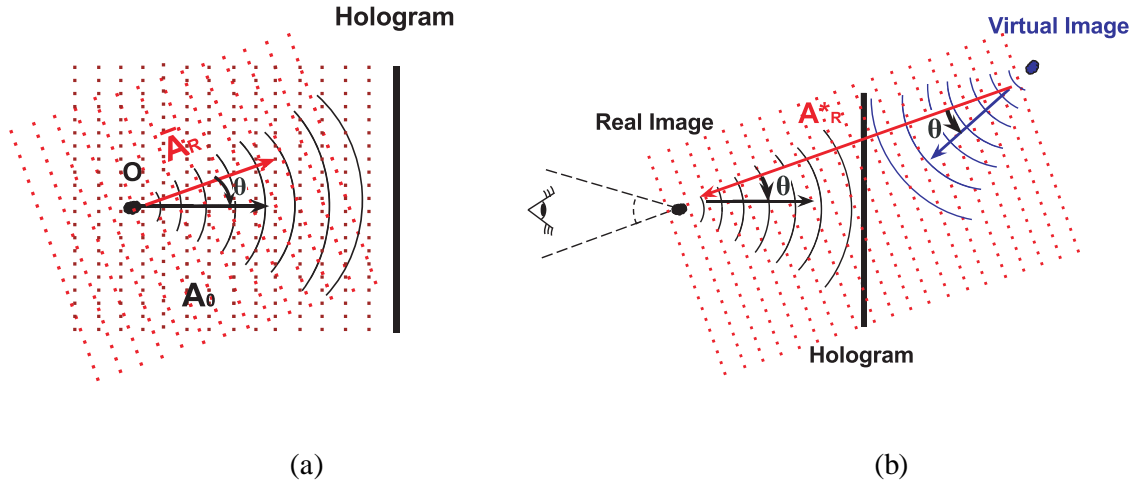
Figure 2-7:   Setup used in (a) recording and (b) reconstructing of an off-axis holograms.

2.4 Digital Lensless Holographic Microscopy

2.4.1 Introduction

In-line holography with spherical waves using a lensless configuration was first proposed by Gabor over 60 years ago, as a new lensless imaging method in electron microscopy [53]. This technique is widely used in optical holography[54], digital microscopy[43], [44], [51], [55], electron microscopy[56], and soft x-ray holography [57]. In particular, the use of digital lensless holographic microscopy (DLHM), which is an in-line architecture, in biology has enabled to obtain 3D images with resolution in the micrometer range in applications

such as underwater observations of biological processes such as the kinematics and dynamics of swimming microorganisms [9], [11], [43].

As previously mentioned, the in-line configuration causes scattered and reference waves to propagate in the same direction, thus producing a superposition of the reconstructed real image and out-of-focus virtual image. This issue is usually called 'twin image problem' in holography [42], [58]. However in DLHM, the utilization of spherical illumination can guarantee the absence of the twin-image problem. In fact, as is demonstrated in [9], for DLHM the twin image does not represent a problem.

In this subsection the technical details about DLHM are presented. In the first part, the most important aspects about the setup for the recording and the descriptive process of the reconstruction of the hologram are discussed. In the second part, the considerations about the illumination source for DLHM are presented.

2.4.2 Record and Reconstruction

DLHM arrangement is based on the classic holographic principle described in the previous section. Figure 2-8 depicts the schematic of one in-line setup for digital lensless holographic microscopy. A laser is focused onto a pinhole producing spherical waves of wavelength λ that illuminate an object located typically a distance of a few thousand wavelengths from the source and forms a highly magnified diffraction pattern on a screen where the hologram recording is performed by a digital sensor, e.g. a CCD or a metal oxide semiconductor camera [42].
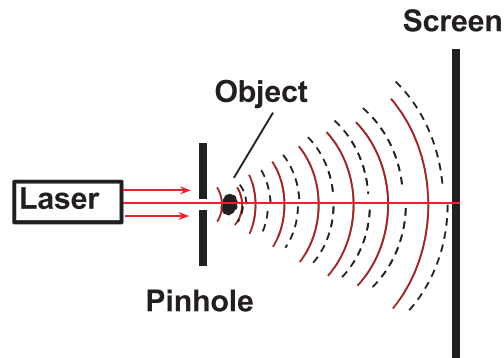
Figure 2-8:   Schematic of DLHM. Image adapted from reference [9].

As described in section 2.3, the intensity on the hologram plane, located in the digital screen, is the intensity of the superposition of two waves: the unscattered reference wave $A_R(r)$, and the wave scattered by the object $A_O(r)$. The intensity recorded by the digital screen with no object present, $|A_R(r)|^2$, is pixel-wise subtracted from the in-line hologram to produce a new intensity $\tilde{I}$ which corrects, at least in part, the effect of the emission cone of the point source [9]:

$$\tilde{I}(r) = |A_R(r) + A_O(r)|^2 - |A_R(r)|^2 \tag{2.40}$$
$$= [A_R(r)A_O^*(r) + A_R^*(r)A_O(r)] + |A_O(r)|^2.$$

In this equation, the bracket in the second line is the holographic diffraction pattern because it is formed from the superposition of the interference terms between the unscattered reference wave and the scattered wave from the object. The second term in the same equation corresponds to the interference between the scattered waves.

Once the hologram is recorded by the digital screen, the wave scattered by the sample, $A_O(r)$, is recovered by computing numerically the diffraction that a spherical wavefront undergoes as if it was illuminated with an intensity $\tilde{I}$ [44]. In this process of the reconstruction the 3-D structure of the object is obtained from the two-dimensional (2-D) hologram on the screen. Mathematically this 3-D structure can be achieved via the Fresnel—Kirchhoff diffraction integral, Equation (2.14), which when written to represent the wavefront propagation in DLHM turns into [45]:

$$A_O(r') = \int_{\text{screen}} \tilde{I}(r) e^{\frac{ikr'\cdot r}{|r|}} d^2r. \tag{2.41}$$

Where $r = (x, y, z)$ represents a point on the digital screen, placed at a distance L from the point source, and $r' = (x', y', z)$ is a point on the reconstruction plane. $A_O(r')$ is numerically calculated by the discretization of the modified hologram in $M \times N$ pixels. Thus Equation (2.41) becomes [59], [60]:

$$A_0(s\Delta x', t\Delta y', z) = \Delta x''\Delta y'' \cdot \exp[ik(s^2\Delta x''\Delta x' + t^2\Delta y''\Delta y')/2L]$$
$$\cdot \sum_{m=-M/2}^{M/2-1} \sum_{n=-N/2}^{N/2-1} \tilde{I}''(m\Delta x'', n\Delta y'')$$
$$\cdot \exp[ik(m^2\Delta x''\Delta x' + n^2\Delta y''\Delta y')/2L]$$
$$\cdot \exp\left[-\frac{ik(s - m^2\Delta x''\Delta x' + t - n^2\Delta y''\Delta y')}{2L}\right].$$

(2.42)

In this equation, $\tilde{I}''(m\Delta x'', n\Delta y'')$ is an interpolated intensity on a spherical-like grid with pixels of size $\Delta x'' \times \Delta y''$. $m, n, s,$ and t are integer numbers that denote the discrete coordinates in the interpolated and reconstruction planes [45]. This equation represents a discrete and scalable convolution that allows the calculation of the scattered complex amplitude $A_0(s\Delta x', t\Delta y', z)$ via three fast Fourier transforms. A comprehensive explanation of this algorithm developed to evaluate $A_0(r)$ can be read in [60].
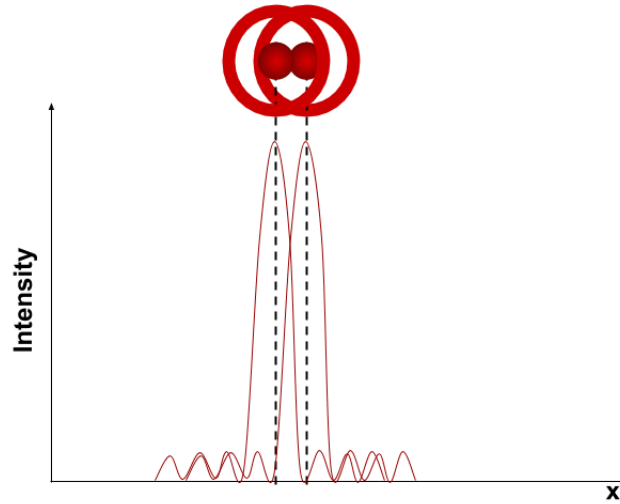
Figure 2-9:   The Rayleigh Criterion.

2.4.3 Resolution in DLHM

According to the Rayleigh criterion, two point sources are just resolved when the first diffraction maximum of one source coincides with the first diffraction minimum of the other source, as it is illustrated in Figure 2-9. In the case of DLHM, as can be read in [9], this criteria is applied by taking as a model an ideal point source that emits a spherical wave,

written as $A_{\mathrm{R}}(\vec{r}) = \frac{A_{\mathrm{r}}e^{ikr}}{r}$, and two objects at positions $\vec{r}_1$ and $\vec{r}_2$, also modeled as point sources, as shown in Figure 2-10 (a). Thus, the total wave field is:

$$A(\vec{r}) = A_{\mathrm{r}}\frac{e^{ikr}}{r} + A_1\frac{e^{ik|\vec{r}-\vec{r}_1|}}{|\vec{r}-\vec{r}_1|} + A_2\frac{e^{ik|\vec{r}-\vec{r}_2|}}{|\vec{r}-\vec{r}_2|}. \tag{2.43}$$

and therefore, the intensity of the contrast image is

$$\tilde{I}(\vec{r}) = A^2(\vec{r}) - \frac{A_{\mathrm{r}}^2}{r^2} = \frac{A_1^2}{|\vec{r}-\vec{r}_1|^2} + \frac{A_2^2}{|\vec{r}-\vec{r}_2|^2} + 2\frac{A_1 A_2}{|\vec{r}_1-\vec{r}_2|^2}\cos[k(|\vec{r}-\vec{r}_1| - |\vec{r}-\vec{r}_2|)]$$
$$+ \left\{\frac{2}{r}\frac{A_{\mathrm{r}}A_1}{|\vec{r}-\vec{r}_1|}\cos[k(r - |\vec{r}-\vec{r}_2|)] + \frac{2}{r}\frac{A_{\mathrm{r}}A_1}{|\vec{r}-\vec{r}_2|}\cos[k(r - |\vec{r}-\vec{r}_2|)]\right\}. \tag{2.44}$$

In this equation, the first two terms account for the scattering from isolated objects variating smoothly the background. The third term represents the interference from the two objects, the classical interference from two point sources, and the term in curly brackets represents the holographic interference. This last term accounts for the interference between the source and each object. Note that for the holographic term to be more prominent in Equation (2.44), amplitudes A_1 and A_2 of the scattered waves must be much smaller than the amplitude of the reference wave A_{r}, so that the terms with A_1^2 and A_2^2 are negligible. This condition is ensured for small objects when $A_1, A_2 << A_0$. In addition, since $|\vec{r}-\vec{r}_1|$ and $|\vec{r}-\vec{r}_2|$ are of comparable length in a typical DLHM setup, the positions on the recording screen are perpendicular to the optical axis that connects the source with the center of the screen, and assuming for simplicity that the objects are located symmetrically from the optical axis and on a line parallel to the screen, so that $|\vec{r}_1| = |\vec{r}_2|$ as shown the Figure 2-10 (b), the Equation (2.44) becomes:

$$\tilde{I}(\vec{r}) = \frac{4}{r}\frac{A_{\mathrm{r}}A_1}{|\vec{r}-\vec{r}_1|}\cos\left[\frac{k}{2}(2r - |\vec{r}-\vec{r}_1| - |\vec{r}-\vec{r}_1|)\right]\cdot\cos\left[\frac{k}{2}(|\vec{r}-\vec{r}_1| - |\vec{r}-\vec{r}_2|)\right] \tag{2.45}$$

In this equation the identity $\cos(a) + \cos(b) = 2\cos[(a+b)/2]\cdot\cos[(a-b)/2]$ has been used. The second cosine term produces the modulation of the holographic interference pattern and has maxima when its argument is $2\pi m$. To recover the necessary information from this term it is required that at least the the zeroth- and first-order maxima are recorded on the screen. Thus, for the first-order maximum, $m = 1$,

(a)

(b)
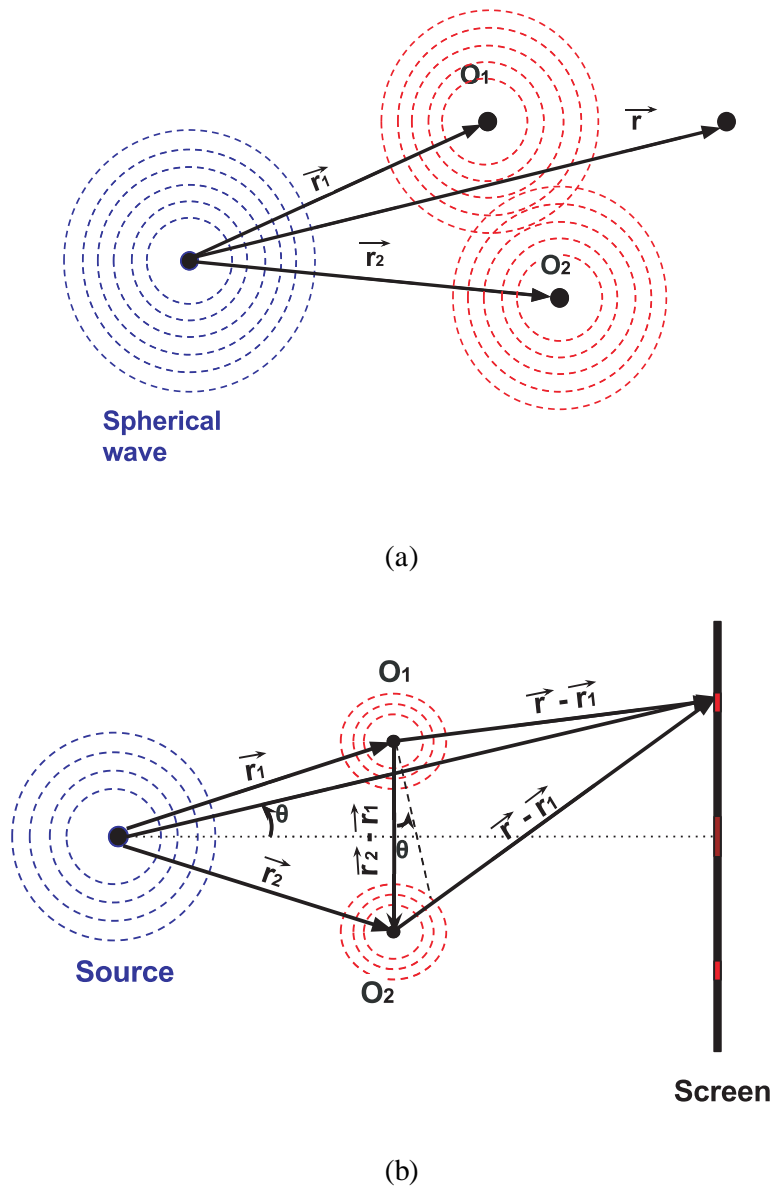
Figure 2-10:   (a). The model to study the problem of the resolution in DLHM. (b) The model taking into account some approaches.

$$\frac{k}{2}(|\vec{r} - \vec{r_1}| - |\vec{r} - \vec{r_2}|) = 2\pi$$
$$\Rightarrow |\vec{r} - \vec{r_1}| - |\vec{r} - \vec{r_2}| = 2\lambda,$$

And according to Figure 2-10 (b), $|\vec{r} - \vec{r_1}| - |\vec{r} - \vec{r_2}| \simeq |\vec{r_2} - \vec{r_1}| \cdot sin\theta$, where $sin\theta = NA$ is the numerical aperture. Hence it follows that two points can be resolved laterally if their lateral separation satisfies

$$|\vec{r_2} - \vec{r_1}| \geq \frac{2\lambda}{NA} \tag{2.46}$$

Note that the resolution is determined by the wavelength and the numerical aperture. In addition, because $|\vec{r} - \vec{r_1}|$ and $|\vec{r} - \vec{r_2}|$ are of comparable lengths, the spatial frequency of the classical interference pattern will be much smaller than the spatial frequency of the holographic interference terms in Equation (2.44). This implies that to obtain a high-resolution reconstructed image it is necessary to record the fine spatial details of the hologram.

Another factor which must be taken into account to obtain a high-resolution is the pinhole size. For the pinhole to act as a point source for a coherent spherical wave, its size must be of the order of a wavelength [9], which is normally very difficult to achieve.

2.5 Illumination Source

A source of light can be analyzed as a large number of individual emitters, each of which emits for only a brief period of time producing wave-trains of finite length. The average length of the wave-trains emitted is referred to as the coherence length [61]. The coherence length L of an illumination source is related to its spectral width Δf, (in other words, its range of frequencies) and to the speed of light c, according the following expression:

$$L = \frac{c}{\Delta f} \tag{2.47}$$

White light has a very broad range of frequencies and thus a very short coherence length, on the order of microns. For its part, lasers are light sources nominally monochromatic and therefore, they can have very long coherence lengths on the order of kilometers [62].

The coherence length determines the spatial coherence. However, another concept related to coherence is the temporal coherence. A monochromatic source is necessarily temporally

coherent, because temporal coherence means that there is a fixed relationship between two beams of the light emitted in different times [63]. The coherence has a critical role in the interference principle since for any two interfering beams of a light source, the path difference between the two beams must be less than the coherence length and the light source must be monochromatic for the interference to be observed.

The coherence length is related to the measure of the depth of field of the DLHM. In conventional imaging with lens, as described in [64], the depth of field is related to all object points within a certain range of distance from the lens that are imaged with acceptable sharpness in a given image-plane. Thus, in lens-based microscopy the depth of field is limited to $2\Delta r^2/\lambda$, where Δr is the spatial resolution limited given by Equation (2.29). Note that according to this expression, a very small depth of field implies a very high resolution, because Δr is small. Then two points can be resolved in depth if:

$$\Delta r \geq \frac{\lambda}{2(NA)^2}.$$

(2.48)

For DLHM the depth of field corresponds to the maximum distance between the object of a given diameter and the hologram plane for which a satisfactory diffraction pattern can be recorded [42]. The depth of field can be restricted in digital holography by using a broadband light source [64]. Such a source has a correspondingly short coherence length according to Equation (2.47).

Another factor which must be taken into account to choose an illumination source for DLHM is its state of polarization. To achieve optimal interference, because the contrast of the interference pattern is influenced by the polarization states of the two beams [64], both the reference and object beams should be identically polarized. This is achieved in in-line holography by ensuring the laser light source is linearly polarized.

In DLHM the illumination source is a laser, as shown in the Figure 2-8 which ensures that the illumination is coherent (monochromatic). The laser is focused onto a pinhole constituting a point light source for a spherical wave. However, as mentioned previously, for the pinhole to act as a point source for a coherent spherical wave, its size must be of the order of a wavelength. A larger pinhole leads to a reduction of the spatial coherence and narrows the zero-order emission cone used to form the holographic interference pattern of emitted light. The numerical aperture of the emission cone of a pinhole can be obtained by numerically evaluating the Fresnel integral for a circular pinhole. After evaluating this

integral, the results show that the numerical aperture of the emission cone is 0.77 and 0.29 for pinholes with diameters of λ and 4λ, respectively [9],.

This work aims for a technological alternative to the pinhole illumination system in DLHM, since this traditional method presents as a main difficulty the implementation of a hole of such small order of magnitude. In the following chapters of this thesis the development and evaluation of a point-source based on fiber optics for DLHM is described. The next chapter presents the analytical, geometrical, and simulation study of the numerical aperture dependency on the conical geometry of the fiber.

3. Numerical Aperture of Cone-shaped optical fibers

Numerical aperture (NA) is a dimensionless parameter which measures the range of angles over which an optical system can accept or emit light. In the case of optical fibers, the NA indicates the capabilities of the optical fiber to gather and/or to emit light. In general, it is wanted to have an optical fiber with the largest possible NA to guarantee the largest accepting or emitting cones of light; thus, optimizing its use. As for the case of step-index optical fibers, the numerical aperture is determined by the refractive index of the core n_{co} and the cladding n_{cl}, namely $\mathrm{NA} = n \sin\theta = \sqrt{n_{co}^2 - n_{cl}^2}$, where θ is half of the angle of light emission or gathering and n is the refractive index of the surrounding medium. Consequently, the only way to have that largest possible NA is by maximizing the difference between the refractive indexes of the core and the cladding. Commercially, ultra-high NA optical fibers are limited up to 0.35, a figure that can be quite small for many applications [65]–[68].

Different options have been proposed to increase the NA of an optical fiber. The most common of these options are photonic-crystal fibers [69]–[71], as well as cone-shaped optical fibers [72]–[74]. In the former, the NA is increased by raising the effective refractive index of the core. In the latter, the distal end of the optical fiber is geometrically modified to obtain a cone-shaped optical fiber [69]. Owing to the elaborated engineering process used to produce photonics-crystal fibers, cone shaping is the most accessible method to increase the NA of optical fibers. Multiple techniques have been reported to modify the geometry of the optical fiber tip; these include mechanical [15]–[17], [75], thermal [19], laser-aided [20], [21] , and chemical etching processes [22]–[26], [76], [77].

Despite the great spectrum of applications of cone-shaped optical fibers [3], [15], [24], [28], [72], [78], up to the best knowledge of the authors there has not been an in-depth analysis on how the geometry of the distal end of the optical fiber is linked to the NA; Only a brief description has been reported elsewhere [39]. For this reason, this section aims to present an analysis of the numerical aperture of the cone-shaped optical fibers. In the first subsection of this work, a step-index optical fiber with conical end, used as illumination source or light gathering system, is modeled and a ray tracing study is performed in order to obtain an analytical expression that linked the numerical aperture with the angle of the cone-shaped tip of the step-index optical fiber. Once this geometrical analysis has been made, the designed cone-shaped optical fiber was numerically modeled using both ray-tracing and wave optics methods to test for the forecasted NA.

3.1 Geometric Analysis

3.1.1 Numerical Aperture in a Step Index Fiber
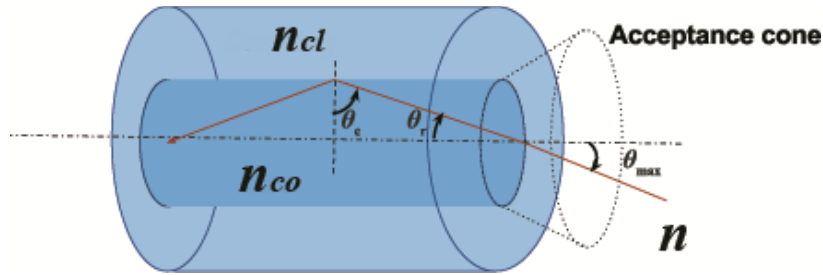
Figure 3-1:   Acceptance cone in an optical fiber.

The light that is launched in a step index fiber optics can propagate through the fiber only if it enters the fiber within a certain cone, known as the acceptance cone, as shown in Figure 3-1. When the light is incident from the medium of refractive index n to the core of index n_{co} at the acceptance angle θ_{max}, the Snell's law applied at the medium-core interface for this situation is:

$$n \sin\theta_{max} = n_{core} \sin\theta_r \qquad (3.1)$$

From the geometry in the Figure 3-1,

$$\theta_r = 90 - \theta_c$$

Here the critical angle θ_c is

$$\theta_c = \arcsin\left(\frac{n_{cladding}}{n_{core}}\right) \tag{3.2}$$

Substituting θ_r in Equation (3.1) gives

$$n\sin\theta_{max} = n_{core}\sin(90 - \theta_c) = n_{core}\cos\theta_c$$

By squaring both sides yields

$$n^2 \sin^2\theta_{max} = n_{core}^2\cos^2\theta_c = n_{core}^2(1 - \sin^2\theta_c) = n_{core}^2\left[1 - \left(\frac{n_{cladding}}{n_{core}}\right)^2\right]$$

and solving for $n\sin\theta_{max}$ yields

$$n\sin\theta_{max} = \sqrt{n_{core}^2 - n_{cladding}^2}$$

In this equation $n\sin\theta_{max}$ is commonly defined as the numerical aperture, **NA**, of the optical system. Then, the NA of step index optical fibers is

$$NA = \sqrt{n_{core}^2 - n_{cladding}^2} \tag{3.3}$$

3.1.2 Analytical Design to Tailor the Numerical Aperture of Cone-Shaped Optical Fibers

The numerical aperture $NA = n \sin \beta$ demands an unambiguous definition of the angle β as the light is gathered or emitted. In the case of cone-shaped optical fibers aimed to be used as illumination sources, β is the angle measured with respect to the cone axis of the refracted-out ray in the core-surrounding medium interface, as illustrated in Figure 3-2. For sake of simplicity, only the sagittal plane is represented. A coarse light-ray analysis on this plane shows that the angle β varies according to the phenomena that the incident ray on that cone-shaped surface suffers; a simple refraction (a), one total internal reflection (b), or multiple total internal reflections (c). These cases are the phenomena that are finally controlled by the incident angle θ_i of the incoming ray over the cone-shaped surface; this latter angle is measured as illustrated in Figure 3-2. In the same figure, one can realize that the incident angle θ_i can be controlled by the semi-angle of the cone tip, α, measured with

respect to the optical axis of the step optical fiber. In summary, the NA, namely the angle β if the fiber is immersed in a refractive index $n = 1$, can be engineered as a function of the semi-angle of the tip in a step optical fiber for each of the phenomena that can take place on the cone-shape surface.

(a)

(b)

(c)
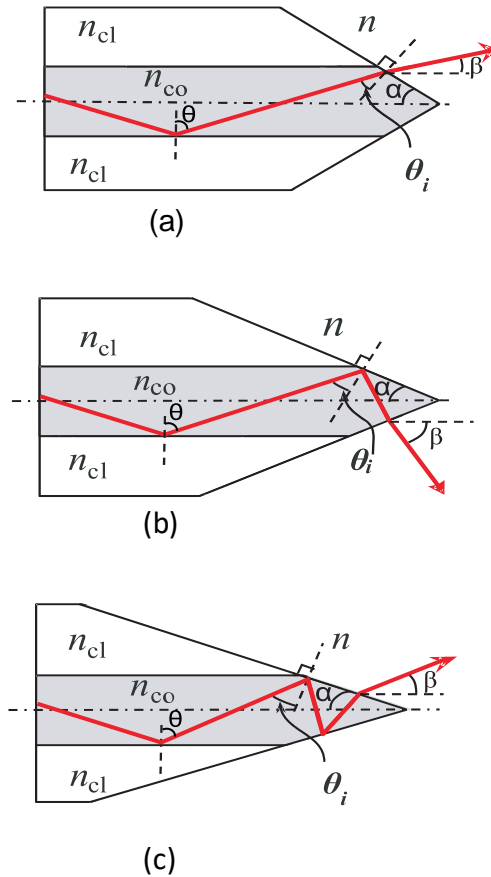
Figure 3-2:   Step optical Fiber with a cone-shaped tip. n, n_{cl} and n_{co} are the refractive indexes of the surrounding medium, the cladding and the core, in that order. A ray incident on the cone-shaped surface can suffer, depending on θ_i, (a) a simple refraction, (b) a total internal reflection, or (c) multiple total internal reflections

For the light to impinge at the cone-shaped surface, initially it must be guided by the step optical fiber. Since the mode coupling could significantly change the characteristics of the light propagating along the fiber, this proposed analytical study can be used only for short fiber lengths (few meters in plastic optical fibers or few hundred of meters in silica optical fibers) [79][80]. In consequence, a step-index optical fiber is considered along this study.

The light guiding is only possible if a total internal reflection takes place at the core-cladding interface. This mandatory condition leads to the rule

$$\theta \geq \theta_c = \arcsin\frac{n_{cl}}{n_{co}}$$

(3.4)

with θ measured as shown in Figure 3-2. The light-ray guided in the optical fiber impinges on the cone-shaped surface at an angle $\theta_i = \theta - \alpha$, which for the limit-case in Equation (3.4) turns into

$$\theta_i = \theta_c - \alpha.$$

(3.5)

On the cone-shaped surface the ray can suffer any of the three formerly said phenomena, which are analyzed in the following subsections. It should be emphasized that a propagated or guided ray undergoes one of the three phenomena depending exclusively on the angle of the cone-shaped surface with no dependence on the size of the illumination at the input facet of the optical fiber.

a.   Simple refraction

Figure 3-3:   Scheme of a cone-shaped step optical fiber with tapered tip at an angle α such that $\alpha > arcsin\,(n_{cl}/n_{co}) - arcsin\,(n/n_{co})$. Under this condition the incident ray suffers a simple refraction at the cone-shaped surface.

In this first case, the light-ray at the cone-shaped surface should impinge at an angle such that it does not experience total internal reflection at the core-medium interface, as shown Figure 3-3, namely

$$\theta_i < \theta_c' = \arcsin \frac{n}{n_{co}}. \tag{3.6}$$

Considering that $\alpha = \theta_c - \theta_i$, the semi-angle of the cone-shaped tip must be

$$\alpha > \theta_c - \theta_c' \tag{3.7}$$

$$\alpha > \arcsin \frac{n_{cl}}{n_{co}} - \arcsin \frac{n}{n_{co}}.$$

Equation (3.7) expresses the angle of the cone-shaped step optical fiber in terms of the index of refraction of the core, the cladding, and the surrounding medium of the step optical fiber, something that is highly wanted in engineering. Now, to connect the cone-shaped angle α with the numerical aperture $NA = n \sin \beta$, requires Snell´s law to be applied at the core-medium interface, which can be expressed as

$$\sin(\theta_c - \alpha) = n \sin\left(\frac{\pi}{2} - \beta - \alpha\right), \tag{3.8}$$

which after some algebra allows the numerical aperture for a cone-shaped step optical fiber with a tip angle $\alpha > \arcsin n_{cl}/n_{co} - \arcsin n/n_{co}$ to be expressed as

$$NA(\alpha) = n \cos\left\{\alpha + \arcsin\left[\frac{n_{co}}{n} \sin\left(\arcsin \frac{n_{cl}}{n_{co}} - \alpha\right)\right]\right\}. \tag{3.9}$$

NA
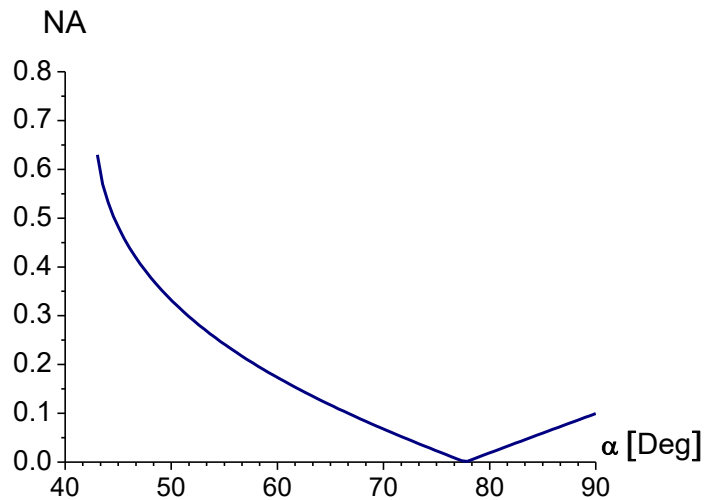
Figure 3-4:   Plot of NA vs. semi-angle α for a commercial single-mode fiber Thorlabs SM600 with a cone-shaped such that $\alpha > arcsin(n_{cl}/n_{co}) - arcsin(n/n_{co})$.

In Figure 3-4 a plot of Equation (3.9) for a commercial single-mode step optical fiber (Thorlabs SM600, $n_{co} = 1.46147$ and $n_{cl} = 1.45804$), surrounded by air is shown. From this figure, it can be seen that by tuning the angle of the cone-shaped optical fiber from $\alpha = 42.9$ to $\alpha = 90$ degrees, numerical apertures from ranging from 0 to 0.64 can be achieved.

b.   One total internal reflection

As for the case of one total internal reflection on the cone-shaped surface, the incident angle θ_i at ① must fulfill the condition given by

$$\theta_i \geq \theta_c' = \arcsin\frac{n}{n_{co}}. \tag{3.10}$$

Once again, accounting for the fact that $\alpha = \theta_c - \theta_i$, to have one total internal reflection on the surface ①, the semi-angle of the cone-shape tip must be

$$\alpha \leq \theta_c - \theta_c'$$

$$\alpha \leq \arcsin\frac{n_{cl}}{n_{co}} - \arcsin\frac{n}{n_{co}}. \tag{3.11}$$
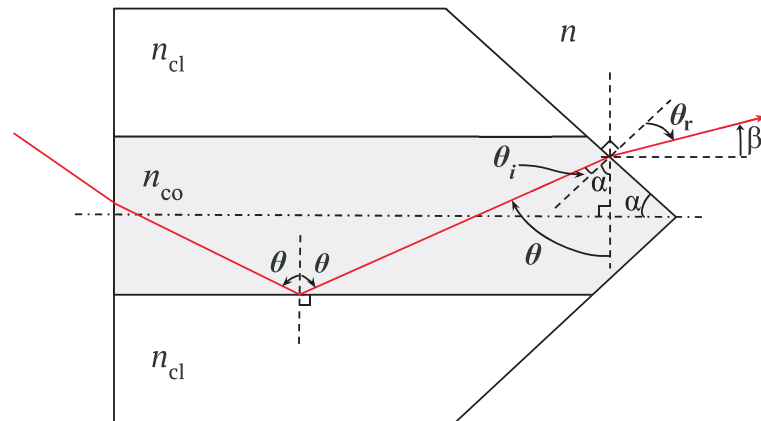

Figure 3-5:   Scheme of a cone-shaped step optical fiber with tapered tip at a semi-angle α such that $\left(\arcsin(n_{cl}/n_{co}) - \arcsin(n/n_{co})\right)/3 < \alpha \leq \arcsin(n_{cl}/n_{co}) - \arcsin(n/n_{co})$. Under this condition the incident ray suffers one total internal reflection on the cone-shaped surface ① and it is refracted out at the cone-shaped surface ②.

After this total internal reflection on the cone-shaped surface ①, the light ray must be refracted out on the cone-shaped surface ②. For this refraction to happen at the core-

medium interface the cone semi-angle α must be chosen such that the incident angle θ_i', see Figure 3-5, fulfills the condition $\theta_i' < \theta_c' = \arcsin n/n_{\mathrm{co}}$. From Figure 3-5, $\theta_i' = \theta' - 2\alpha$ or $\theta_i' = \theta_c - 3\alpha$.

According to this latter expression, the condition $\theta_i' < \theta_c' = \arcsin n/n_{\mathrm{co}}$ is equivalent to:

$$\alpha > \left(\arcsin \frac{n_{\mathrm{cl}}}{n_{\mathrm{co}}} - \arcsin \frac{n}{n_{\mathrm{co}}} \right)/3 \, . \tag{3.12}$$

Equations (3.11) and (3.12) determine the limits that the semi-angle of the cone-shaped tip must fulfill for the guided light- ray to suffer one single internal reflection and thereafter be refracted out from the cone-shaped step optical fiber, namely:

$$\left(\arcsin \frac{n_{\mathrm{cl}}}{n_{\mathrm{co}}} - \arcsin \frac{n}{n_{\mathrm{co}}} \right)/3 < \alpha \leq \left(\arcsin \frac{n_{\mathrm{cl}}}{n_{\mathrm{co}}} - \arcsin \frac{n}{n_{\mathrm{co}}} \right). \tag{3.13}$$

On applying Snell´s law at the core-medium interface ② with the use of auxiliary angles shown in Figure 3-5, the numerical aperture can be expressed as a function of the cone-shaped semi-angle α as:

$$\mathrm{NA}(\alpha) = n \cos \left\{ \alpha + \arcsin \left[\frac{n_{\mathrm{co}}}{n} \sin \left(\arcsin \frac{n_{\mathrm{cl}}}{n_{\mathrm{co}}} - 3\alpha \right) \right] \right\}. \tag{3.14}$$

Figure 3-6:   Plot of NA vs. semi-angle α for a commercial single-mode fiber (Thorlabs SM600) with   a   conical   tip   when $\left(arcsin\left(n_{cl}/n_{co} \right) - arcsin\left(n/n_{co} \right) \right)/3 < \alpha \leq arcsin\left(n_{cl}/n_{co} \right) - arcsin\left(n/n_{co} \right)$.

In Figure 3-6, Equation (3.14) is plotted for a commercial single-mode fiber (Thorlabs SM600) surrounded by air. Numerical apertures ranging from 0 to 1 can be achieved by tuning the angle of the cone-shaped optical fiber from $\alpha = 14.3$ to $\alpha = 42.9$ degrees, which shows the opportunity to obtain step optical fibers with actual high numerical apertures.

c.   Multiple internal reflections

The third phenomenon that can arise at the cone-shaped tip of the step index optical fiber is the happening of multiple internal reflections. This section presents a particular situation where only two internal reflections happen. The first total internal reflection happens at cone-shaped surface ① and the second on the cone-shaped surface ②. Thereafter the light-ray is refracted out on the cone-shaped surface ①, as shown Figure 3-7. For total internal reflection to occur on the cone-shaped surface ②, after being totally internally reflected at surface ①, the incident angle θ_i' must fulfill the condition

$$\theta_i' \geq \theta_c' = \arcsin \frac{n}{n_{\text{co}}}. \tag{3.15}$$

Equation (3.15) implies that $\alpha < \frac{(\arcsin(n_{\text{cl}}/n_{\text{co}}) - \arcsin(n/n_{\text{co}}))}{3}$ as was shown for the case of a one total internal reflection.
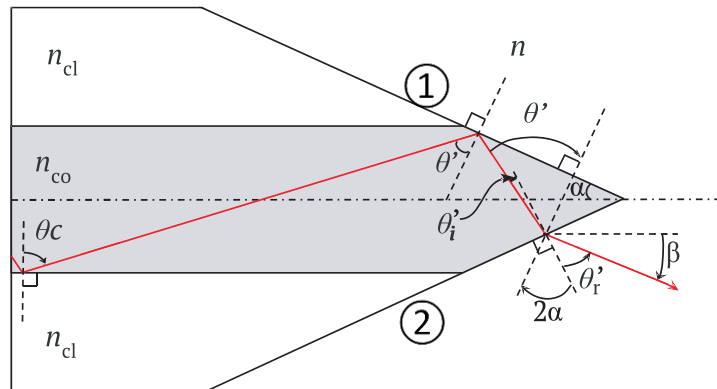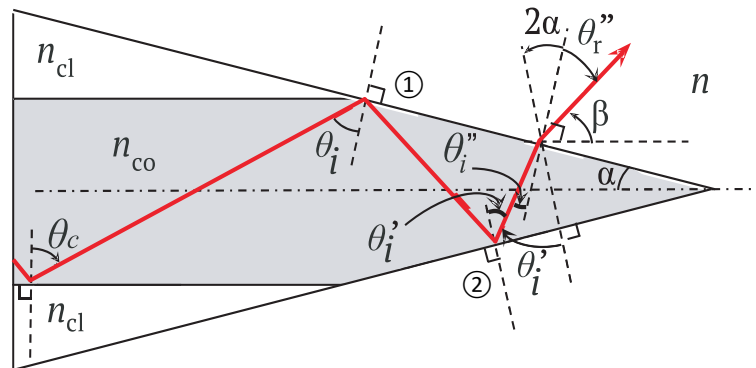

Figure 3-7:   Scheme of a cone-shaped step optical fiber with tapered tip at semi-angle α such that $\frac{(\arcsin(n_{\text{cl}}/n_{\text{co}}) - \arcsin(n/n_{\text{co}}))}{5} < \alpha \leq \frac{(\arcsin(n_{\text{cl}}/n_{\text{co}}) - \arcsin(n/n_{\text{co}}))}{3}$. Under this condition the incident ray suffers one total internal reflection on the cone-shaped surface ①, one total internal reflection on the cone-shaped surface ②, and thereafter is refracted out at the cone-shaped surface ①.

Note that for the light-ray refracted out on the cone-shaped surface ① cone semi-angle α must be chosen such that the incident angle θ_i'' fulfills the condition $\theta_i'' < \theta_c' = \arcsin n/n_{co}$. After some algebra with the geometry and the auxiliary angles illustrated in Figure 3-7, one can arrive to the condition $\theta_i' = \theta_c - 5\alpha$, which leads to an extra limit to the value of semi-angle cone-shaped tip

$$\alpha > (\theta_c - \theta_c')/5. \tag{3.16}$$

Thus, the limits that the semi-angle cone-shaped tip must fulfill for the light-ray guided ray to suffer two internal reflections and thereafter being refracted out from the cone-shaped step optical fiber are given by

$$\frac{\left(\arcsin\frac{n_{cl}}{n_{co}} - \arcsin\frac{n}{n_{co}}\right)}{5} < \alpha \le \frac{\left(\arcsin\frac{n_{cl}}{n_{co}} - \arcsin\frac{n}{n_{co}}\right)}{3}. \tag{3.17}$$

Again, using Snell´s law at the core-medium interface ② with the auxiliary angles shown in Figure 3-7, the numerical aperture in this case is expressed as a function of the semi-angle cone-shaped α as

$$\text{NA}(\alpha) = n \cos\left\{\alpha + \arcsin\left[\frac{n_{co}}{n}\sin\left(\arcsin\frac{n_{cl}}{n_{co}} - 5\alpha\right)\right]\right\}. \tag{3.18}$$

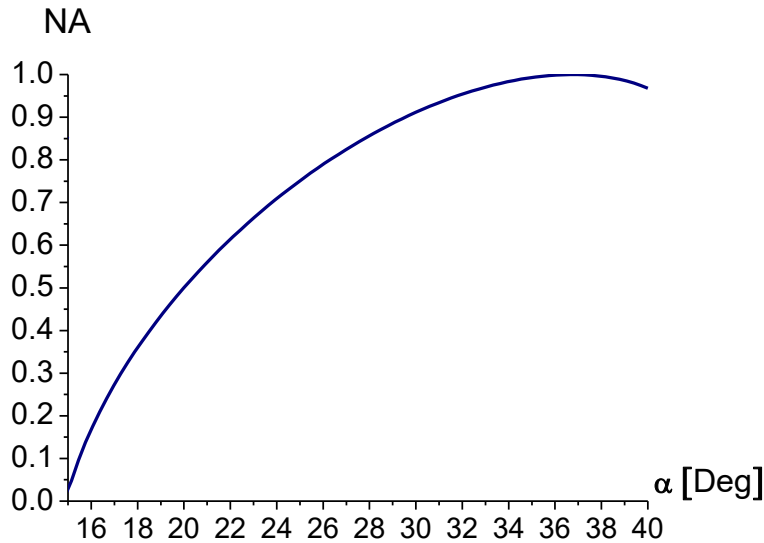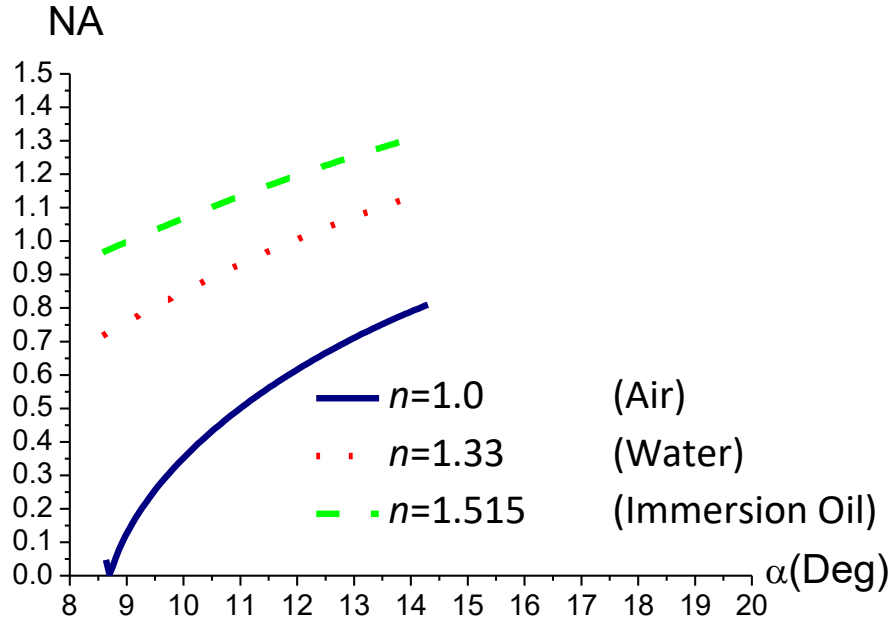**Figure 3-8:**   The plot of NA versus α for the commercial single-mode fiber Thorlabs SM600 with tapered tip at an angle α such $\frac{(\arcsin(n_{cl}/n_{co}) - \arcsin(n/n_{co}))}{5} < \alpha \le \frac{(\arcsin(n_{cl}/n_{co}) - \arcsin(n/n_{co}))}{3}$.

The equations that have been derived in this work also show the opportunity surround the cone-shape optical fiber with mediums with higher refractive indexes than air to increase even further the achieved numerical apertures. To use this possibility, Equation (3.18) has been plotted for a single-mode fiber (Thorlabs SM600) surrounded by different mediums, air (n=1), water (n=1.33), and immersion oil for microscopy (n=1.515). Results are shown in Figure 3-8. In this particular case, it can be noted that by choosing the angle of the cone-shaped optical fiber from $\alpha = 8.58$ to $\alpha = 14.3$ degrees, numerical apertures up to 0.77 for air, up to 1.12 for water, and up to 1.31 for immersion oil can be achieved, providing great versatility in the design of this kind of light sources or light collecting devices. As was expected, the surrounding of the cone-shape optical fiber with mediums with refractive indexes higher than one leads to the very wanted option of numerical apertures also higher than one, a feature very wanted in many applications.

The results of the carried out geometrical analysis that allowed Equation (3.9), Equation (3.14), and Equation (3.18) to be obtained, allow a generalization to be made for the case of more than two total internal reflections. After a said number m of total internal reflections, the numerical aperture, expressed as a function of the semi-angle cone-shaped α, can be written as

$$NA(\alpha) = n \cos\left\{\alpha + \arcsin\left[\frac{n_{co}}{n}\sin\left(\arcsin\frac{n_{cl}}{n_{co}} - (2m+1)\alpha\right)\right]\right\}. \tag{3.19}$$

Where $m = 1,2,3, ..., N$. For a value of m, this equation is valid for the range of α values that satisfy the condition:

$$\left(\arcsin\frac{n_{cl}}{n_{co}} - \arcsin\frac{n}{n_{co}}\right)/(2m+1) < \alpha < \left(\arcsin\frac{n_{cl}}{n_{co}} - \arcsin\frac{n}{n_{co}}\right)/m. \tag{3.20}$$

The parametric Equation (3.19) can be used to design cone-shaped optical fibers with a specific numerical aperture, after the light-ray being totally internal reflected m times. Figure 3-9 shows the NA, for a commercial single-mode fiber (Thorlabs SM600) surrounded by air, vs. semi-angle α, whose ranges of values are determined for the total internal reflections of m =0, m =1, m =2 and m =3, according the Equation (3.20). It can be seen that it is possible to obtain the same numerical aperture for different cone angles. The number m is chosen at the designer's convenience. A number m =0 corresponds with cone tips with

large angles, $m =1$ allows to achieve the largest numerical apertures, while $m =2$ and $m =3$ exhibit dramatically changes in the numerical aperture with small variations of the cone angle, and therefore, a precise control in the cone fabrication is required to ensure the desired value of NA.
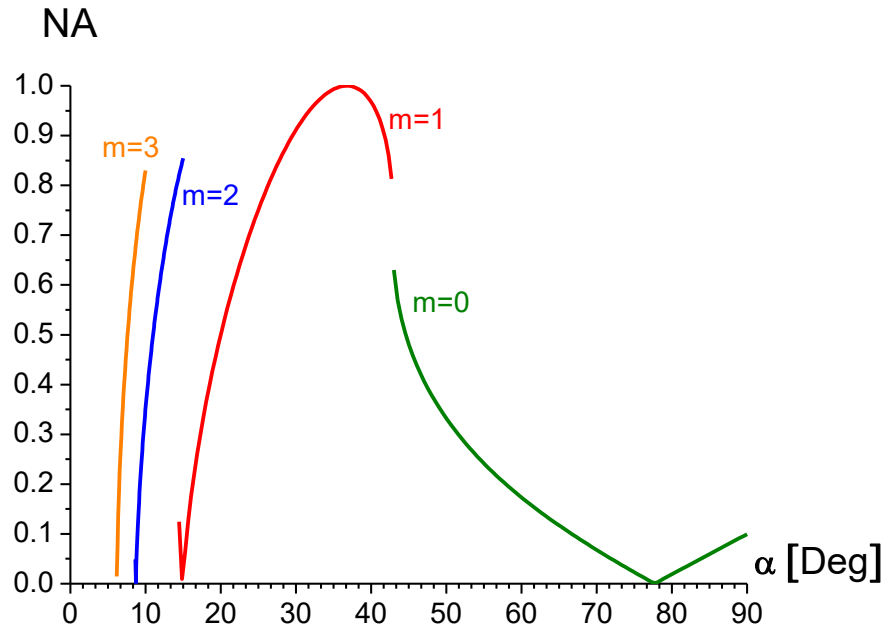
Figure 3-9:   Plot of NA vs. semi-angle α for a commercial single-mode fiber (Thorlabs SM600) surrounded by air.

3.2 Simulation Analysis of the Numerical Aperture in Cone-shaped Optical Fibers

3.2.1 Ray Tracing Study of a Conventional Cone Tip

Once the geometric analysis has been completed, the numerical modeling of the achieved NA with the above design was completed with COMSOL Multiphysics™ [81]–[84]. Standard single-mode step-index optical fibers SM600 surrounded by air with their distal conical tips subtending apex semi-angles of 15, 20, 22, and 29 degrees were discretized using the standard meshing tool with the mesh setting at *Physics-controlled mesh* and the element size set to *Extremely fine.*

A ray tracing numerical modeling was performed for the cone-shaped optical fibers. For the modeling, 50,000 rays from a 4-mW point source were coupled into each of the modeled cone-shaped optical fibers. A screen was placed at 0.5 mm from the apex of the conical tip to record the modeled emitted irradiance and the spot size of the beam. The NA was then determined from the radius of spot and the distance between the screen and the apex of the conical tip. The intensity and the spot size of the beam when the propagated rays stroke the surface were measured in this screen, as shown in Figure 3-10. The numerical aperture was determined from the radius of the spot s, in millimeters, and the distance between the screen and the apex of the cone as follows:

$$NA = n \sin\left(\arctan\left(\frac{s}{0.5}\right)\right) \tag{3.21}$$

The radius of the spot s was determined using the software ImageJ [85] by calculating the intensities of all pixels in a circle of a given radius around the center (maximum intensity) pixel. The radius taken as the spot radius corresponds to the one of the circles that surrounds 95% of the high intensity pixels, according the scale of the image.
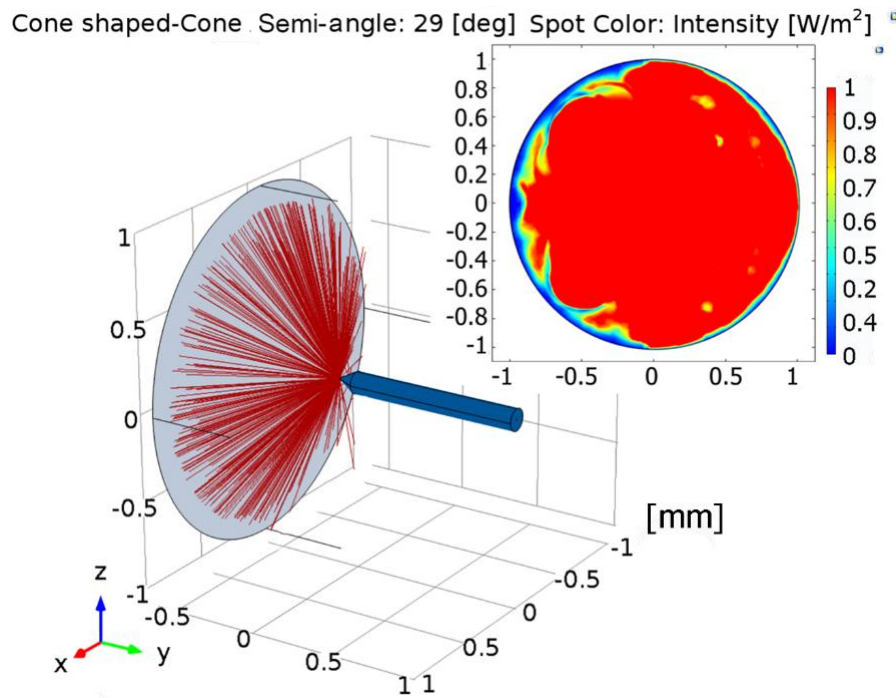
Figure 3-10: Scheme of a fiber optics with tapered tip modeled using COMSOL MultiphysicsTM. A numerical simulation of ray tracing was performed and the NA was determined from the spot size in a screen placed 0.5 mm from the apex of the cone.

Here, $n = 1$ for the simulated air atmosphere. Note, however, that this method of calculation represents an approximation, since not all rays emerge from the apex of the cone shape end, as shown in an enlarged view in the Figure 3-11(a). Although it is not possible to determine at what point on the conical surface of the tip of the fiber the rays with the greatest angle are emerging, the maximum separation distance between the projection of these rays on the axis of the cone and the screen can be determined , according to Figure 3-11 (b), as the maximum distance D; which is given by the following relation:

$$D = \frac{d\,s}{s - y} \tag{3.22}$$

When the screen is far away from the fiber tip, which implies that $s >> y$, the last equation reduces to $D \approx d$. Experimentally, this approximation is valid since the screen can be placed a few millimeters away from the cone tip and the fiber core size is on the order of a few microns.

(a)   (b)
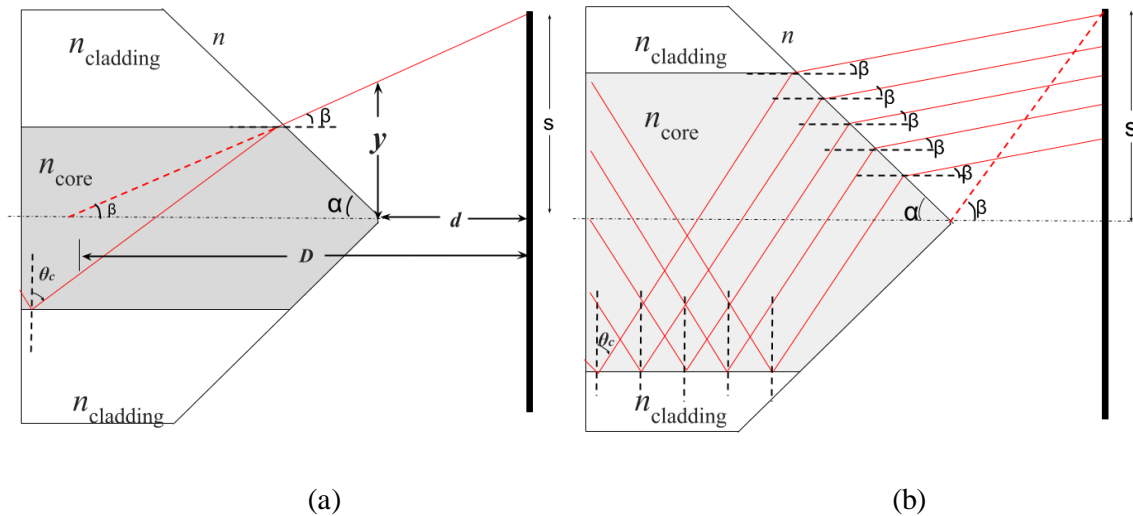
Figure 3-11:   Determination of the NA placing a screen at a distance d from the apex of the cone and measuring the radius of spot size s. (a) This method of calculation represents an approximation since not all the rays with the greatest angle β emerge from the apex of the cone tip. (b) The maximum separation distance between the projection of these rays on the axis of the cone and the screen can be expressed in terms of d, s and y.

In the ray tracing numerical simulation, a circular screen of diameter 10 mm is placed at 0.5 mm from the fiber tip. This distance was not chosen arbitrarily, it corresponds to the maximum allowed separation for which the numerical simulation runs properly with the available computing capacity, since a longer distance implies increasing the number of rays to cover the spot area and increasing the number of the finite elements that constitute the space between the fiber tip and the screen. Additionally, the size of the screen and its separation from the fiber tip have been chosen to ensure that the maximum NA measured is 0.99, according the Equation (2.26). Then, since that y is approximately equal to the fiber core radius (2.1 μm), the maximum distance D is given by:

$$D = \frac{s}{2(s - 0.0021)} \tag{3.23}$$

Note that D approximates to 0.5 mm only if the spot size is at least an order of magnitude greater than the fiber core radius.

The Table 3-1 summarizes the results of the ray tracing simulation analysis and compares them with the theoretical results obtained using Equation (3.20), according to the condition given in Equation (3.21), for commercial single-mode fibers SM600 with tapered end at the selected angles. As it can be seen, the simulation analysis results are in good agreement with the theoretical predicting results using the geometrical analysis, except in the cases where the spot size is very small, as expected considering the Equation (3.23).

The use of the ray-tracing technique to study a regular cone tip was justified by the fact that the core diameter (4.2 μm) was larger than the wavelength used (0.630 μm). Consequently, the diffraction effects associated with the relatively short wavelengths were negligible compared to the light-guiding effect based on the variation in the transverse refractive index profile. However, for completeness and to verify the above assumptions, an electromagnetic wave propagation analysis to study the NA of a regular step-index cone-shaped fiber was also performed, as it is described in the section to follow.

3.2.2   Electromagnetic Wave Propagation in a Conventional Cone Tip

The electromagnetic wave propagation modeling was performed by exciting a TE wave at the flat end of the cone-shaped step-index optical fiber. Along the outside cylindrical surface of the cladding, the electric field was set to zero. This is since the amplitude of the field decays rapidly as a function of the radius of the cladding in the core-cladding interface in the form of an evanescent wave. Thus, the wave is negligible outside the core of the optical fiber. The propagation modes found by the COMSOL solver were those which fulfilled the Maxwell equations with an effective modal index, n_{eff}, between the refractive indexes of the cladding and the core $n_{cl} < n_{eff} < n_{co}$. In the performed analysis, the effective modal index obtained corresponded to that one of the fundamental mode. The reason why only the fundamental mode was considered in the electromagnetic wave propagation was because the SM600 single-mode fiber only supports the propagation of the LP_{01} mode at a wavelength of 633 nm [86], [87]. Note that in COMSOL, setting the search of the mode index slightly above the refractive index of the core of the fiber ensures a faster convergence of the numerical solution. As $n_{co} = 1.46147$, the simulation parameters *desirednumberofmodes* and *searchformodesaround* were set to 1 and 1.461475, respectively. In a similar way as the ray-tracing modeling, a screen located 0.5 mm away from the apex of the cone-shaped step-index optical fiber recorded the irradiance produced by the propagated modes along the fiber. The wave propagation modeling is illustrated in Figure 3-12 for the case of a cone-shaped optical fiber with apex semi-angle of 29°, which produces a NA=0.88.

To measure the NA of the modeled cone-shaped step-index optical fibers, the Gaussian function was used. Under this assumption, the NA is related to the full width at half maximum (FWHM) along a propagation distance d according to [88]:

$$\text{NA} = \sin\left[\arctan\left\{\frac{FWHM}{\sqrt{2\ln2}\,d}\right\}\right],$$

$$(3.24)$$

where the FWHM is related to the radius of the spot of the beam $s(d)$ at a distance (d) from the conical tip [88]:

$$s(d) = \frac{FWHM}{\sqrt{2\ln2}}\ .$$

$$(3.25)$$

The FWHM of each spot was measured with the software ImageJ by fitting a Gaussian profile along a straight line through the center of the image. Table 3-2 summarizes the results of the wave propagation analysis.
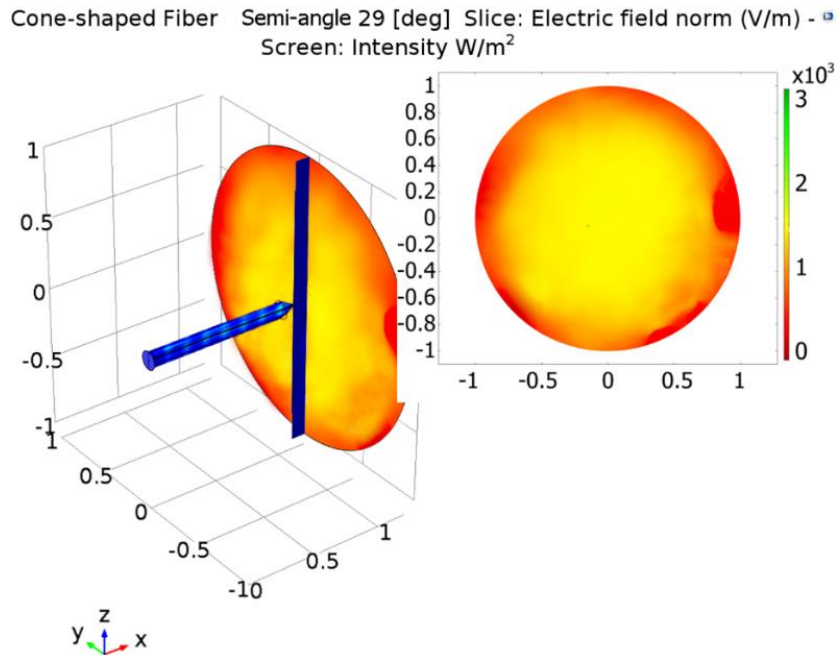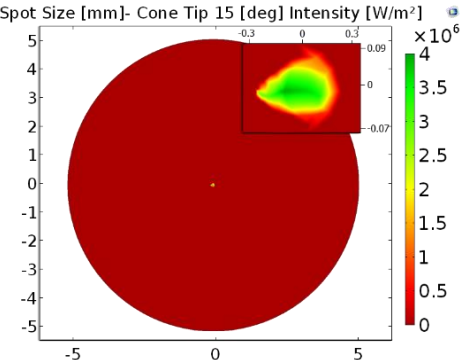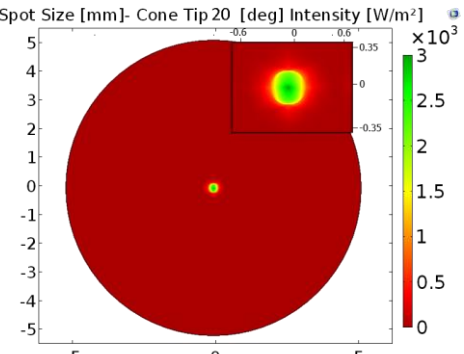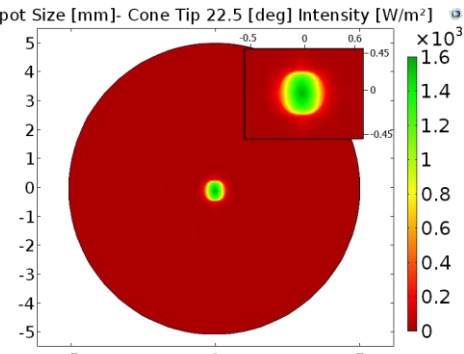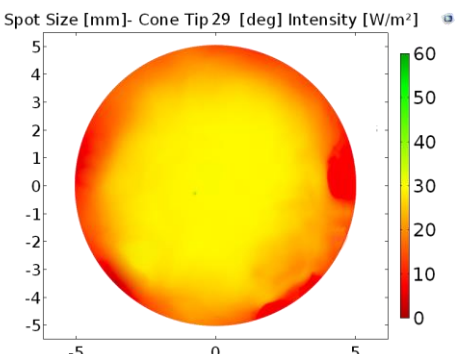
Figure 3-12: Scheme of a fiber optics with cone shape end modeled using the wave optics module of COMSOL Multiphysics™. A numerical simulation of the electromagnetic wave propagation was performed, and the NA was determined from the spot size in a screen placed 0.5 mm from the apex of the cone.

These simulation analysis results confirm that it is possible to control the numerical aperture of a cone tip fiber by a convenient choice of the cone angle. However, the fabrication of cone tips with a specific angle is not an easy task. The method of production of etched cone tip fibers is described in the next chapter.

Table 3-1:   Ray tracing numerical simulations in COMSOL Multiphysics™ for cone-shaped optical fiber with semi- angles of 15, 20, 22.5 and 29 degrees. The subscripts S and T refer to simulation and theoretical values of the numerical aperture.

Semi-angle	Ray Tracing	Spot Size (±0.01) mm	NA (±0.01)
15°			NA_S=0.13 NA_T=0.02
20°			NA_S=0.51 NA_T=0.49
22.5°			NA_S=0.67 NA_T=0.64
29°			NA_S=0.91 NA_T=0.89

Table 3-2:   Numerical simulations in the wave optics module of COMSOL Multiphysics™ for a commercial single-mode fibers SM600 with tapered end at 15, 20, 22.5, and 29 degrees. The subscripts S and T refer to simulation and theoretical values.

Semi- angle (±0.1) °	Spot Size (±0.01) mm	NA (±0.01)
15°		$NA_S = 0.15$ $NA_T = 0.02$
20°		$NA_S = 0.49$ $NA_T = 0.49$
22.5°		$NA_S = 0.71$ $NA_T = 0.64$
29°		$NA_S = 0.88$ $NA_T = 0.89$

The obtained results until now are summarized in a plot in Figure 3-13. The predicted theoretical NA presented in Section 3.1.2 using Equation (3.14) with m=1, for the range of semi-angles from 15° to 29° is plotted in solid line. In this analytical design the refractive indexes of a commercial single mode optical fiber Thorlabs SM600, (n_{co}=1.46147 and n_{cl}=1.45804) surrounded by air (n=1) were used. The theoretical model of NA for the optical fiber is contrasted in Figure 5-4 with the ray-tracing simulation results, in circles, and the wave optics propagation results in solid squares.
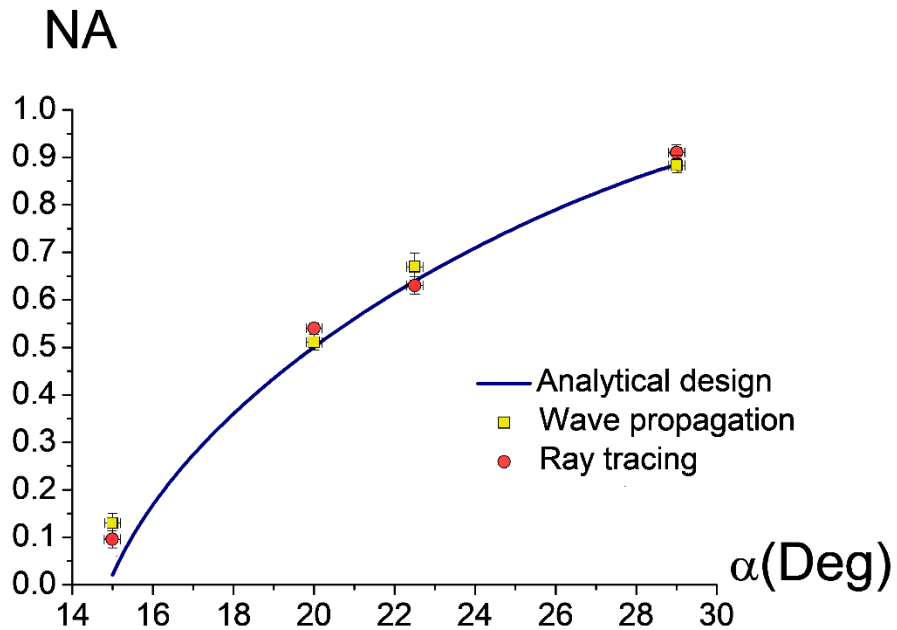
Figure 3-13. Plot of the NA vs. the semi-angle α for a commercial single-mode fiber (Thorlabs SM600 n_{co}=1.46147 and n_{cl}=1.45804) surrounded by air. The solid line is the result of plotting (1). Both modeling results, ray-tracing (circles) and wave optics propagation (solid squares) are also presented.

4.   Fabrication of cone shape fibers tips with Tailored cone angle

Cone-shaped optical fibers are used in very diverse applications from nanoscale imaging [89], near-field optical microscopy [24], [26], [90], [91], photon scanning tunneling microscopy [37], [92], sensing applications [25], [93], and nanofabrication, to molecular biology and medical diagnostics [25]. Most of the cone-shaped fibers used today are produced either by heating and pulling [18], [19], [33], or by chemical etching in aqueous solution of fluorhydric acid (HF). The etching methods include dynamic etching [23], [25], [93], [94], selective etching [95], and static etching [18], [24], [77], [96].
In the heating and pulling method, an optical fiber is heated either by a tungsten filament conducting an electric current, a flame produced by a fuel combustion, or using CO_2 laser pulses, while being pulled by an axial tension applied at a controlled speed. This technique requires complex and expensive equipment and complicated manipulations to precisely control the angle of the tip.

On the other hand, the chemical etching methods are the most popular and reproducible techniques to fabricate fiber tips. The dynamic etching is based on a moving or rotating optical fiber that is immersed vertically in a two-phase solution of HF and an organic solvent. In this method, as in the heating and pulling method, a sophisticated equipment is required to control the movements of the fiber [19], [94].

Lastly, selective etching and static etching are the simplest and lowest cost methods to fabricate fiber tips because they only imply immersing the fiber ends into an adequate

etching solution to obtain the conical shape tip. In the selective chemical etching method, the difference in etching rates of the doped silica that makes up the core of the fiber and the pure silica that constitutes the cladding is controlled to modify the angle of the cone tip fiber. A suitable buffered acid solution composed of HF, water, and 40% ammonium fluoride (NH_4F) is used to etch the cladding faster than the core, resulting in a cone whose base diameter corresponds to the core of the fiber [95].

The static chemical etching, also known as Turner Method [97], is the most widely used method for the fabrication of cone-shaped optical fibers and is based on the chemical etching of the distal end of the fiber in an aqueous HF solution with an organic solvent cover layer. The tip fabrication takes place at the interface of the etching liquid and the cover layer thanks to the formation of a meniscus, which is determined by the acid–cover layer–fiber interface, as explained in detail in [18]. The cone angle is mainly determined by the meniscus height, which decreases with time as the fiber diameter reduces due to etching. This method is very reproducible, does not require complicated equipment, is self-terminating, and allows for cone semi-angles apex of up to 22° with high transmission efficiencies ($\sim 10^{-4}$) to be obtained [24], [98]. The transmission efficiency is defined as the ratio of output energy to the input coupled energy [99].

Since the static chemical etching is the simplest method to produce cone-shaped optical fibers, great effort has been made to modify the geometry of the tips according to the requirements of the various applications in which they can be used. This include varying the etching rates and using different protective solvents. In spite of these efforts, it has not been reported in the literature cone-shaped fibers with shorter tapers, smooth surfaces, and large conical semi-angles (>22°) with merely static etching. However, tips with shorter tapers and larger conical aperture angles fabricated thanks to the diffusion of etchants in the cover- layer have been reported by Yihong et al [77].

What happens is that in the static chemical etching the diffusion of the etchant promotes that the etching reaction continues, but now into the cover-layer, after the cone tip has been formed. These processes can modify the shape and size of the tip if given the adequate time. This additional etching, however, was reported to only affect a small part at the end of the cone due to the short time allowed for the diffusion to take place (less than 75 minutes). Additionally, the reported tips do not exhibit a very smooth surface [77].

In this chapter, the geometrical characteristics of chemically etched cone tips are studied considering the effect of etchant diffusion for prolonged times. A simulation in COMSOL Multiphysics™ using the transport of chemical species was performed in order to verify that tips with shorter tapers and larger conical aperture angles can be fabricated thanks to the diffusion of etchants in the cover- layer as report Yihong et al [77]. Finally, an experimental setup was developed allowing for cone-shaped optical fibers with short tapers, very smooth surfaces, and larger conical angles to be obtained from single-mode fibers. The main parameters affecting the final shape of the cone tip are also discussed.

4.1   Materials and methods

Several single-mode optical fiber pieces (Thorlabs SM600) with 10 mm of protective jacket removed from their distal end were immersed in an aqueous HF solution (21%) covered by a thin layer of sunflower oil. This etching solution was contained in a Teflon vessel devised to assist the vertical placement of the fibers to be etched, as illustrated in

Figure 4-1.The etching temperature was maintained at (25±1) °C. Cone-shaped optical fibers were formed at the tips of the optical fibers after 5 hours of immersion, in a process schematized in Figure 4-2.
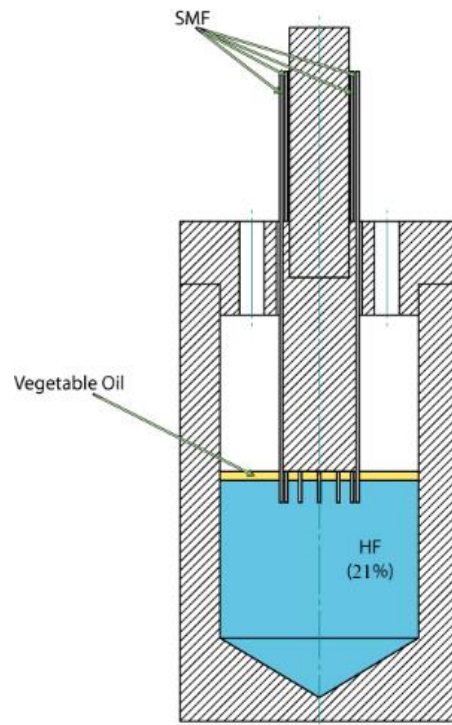
Figure 4-1:   Schematic diagram of the experimental setup used to assist the vertical placement of the optical fiber to be etching.

After the cone tips formation, the fibers were removed from the vessel and immersed in a supersaturated solution of calcium carbonate ($CaCO_3$) to arrest the chemical etching. This procedure was performed one fiber at a time with intervals of one hour up to complete 26 hours since the initial immersion.

(a)   (b)   (c)
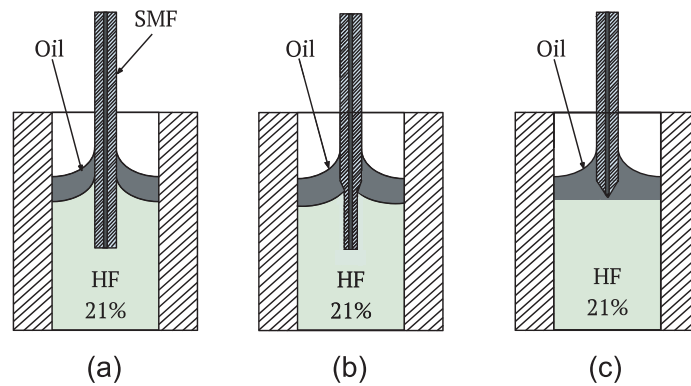
Figure 4-2:   Schematic diagram of the fiber during the etching process: (a) at the early stages of etching, (b) in the meantime of the process, and (c) after the cone tip is formed (~ 5 hours). Notice the height reduction in the meniscus at the HF-oil interface as the etching progresses.

To illustrate the process of formation of the tip, a simulation in COMSOL Multiphysics™ was performed using the transport of chemical species module coupled to the deformed geometry module [81], [82], [100]. The Figure 4-3 (a) shows the simplified 2D model geometry.

(a)   (b)
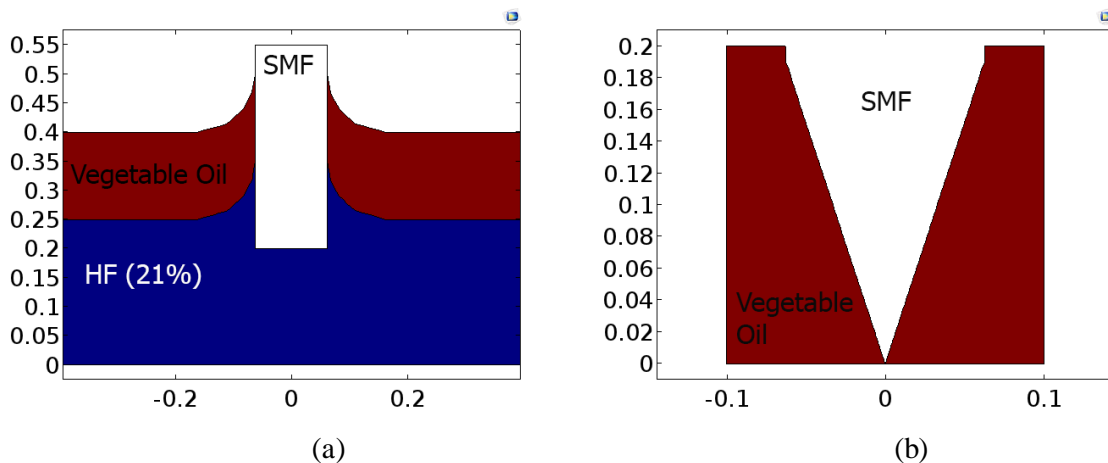
Figure 4-3: Geometry of the simulation domains in COMSOL used to study (a) the process of formation of the tip and (b) analyze the effect of etchant diffusion on tip profile

As aforementioned, the etching reaction takes place at the meniscus between the hydrofluoric acid and the vegetable oil cover layer in such a manner that the conical surface occurs as a result of the decreasing meniscus height when the fiber diameter is reduced by the HF. The rate of this reaction k [(m/s)] depends on the local concentration of HF, $c \left[\frac{mol}{m^3} \right]$, at the etching surface (moving boundary) according the First Fick's law of diffusion:

$$D\nabla c \cdot n = -kc \qquad (4.1)$$

where $D \left[\frac{m^2}{s} \right]$ denotes the diffusion coefficient and n is the normal vector.

The discretization process of the simulation domain in COMSOL was developed using the Standard meshing tool with the mesh set at *Physics-controlled mesh* and element size set to *Normal*. The parameters for the simulation were the diffusion coefficient of HF 21% in water $D = 4.3 \times 10^{-9} \left[\frac{m^2}{s} \right]$ [101], the density of HF 21%, $\rho = 1070 \left[\frac{kg}{m^3} \right]$, and the molar mass of HF $M = 0.02 \left[\frac{kg}{mol} \right]$. The results of this simulation are shown in Figure 4-4.

The shape evolution of the fiber being etched to form the cone-shaped was simulated using the *Deformed geometry* module that displaces the etched boundary on the sides of the fibers compressing consequently the mesh that defines the optical fiber. The study of the formation of the cone tip stops at the point where the mesh cannot be compressed any further. This stage was reached when the simulated time was close to 180 minutes of chemical etching acting on the fiber end, as shown in Figure 4-4.

The next step was to analyze how the etchant continues into the oil cover layer and its effect on the cone-shape geometry. To achieve this, a second COMSOL simulation was performed using the same coupled modules. In this case, however, a time-dependent study was performed in the *Transport of chemical species* module to determine how the concentration changes with time. This is, solving Fick's second law:

$$\frac{\partial c}{\partial t} + \nabla \cdot (D\nabla c) = R, \qquad (4.2)$$

where $R \left[\frac{mol}{m^3 s} \right]$ indicates the reaction rate. The shape evolution of the etched tip was simulated using the *Deformed geometry* module that displaces the etched boundary according to an interfacial condition for the normal mesh velocity v:

$$v = \frac{DM}{\rho} \qquad\qquad (4.3)$$

An enlargement of the apex angle and reduction in the cone height is expected due to the different etching rates caused by the concentration gradient in the vertical direction after the oil–HF interface. It is important to clarify that the changes in the profile and size of tip after the formation of the cone is determined not only by diffusion of the two phase-contact liquids but is also related to other factors such as solubility and convection [76] [102]. HF convection occurs across the oil-HF interface, as HF is consumed the reaction products move away due to gravity since the products are denser than the HF itself.
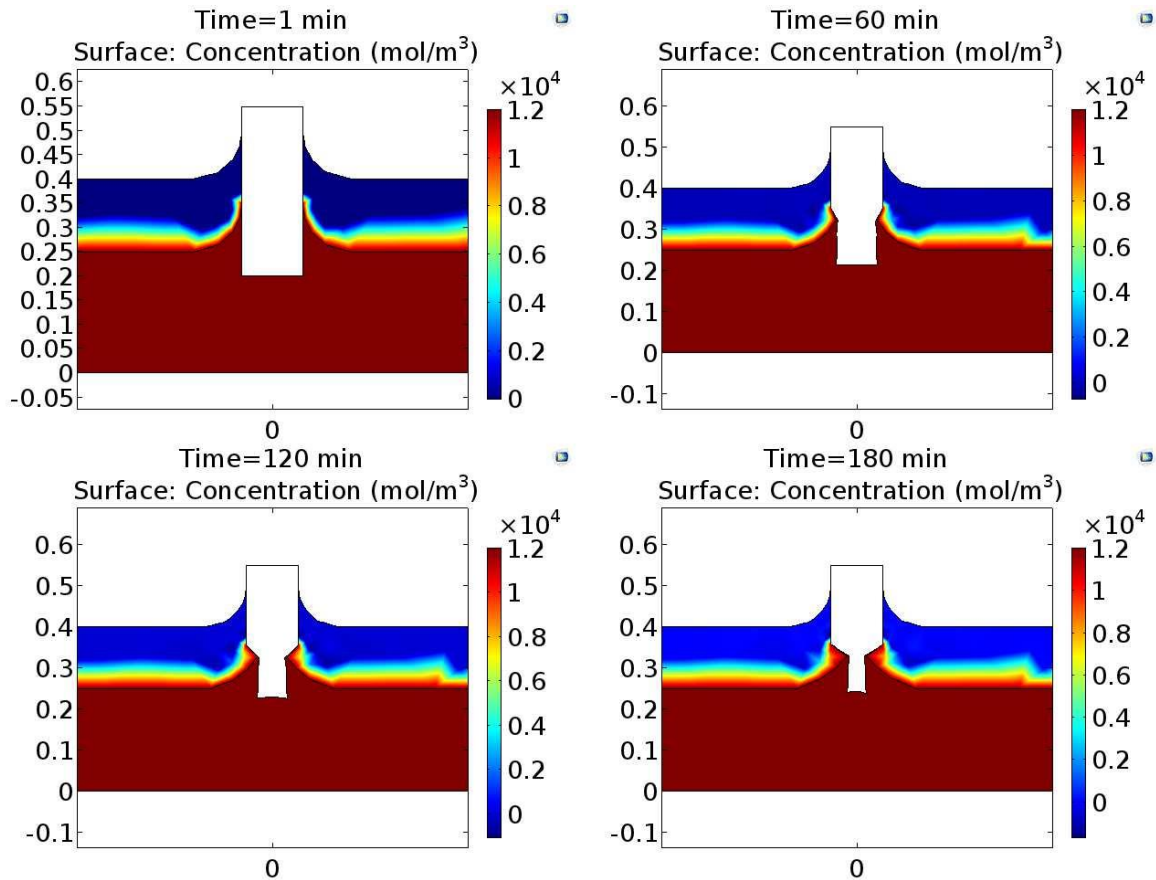
Figure 4-4:   Results of the numerical simulation in COMSOL Multiphysics™ of the process of formation of the cone tip by the method of static etching. The process stops after about three hours since the mesh cannot be compressed any further.

The domain geometry for the second set of simulations, where the difussion into the oil cover layer occurs, is shown in Figure 4-3 (b). Although the diffusion of HF 21% in sunflower

is studied, no effects of etchant diffusion on tip of the fiber are considered between t=0 and t=5 h. Simulation of diffusion during this period is necessary in order to determine the initial concentration of etchant in the coverlayer immediately after cone-shaped optical fibers are formed. The discretization process was developed using the *Standard meshing tool* and element size was set to *normal*. The parameters used in the simulation were: The diffusion coefficient of water in sunflower oil $D = 0.25 \times 10^{-9} \left[\frac{m^2}{s}\right]$ [25], density of the sunflower oil $\rho = 980 \left[\frac{kg}{m^3}\right]$, the volume force vector was specified as $F = \rho \cdot g$, and the pressure was specified as a boundary condition $P = \rho \cdot g \cdot y$, where y is the horizontal location in the vegetable oil. A concentration source of HF (12 M) was set at the lower boundary. The results of this simulation at various times are summarized in Figure 4-5 and in Figure 4-6. These simulation results corroborate that the existence of a HF concentration gradient in the coverlayer is proportional to the formation of a larger cone semi-angle. In the next section, this characteristic of chemically etched cone tips is experimentally verified considering the effect of etchant diffusion for prolonged times.
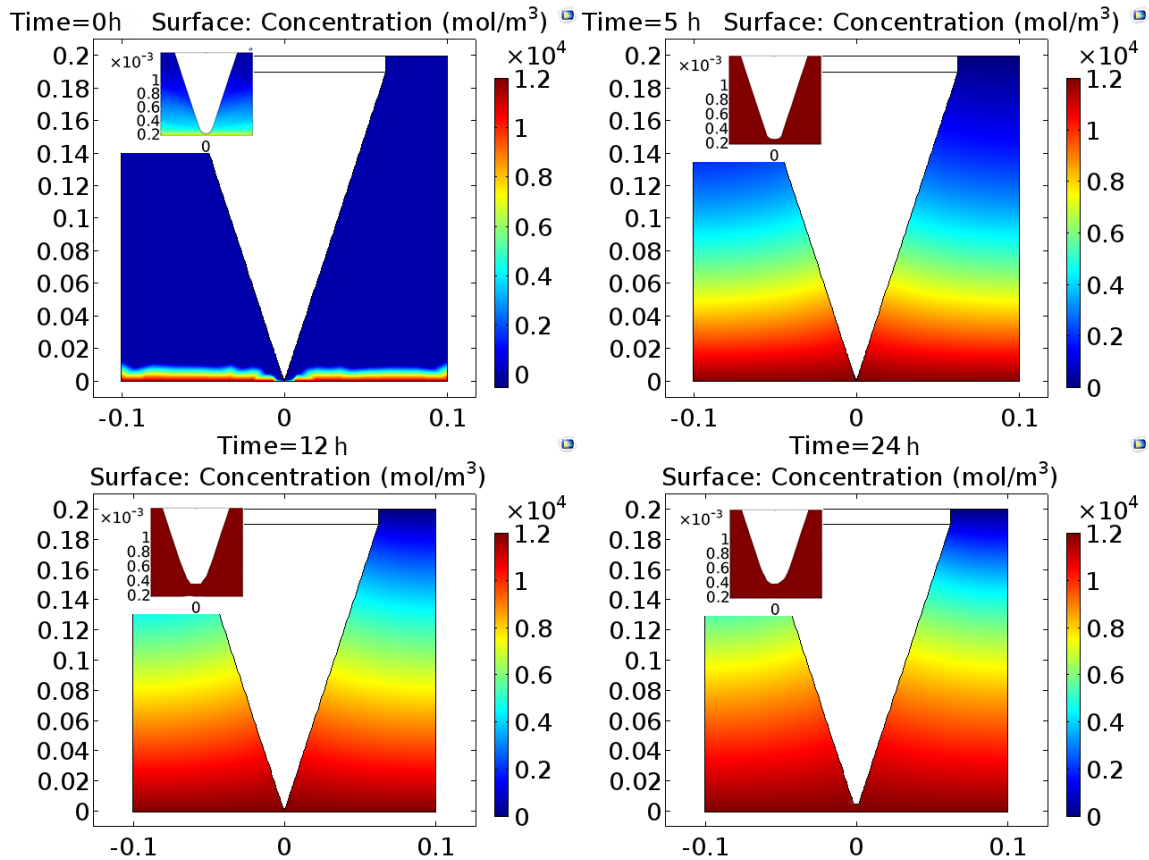
Figure 4-5:   Simulation results for the model used to analyze the effect of etchant diffusion on tip profile.
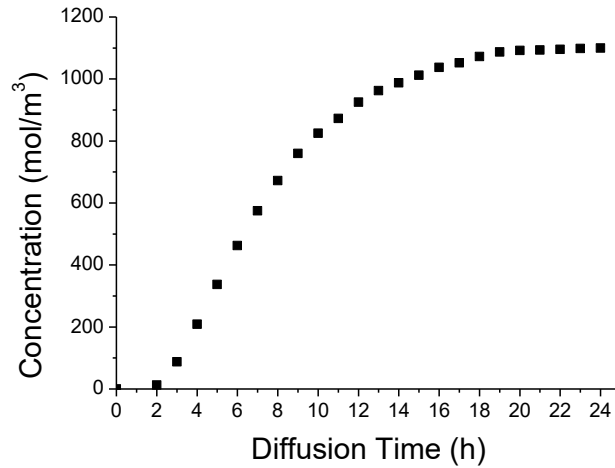
Figure 4-6:   Simulation results of the etchant concentration vs diffusion time.

4.2 Results and discussion

Figure 4-7 (a) shows a detailed view of some of the cone-shaped fibers with larger conical semi-angles. The cone semi-angles were measured using the angle tool of the open source software ImageJ [103], from the measurement of the half angle defined by the two lines that mark the apex of the cone in the core section (at the last 5 µm of the tip), as shown Figure 4-7 (b). The SEM image in Figure 4-7 (c) shows in detail the surface of an etched cone-shaped fiber with large conical angle. The very smooth surface observed is the result of the small amount of etchant in the cover layer and the slow etching rate of the HF at 21% on the conical surface of the fiber.

A plot of the cone semi-angle versus time is shown in Figure 4-8 and Figure 4-9 shows the obtained cone tips manufactured through static etching at different times and in .The geometrical characteristics of the enlargement of the apex angle and reduction in the cone height are clearly observed over etching time. These geometrical changes occurring after the cone-shape formation can be explained through the HF diffusion into the oil cover layer, in agreement with the simulation shown in Figure 4-5. This concentration gradient of HF acts with different reaction rates on the cone-shaped optical fibers, thus the etching rates are higher in the oil-HF interface neighboring. The amount of time required to observe a significant change in the geometry of the tip can be attributable to the low solubility and low diffusion coefficient of HF at 21% in the oil.
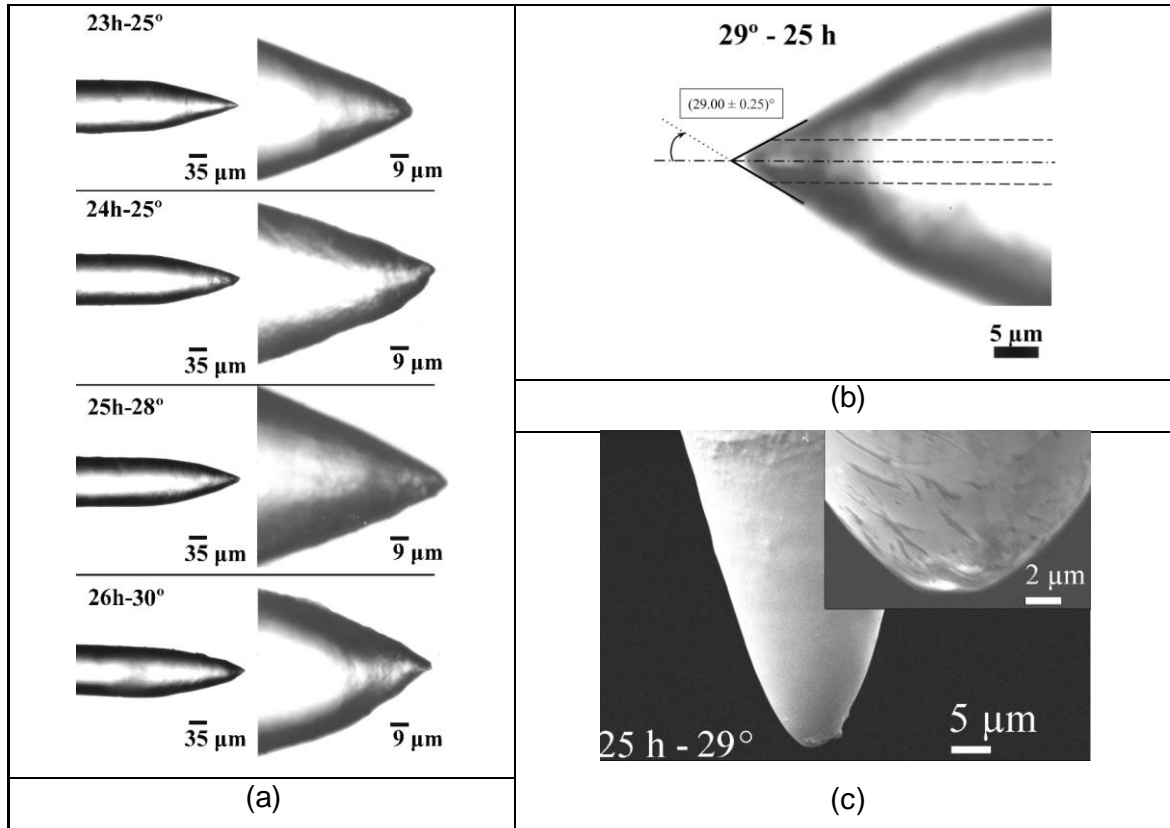
Figure 4-7: Detail of the fabricated tips with the larger conical semi-angles. The images (a) and (b) shows cone-shaped fibers with larger conical semi-angles obtained under an optical microscope. Dashed lines represent the fiber's core approximate location. The image (c) is a SEM image of a cone-shaped optical fiber.
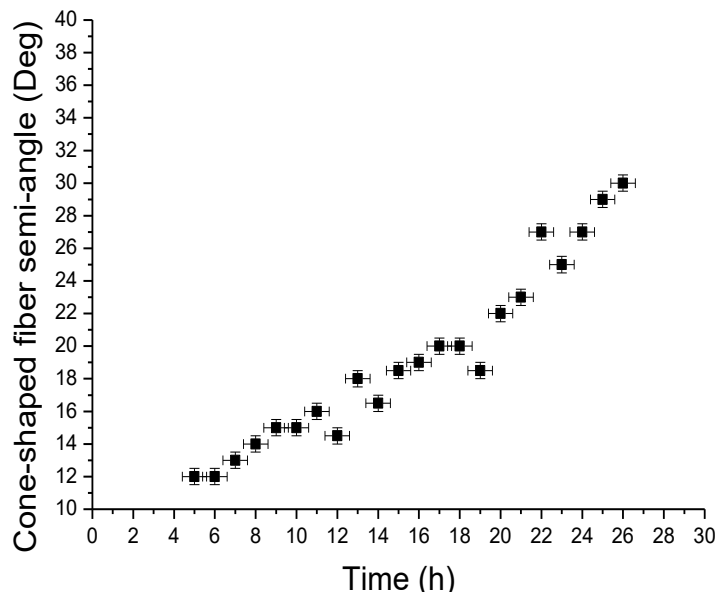
Figure 4-8: Cone semi-angle versus time. Cone-shaped optical fibers were formed at the tips of the optical fibers after 5 hours of immersion in HF solution (21%) covered by a thin layer of sunflower oil. The etching temperature was maintained at (25±1) °C. The existence of a HF concentration gradient in the coverlayer is proportional to the formation of a larger cone semi-angle.

6 h - 12 ° $\overline{35}$ µm

7 h - 13 ° $\overline{35}$ µm

8 h - 14 ° $\overline{35}$ µm

9 h - 15 ° $\overline{35}$ µm

10 h - 15 ° $\overline{35}$ µm

11 h - 16 ° $\overline{35}$ µm

12 h - 14.5 ° $\overline{35}$ µm

13 h - 18 ° $\overline{35}$ µm

14 h - 16.5 ° $\overline{35}$ µm

15 h - 16.5 ° $\overline{35}$ µm

16 h - 19 ° $\overline{35}$ µm

17 h - 20 ° $\overline{35}$ µm

18 h - 20 ° $\overline{35}$ µm

19 h - 18.5 ° $\overline{35}$ µm

20 h - 22 ° $\overline{35}$ µm

21 h - 23 ° $\overline{35}$ µm

22 h - 22 ° $\overline{35}$ µm

23 h - 25 ° $\overline{35}$ µm

24 h - 27 ° $\overline{35}$ µm

25 h - 29 ° $\overline{35}$ µm

26 h - 30 ° $\overline{35}$ µm
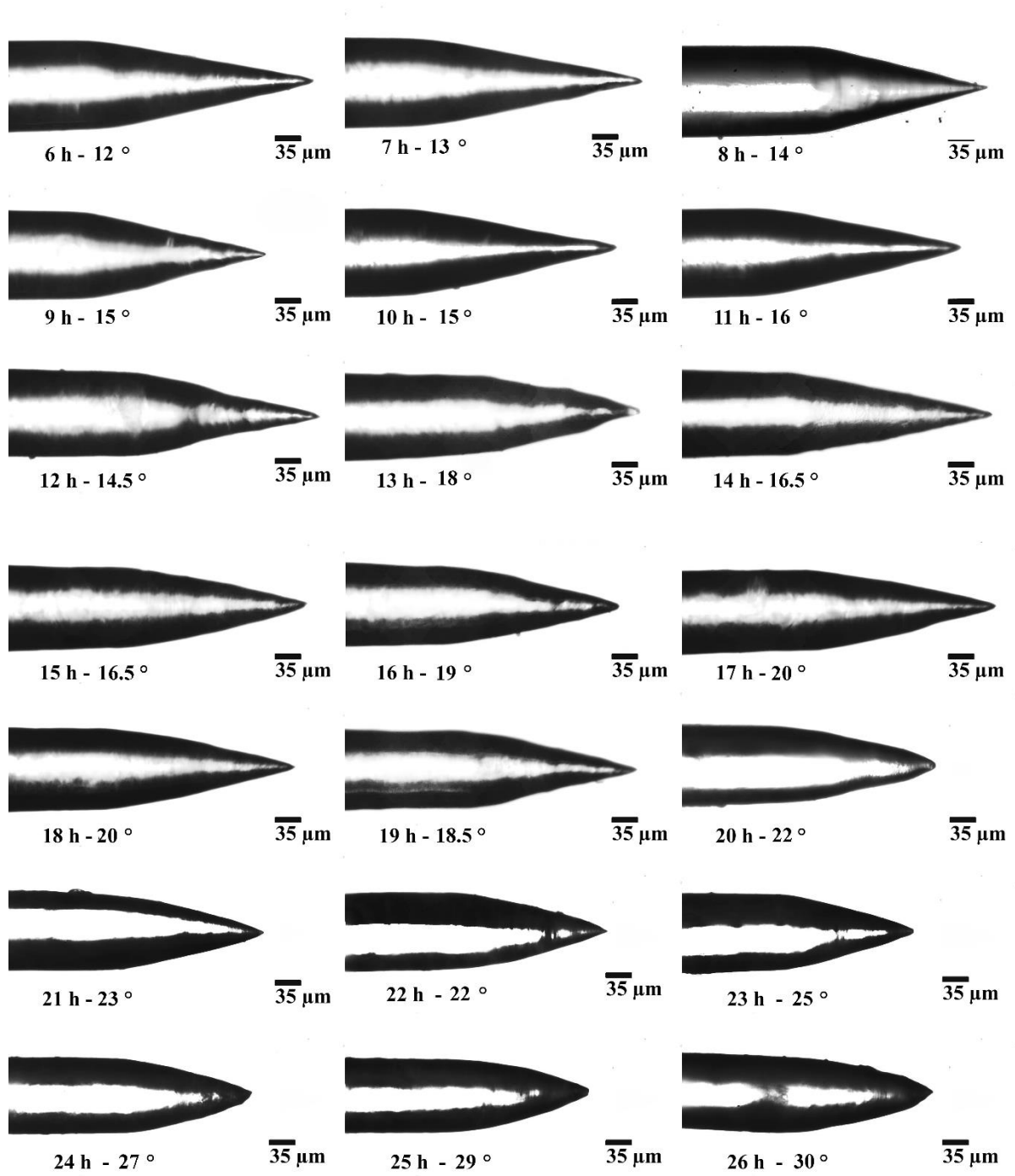
Figure 4-9:   Results of the fabricated tips at different times over the 26 hours of static etching.

5. Experimental Results of the Numerical Aperture of the Conventional Cone Tips

As it was presented in Chapter 3, the numerical aperture of an optical fiber is the parameter that describes not only the maximum angle which the light exits the fiber, but also the maximum angle at which the light incident on the fiber is totally internally reflected and it can propagate along the fiber. In general, to have an optical fiber with the largest possible NA is desired to guarantee the largest accepting or emitting cones of light; which eases the light coupling and minimizes the losses. As for the case of step-index optical fibers, as shown in preceding chapters, cone shaping seems to be the most accessible option to increase the NA, in comparison with other methods such as photonic-crystal [69]–[71], with the advantage that NA could be tailored by choosing a particular angle of the cone. In order to experimentally verify the obtained results of the analytical and simulation studies, a methodology to measure the NA for the cone-shaped optical fibers is described in this chapter.

As the main objective at this point is to validate the possibility of producing cone-shaped step-index optical fibers with tuned NA in the range from 0 to 1 in air, $m = 1$ was chosen for the design Equation (3.19). This condition, $m = 1$ which implies a single total internal reflection at the conical tip, occurs for conical tip semi-angles from 14 to 43 degrees according Equation (3.20). However as shown in Chapter 4, owing to the limitations of the fabrication by the etching chemical method, only conical tips with semi-angles from 15 to 29 degrees were fabricated, and therefore, NAs from 0.02 to 0.88 were obtained. A complete report of the experimental results of the NA measurement for these cone-shaped optical fibers and the discussion of those are presented throughout the chapter.

5.1   Measurement of the Numerical Aperture of the Cone-shaped Optical Fibers.

In the visible light range, the numerical aperture of an optical fiber is measured from the radius of illumination spot on a screen and the distance between the screen and the end of the cone [104], [105]. Figure 5-1 shows the spots for various cone-shaped optical fibers with different cone angles. It can be seen that the spot size is difficult to define from the distribution of intensity on the screen perceived by the human eye. If the spot is recorded onto a camera, the maximum coupling of light from the source into the fiber allows a saturated spot to be observed, and this spot is what is typically used to determine the numerical aperture of the fiber [104], [105].
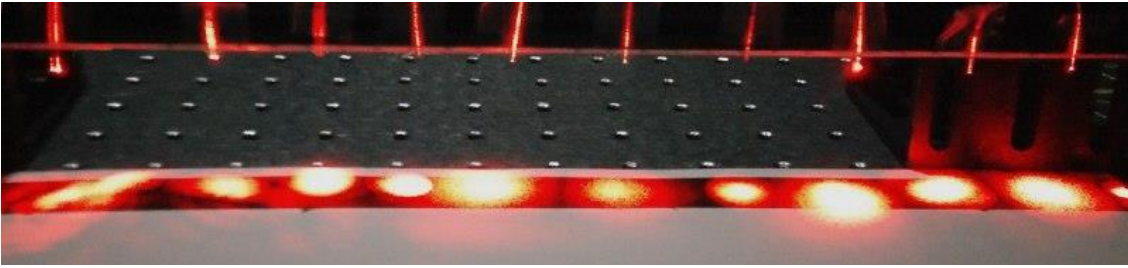
Figure 5-1:   Spots of cone-shaped optical fibers as illumination sources with different cone semi-angle.

A more adequate determination of the numerical aperture may be carried out by fitting a Gaussian function to the intensity profile at the output of the fiber. From this fitting it is possible to obtain the full width at half maximum (FWHM) in the transversal direction of the spot. The FWHM is related to the radius of the beam $w(z)$ at a distance (z) from the fiber according to [88]:

$$w(z) = \frac{\text{FWHM}}{\sqrt{2\ln2}} . \tag{5.1}$$

The radius of the beam $w(z)$ at a distance (z) from the fiber is given by [106]:

$$w(z) = w_o\sqrt{1 + \left(\frac{z}{z_r}\right)^2}, \tag{5.2}$$

where w_o is the the waist radius, and z_r is the Rayleigh range. The latter is related to the wavelength λ of the laser light by [107]:

$$z_r = \frac{\pi w_0^2}{\lambda}.$$

For $z \gg z_r$, $w(z)$ increases linearly with z, which implies that far from z_r the waist of the beam is cone-shaped, as shown in Figure 5-2. The angle formed between the central axis of the beam and the lines along that cone is called the divergence of the beam, and corresponds to the angle of the numerical aperture NA. Then the NA is given by:

$$\text{NA} = \sin\left[\arctan\left\{\frac{\Delta\text{FWHM}}{\sqrt{2\ln 2}\Delta z}\right\}\right] \tag{5.3}$$
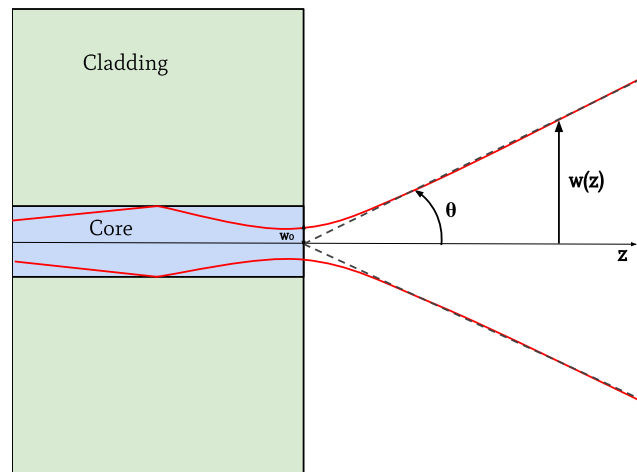
Figure 5-2:   Output beam from the end of the fiber approximated to a Gaussian beam with width $w(z)$ as a function of the distance z. The angle θ is the divergence of the beam and corresponds to the angle of the NA.

Using the aforementioned framework, the fabricated cone shaped optical fibers were spliced to single mode patchcord cables with FC/PC connectors on one end (Thorlabs P1-630A-FC-1); a laser diode emitting at a wavelength of 632.8 nm was coupled to these patchcords. The cone-shaped end of each optical fiber was placed into a side-loading fiber chuck (Thorlabs HFC007) and mounted vertically on a three-axis flexure stage (Newport 460A-XYZ), as shown in Figure 5-3. The apex of the cone tip was placed first at a distance of 4 mm from a CMOS camera sensor (Lumenera LU120) where a first spot image was recorded. The fiber was then placed 2 mm away from the camera sensor and a second

spot was registered. The FWHM was determined through a Gaussian fit of the intensity profiles for each recorded spot. With the data of the Gaussian fit and $\Delta z = 2$ mm, the NA was finally calculated using Equation (5.3).
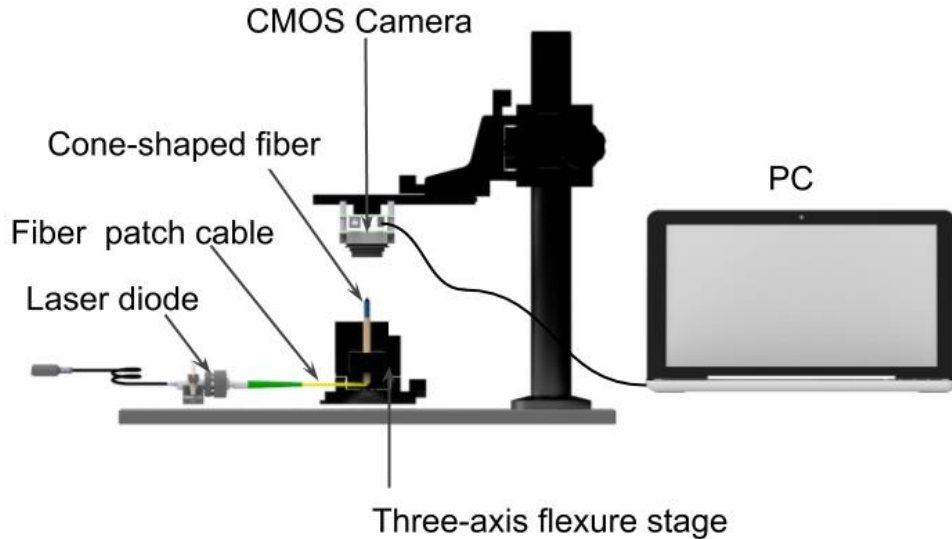
Figure 5-3:   Experimental arrangement used for the measurement of the numerical aperture of the cone tips. This apparently simple experimental setup constitutes the Digital Holographic Microscope Lensless (DHML).

5.2   Results.

First column of Table 5-1shows the images of cone-shaped optical fibers and their recorded intensity spots. The intensity profile was measured along the white line on each spot and a Gaussian fit was used to determinate the NAs using Equation (5.3). It can be observed that the NA obtained on each cone-shaped optical fiber increases with the etching time and the resulting angle. The recorded intensity spots show a ring-like structure produced by the self-interference the spherical waves emitted by the tip on the different optical layers of the CMOS camera. Along the white line over the intensity spot, the profile was measured and plotted with the black line in second column of Table 5-1. To validate the premise of Gaussian shape of the intensity spot, the red line in panel (b) shows the numerical fitting with the parameter presented in the inset.

Table 5-1:   Numerical aperture measurements for some fiber tips. The transverse intensity profile of the spot of the output from the fiber approximated by a Gaussian function also has been included.

Cone Tip and Spot	Transverse Intensity Profile
15° - 10 h	
20° - 17 h	
22.5° - 20 h	
29° - 25 h	

For **15° - 10 h**:

Gaussian	
NA	**0.14**
Adj. R-Squar	0.99141
sigma	0.93854
FWHM	2.2101
Height	112.18443

For **20° - 17 h**:

Gaussian	
NA	**0.47**
Adj. R-Square	0.9914
sigma	0.8467
FWHM	1.9939
Height	166.17

For **22.5° - 20 h**:

Gaussian	
NA	**0.56**
Adj. R-Square	0.98706
sigma	0.86555
FWHM	2.03821
Height	153.4551

For **29° - 25 h**:

Gaussian	
NA	**0.88**
Adj. R-Squar	0.98861
sigma	0.88739
FWHM	2.08964
Height	55.64022

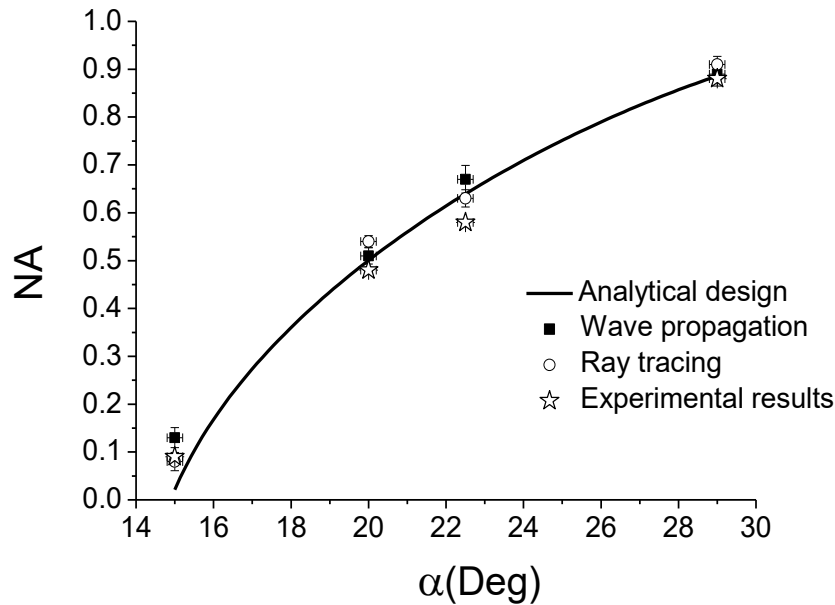**Figure 5-4:**   Plot of the NA vs. the semi-angle α for a commercial single-mode fiber (Thorlabs SM600 n_{co}=1.46147 and n_{cl}=1.45804) surrounded by air. The solid line is the result of plotting (1). Both modeling results, ray-tracing (circles) and wave optics propagation (solid squares), along with the experimental results (stars) are also presented.

The obtained results until now in this thesis are summarized in a plot in Figure 5-4. The predicted theoretical NA presented in Section 3.1.2 using Equation (3.14) with m=1, for the range of semi-angles from 15° to 29° is plotted in solid line. In this analytical design the refractive indexes of a commercial single mode optical fiber Thorlabs SM600, (n_{co}=1.46147 and n_{cl}=1.45804) surrounded by air (n=1) were used. The theoretical model of NA for the optical fiber is contrasted in Figure 5-4 with the modeling results presented along this thesis have for cone-shaped optical fibers with semi-angles 15°, 20°, 22.5°, and 29°. The ray-tracing simulation, presented in Section 3.2.1, is shown in circles; the wave optics propagation, presented in Section 3.2.2 is shown in solid squares; and finally, the experimental results from the cone-shaped fabricated by the chemical etching method are shown in stars.

The concurrence between the analytical equation, the modeling results, and the experimentally measured numerical apertures, shows that it is possible to design, model, and fabricate with a great degree of confidence cone-shaped step-index optical fibers with numerical apertures from 0.09 to 0.88 in air.

6. Fiber Optics Point-Source for Digital Lensless Holographic Microscopy

Based on principle of holography proposed by Gabor in 1948 [53], digital holographic microscopy (DHM) constitutes a powerful tool for a wide range of applications [51], [108]. This technique allows three-dimensional sample imaging by numerical refocusing of a two-dimensional image at different object planes without using any opto-mechanical movement [9], [42]. Due to its versatility, DHM is applied to real-time phase contrast imaging [109], polarization microscopy imaging [110], three-dimensional dynamic analysis of cells [111], and particle tracking [112], among others.

Digital in-line holography with spherical waves is the simplest realization of DHM. As it works without lenses [9], this configuration is usually known as Digital Lensless Holographic Microcopy (DLHM). Due to this experimental configuration simplicity, much research has been recently undertaken on DLHM. In this technique, a point-source and a digital recording system are the only hardware elements required to obtain both the phase and the amplitude information of microscopic specimens[9], [113]. Optimizing each of these systems has been a technological challenge around which a wide field of research has been developed over recent decades. Particularly in the case of the light source, illumination of the specimen with spherical waves is required to obtain the magnification of the diffraction pattern in the recording process of the hologram [45].

A traditional DLHM setup uses a monochromatic light source, usually a laser of wavelength λ, that is focused into a pinhole of linear dimensions in the order of λ to generate the spherical waves. Although in theory, the pinhole illumination system is a very simple method

to generate the spherical waves, in practice, implementation of this system in DLHM is very cumbersome. In addition to the difficult and expensive manufacture process, the main experimental difficulty of pinholes is due to the rigorous alignment process; which many times requires using ultra-precise opto-mechanical elements [112]. In response to these difficulties and taking advantage of the good features of the optical fibers such as the flexibility, low cost, and relative ease of coupling light, a cone-shaped optical fiber tip as illumination source for DLHM is proposed in this work.

Cone-shaped optical fibers modify the way how light emerges from the optical fiber in such a way that said distal end can be implemented as a point source of spherical waves [14]. Some microscopy techniques incorporate cone-shaped optical fibers as scanning probes. In particular, near-field scanning optical microscopy (NSOM) uses these kind of probes to scan the sample by illuminating a nanometric local area and detecting the transmitted or reflected light in the near field zone [24], [26], [90], [91]. Another technique that employs cone-shaped optical fibers is called photon scanning tunnelling microscope (PSTM) [37], [92]. This latter technique is analogous to the electron scanning tunnelling microscopy (ESTM), but with the difference that it involves tunnelling of photons instead of electrons from the sample surface to the cone-shaped fiber.

In referring to DLHM, an exhaustive search of literature related to the development and implementation of a point-source based on cone-shaped optical fibers did not match any scientific journal or conference proceeding article; with the exception of a brief description reported elsewhere [39]. Owing to the aforementioned flaws attributable to the pinhole illumination systems in DLHM, this chapter evaluates the point-source based on optical fibers for DLHM able to produce comparable results to those obtained by conventional pinhole illumination systems.

6.1 Resolution Characterization of the DLHM with cone tip optical fibers as illumination source.

Once the numerical aperture measurements have been completed, the next objective is to implement the fibers with cone tip as point sources of spherical waves for Digital Lensless Holographic Microscopy. To achieve this, the experimental setup shown in Figure 6-1 was used to generate diffraction patterns, or holograms, illuminating a sample with the optical fiber point-source.
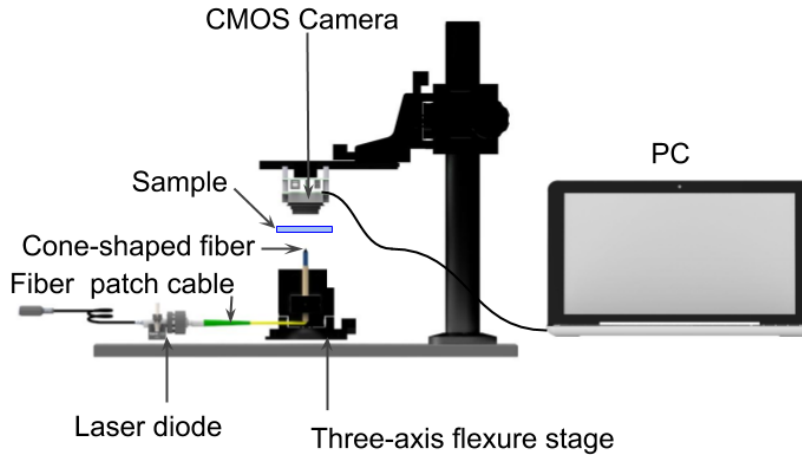
Figure 6-1: Experimental arrangement of the DLHM.

As discussed in Section 2.4.3, according to the Rayleigh criterion two point sources are just resolved when the first diffraction maximum of one coincides with the first diffraction minimum of the other. In the case of DLHM, this criteria is applied by taking as a model an ideal point source that emits a spherical wave, and two objects at positions $\vec{r}_1$ and $\vec{r}_2$. According this model, two points can be laterally resolved if their lateral separation satisfies the following equation:

$$|\vec{r}_2 - \vec{r}_1| \geq \frac{\lambda}{2NA}. \tag{6.1}$$
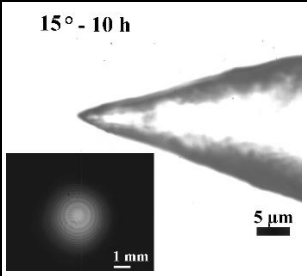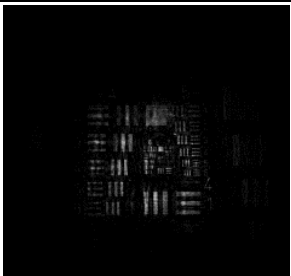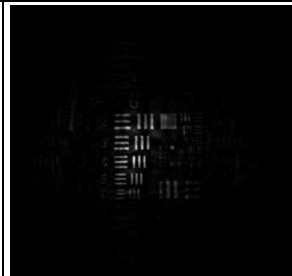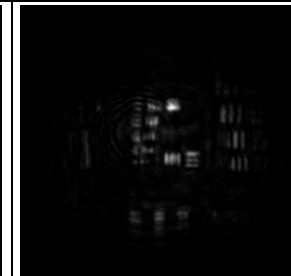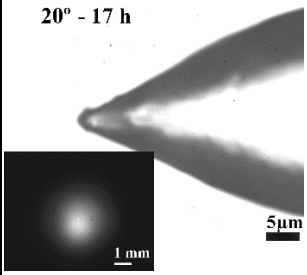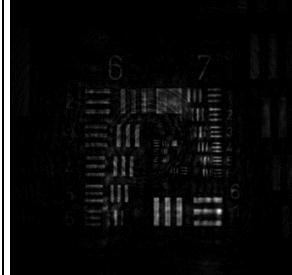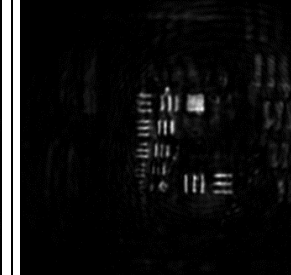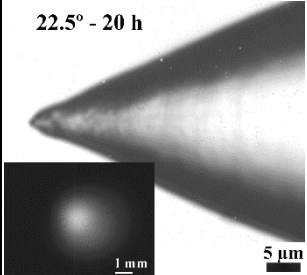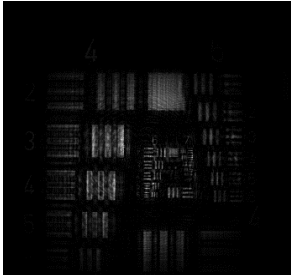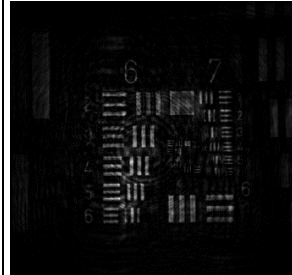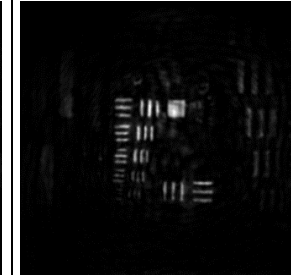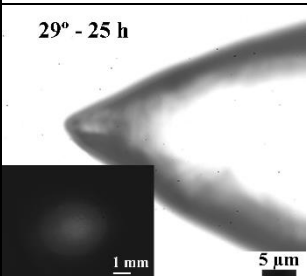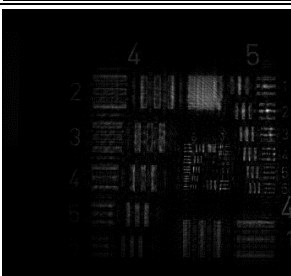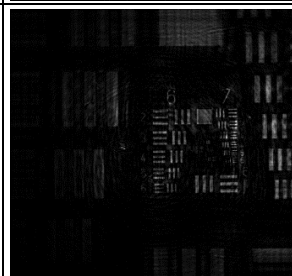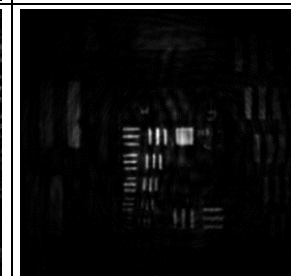
Where NA must be taken as the one with the lowest value between the NA of the illumination source and the NA of the recording setup [114].

According to Equation (6.1), the resolution of the DLHM can be determined knowing the distance between two very close sample objects, and the NA values of the cone tip used as point source. In order to achieve this, a resolution test pattern (1951 USAF resolution test chart) was used as sample in the DLHM and a series of images was reconstructed sweeping the groups 4 (16 lp/mm) to 9 (645 lp/mm). Here, lp/mm stands for line pairs per mm.

Table 6-1 presents in columns 2 to 4 the results of the reconstructed images of the positive USAF 1951 Hi-Resolution target for each of the fabricated cone-shaped optical fibers. It can be observed that the cone-shaped fiber with an etching time of 10 h (NA=0.14) can

resolve all the elements of groups 4 to 7, with distances between lines ranging from 17 μm to 2 μm; which is in agreement with (6.1). However, groups 8 and 9 (with a distance between lines smaller than 0.9 μm) cannot be resolved. On the other hand, for cone tips with etching time of 17 h (NA=0.47), 20 h (NA=0.57), and 25 h (NA=0.88) all elements from the groups 4 to 9, with distance between lines ranging from 17 μm to 0.55 μm, can be clearly resolved.

Table 6-1:   Reconstructed images of the positive USAF 1951 test target for each of the cone tips as point-source for DLHM.

Cone Tip	USAF Groups 4 and 5	USAF Groups 6 and 7	USAF Groups 8 and 9
15° - 10 h			
20° - 17 h			
22.5° - 20 h			
29° - 25 h			

6.2 Cone-shaped optical fibers as alternative to pinhole illumination in DLHM.

6.2.1 Spherical frontwave analysis

To analyze the wavefront produced by the cone-shaped optical fibers, the phase of the intensity distribution of the spots in column 1 of Table 6-1 was numerically reconstructed. The phase distribution acquired directly is limited from π to -π, which is called wrapped phase. It must be unwrapped to retrieve the nature phase employing a suitable phase unwrapping algorithm. Figure 6-2 shows in (a) the distribution of wrapped phase, and in (b) the three-dimensional representation of the corresponding unwrapped phase distribution, calculated by Quality Guided Phase Unwrapping algorithm (QGPU) [115], for the wavefront of the cone-shaped optical fiber with NA=0.47. The obtained results are comparable to other analysis of spherical wavefronts, such as those reported in [116], [117]; confirming that the generated wavefront emmited by the cone-shaped optical fiber engineered in this dissertation is spherical.

(a)   (b)
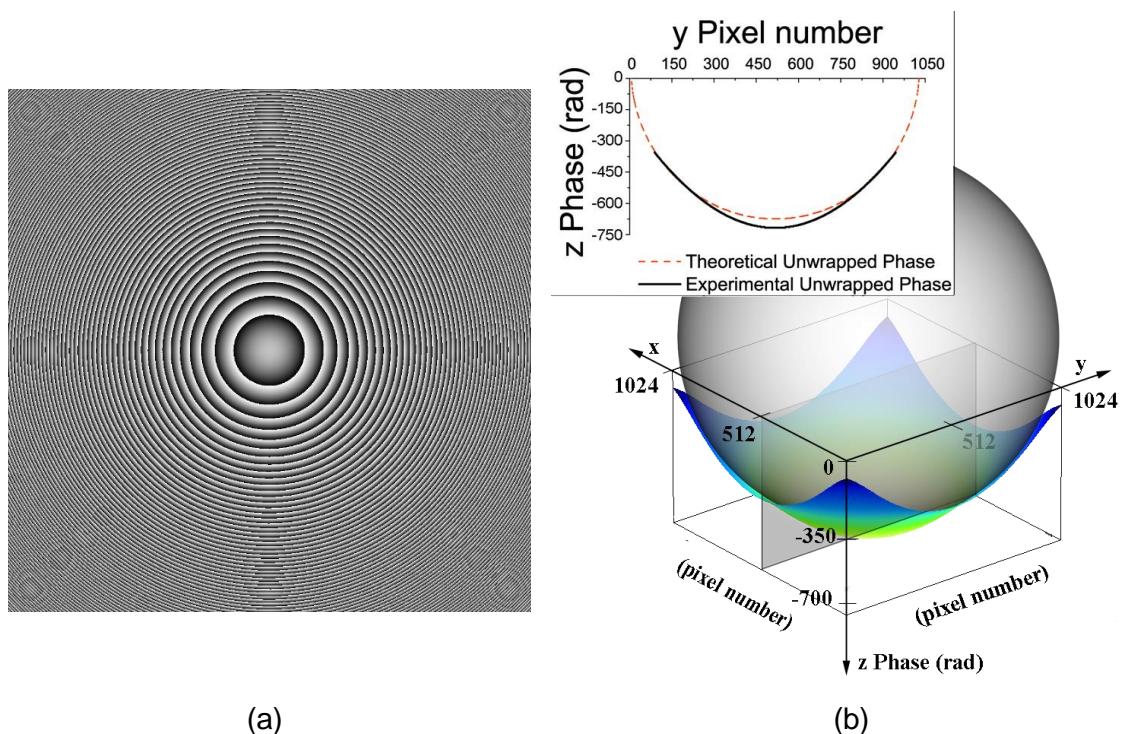
Figure 6-2:   Analysis of the spherical wavefront produced by a cone-shaped optical fiber with NA= 0.47. (a) Phase reconstruction, and (b) Three-dimensional representations of the unwrapped distribution of phase.

6.2.2 Cone-shaped optical fiber versus pinhole

The feasibility of the cone-shaped optical fibers as a technological alternative point source for DLHM requires the comparisson with the pinhole illumination system. The 1951 USAF hi-resolution target was used as sample using as illumination point-source both, a cone-shaped optical fiber with NA=0.47 and a pinhole with NA=0.47 (National Aperture, Inc™ diameter 2λ). Images were taken using the same groups in the resolution target with both illumination sources and summarized in **Table 6-2**. The results of the reconstructed images of groups 4 to 9 (16 lp/mm to 645 lp/mm) are readily comparable. This is very encouraging and support the viability of using engineered optical fibers as a technological alternative to the pinhole illumination system for DLHM. Furthermore, features of the optical fibers such as the installation flexibility, low cost, good overall durability, low weight, and the ease of coupling light by connecting it to a laser or a LED diode, constitute advantages over the pinhole illumination.
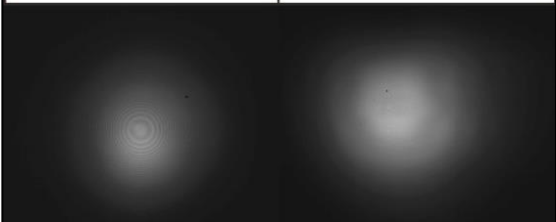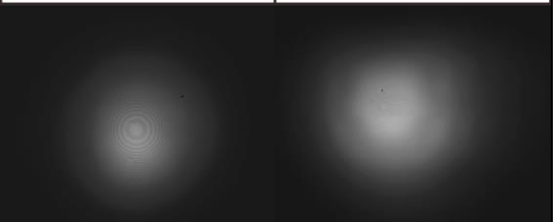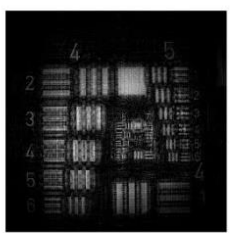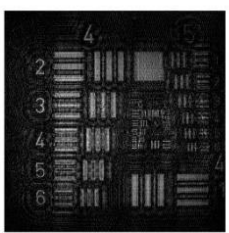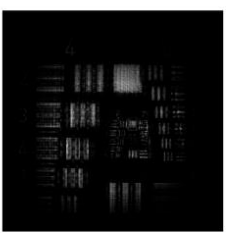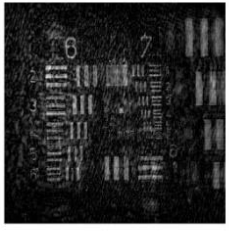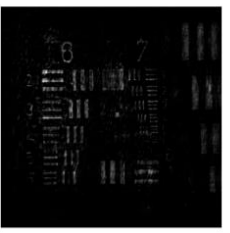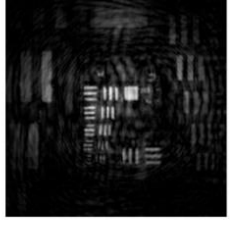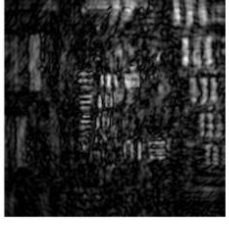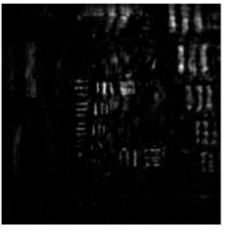
6.2.3 Non-bio and bio imaging with cone-shaped optical fiber point-source in DLHM

Finally, to demonstrate the capabilities of DLHM with cone-shaped optical fibers as point-source illumination, some non-biological and biological sample images were imaged. DLHM images of an acupuncture needle using cone-shape optical fibers as point-sources were taken. Figure 6-3 (a) and (b) show the images obtained using cone-shaped optical fibers with NA of 0.15 and 0.44, respectively. In agreement with Equation (6.1), these images show that the lateral resolution achieved by those NAs is capable of distinguish fine details of the roughness on the tip of the needle.

Culminating this study of the optical fiber as a point source,

shows the reconstructed image for a paraffin wax section of the head of a fruit fly (Drosophila melanogaster). The section is about 900 μm wide and the sample has a thickness on the order of 8 μm. This image was obtained using a cone-shaped optical fiber with NA=0.44 implemented as point-source in DLHM. Very fine details, such as the bristles which form the structure of the compound eye of the Drosophila melanogaster, are visible. These result show the capability of DLHM with cone-shaped optical fiber to image micrometer-sized structures.

Table 6-2: Reconstructed images in amplitude (left) and intensity (right) of the positive USAF 1951 using a cone tip and a pinhole both with NA=0.45.

(a)   (b)

Figure 6-3:   DLHM reconstructed images of an acupuncture needle's tip using cone-shaped optical fibers of (a) NA=0.15 and (b) NA=0.44
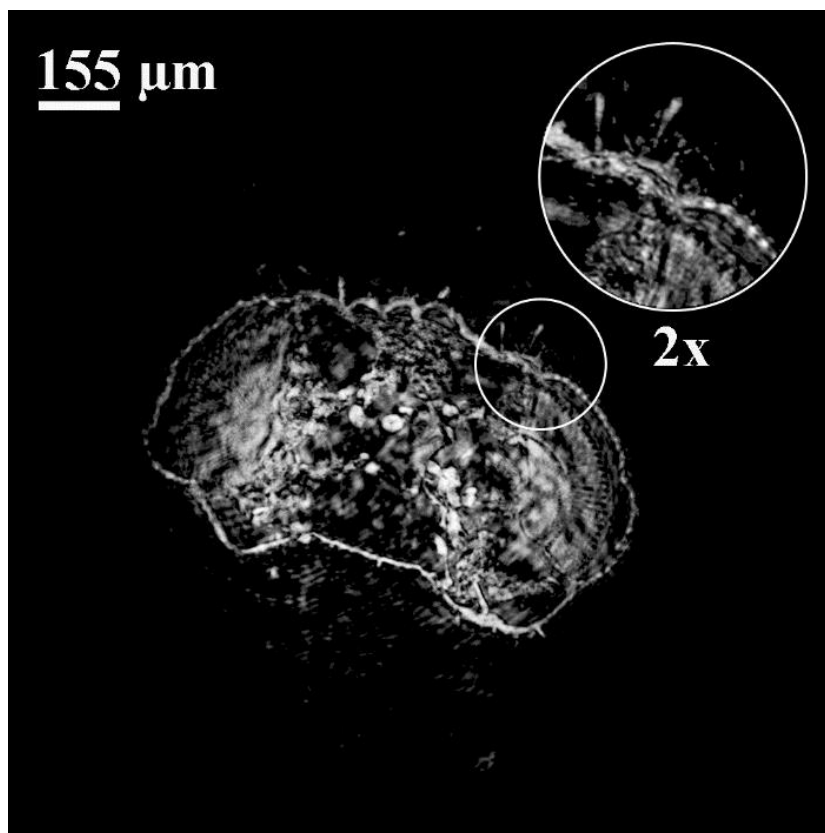
Figure 6-4: Reconstructed image for a section of the head of a Drosophila Melanogaster fly using a cone tip with NA=0.88.

7. Conclusions y recommendations

7.1 Conclusions

In this dissertation, a light source alternative to traditional pinhole illumination system for digital holographic microscopy lensless (DLHM) was developed from the use of step-index optical fibers. The hypothesis along this work was to determine whether step-index optical fibers could be used as point source for DLHM.

As mentioned in Equation (2.46), the resolution achievable by a DLHM system depends both on the numerical aperture and the light wavelength used to illuminate the sample. Light wavelengths cannot be modified without a tradeoff in the detection system. Leaving the only feasible option to use the highest possible numerical aperture (NA) in the optical fiber to be used as illumination source.

NA in a clean cleaved optical fiber, as shown in Equation (3.3), is a function of the difference in refractive indexes of the core and cladding of the fiber. The NA determines the angle of the cone of acceptance or the cone of emission. Since the NA of a clean cleaved step-index optical fibers is rather small (maximum up to 0.35 for high-NA fibers), and modifying the refractive indexes of the optical fiber was not a cost-efective option, the only option left was to modify the geometry of the optical fiber at the distal end, changing the way in which light emerges from it.

To test this hypothesis, analytical expressions to tailor the numerical aperture of cone-shaped step optical fibers were proposed as a first stage. The expressions obtained were derived from the geometrical study of light-ray tracing at the cone-shaped tip of a regular step-index optical fiber. The analysis of the different physical phenomena that can take place at the cone tip immersed in different surrounding media, as a function of the cone

angle at the end of the fiber, led to theoretical numerical apertures up to 1.00 for air, 1.33 for water, and 1.5 for immersion oil. These NA values can be achieved via a variety of cone angles, providing great versatility in the design of light sources or light collecting devices based on step-index optical fibers. The initial results of this stage were presented at the OSA Latin American Optics and Photonics conference LAOP 2018 held in November 12-15 in Lima (Peru) [118]. The final results were compiled in a research article submitted to Heliyon Journal (Elsevier), which is currently in the second round of peer reviewers after being suggested minor changes in the first reviewing stage.

As a second stage, both ray-tracing and wave-optics propagation analysis were performed using COMSOL to model the numerical apertures that can be achieved for step-index optical fibers by modifying the cone angle at their distal end. The concurrence between the analytical equations found in the first stage and the modeling results shows that it is possible to design, with a great degree of confidence, cone-shaped step-index optical fibers with numerical apertures from 0.09 to 0.88 in air. The results of this stage were consolidated in a research article submitted to the Journal of Lightwave Technology (OSA-IEEE), which is currently in the second round of peer reviewers after being suggested minor changes in the first reviewing stage.

In order to test the findings from the analytical and numerical stages, a fabrication method to obtain cone-shaped optical fibers was developed and thoroughly described in this dissertation in Chapter 0.The geometrical characteristics of chemically etched cone-shaped fibers were studied considering the effect of etchant diffusion for prolonged times. Tips with shorter tapers, very smooth surface, and larger conical angles than ever reported in the literature, were obtained from single-mode optical fibers using hydrofluoric acid solution as etchant and a cover-layer of vegetable oil. The results of this stage are being compiled in a research article to be submitted to a peer-reviewed journal.

Finally, the cone-shaped optical fibers fabricated in the experimental stage were used as point sources of spherical waves for Digital Lensless Holographic Microscopy in an experimental setup where the diffraction pattern (hologram) from real samples was recorded and reconstructed. Being able to reconstruct images in the same fashion as when using pinholes as point source proved that optical fibers can be used as point source for DLHM. To demonstrate that the emmited wavefront from the cone-shaped optical fibers engineered in this dissertation was effectively spherical, a phase unwrapping algorithm was

implemented, allowing for a plot of the phase to be plotted. The obtained surface at this stage is beyond the expectations and proves the feasibility of generating spherical wavefronts from single-mode optical fibers.

In addition, testing fibers with different cone angles at the distal end as point source allowed samples to be imaged with various optical resolutions. This result confirms that the numerical aperture of cone-shaped optical fibers can be tailored by controlling the etching time during the fabrication stage. This ability to tailor the numerical aperture allowed the dependence of the resolution on the numerical aperture of the cone-shape optical fibers to be corroborated. The initial results from this stage where the optical fibers were used as illumination sources were submitted and accepted to be presented at the OSA Digital Holography and 3-D Imaging conference to be hold in May 19th-23rd, 2019 in Bordeaux, France. The complete results of the digital holographic microscope using optical fibers as point source were also compiled and submitted as part of the OSA-IEEE Journal of Lightwave Technology Journal's special issue on Imaging and Illumination with Optical Fiber, which is currently in the second round of peer reviewers after being suggested minor changes in the first reviewing stage.

The comparative analysis of the engineered cone-shaped optical fibers with respect to the conventional pinhole illumination system is very encouraging and supports the viability of using optical fibers as an alternative for the illumination in DLHM. In fact, the good features of the optical fibers constitute advantages over the pinhole illumination. Furthermore, the capability of DLHM with cone-shaped optical fiber to image micrometer-sized structures was shown in this dissertation.

7.2 Recommendations

As additional stages to the research undertaken in this dissertation, the following is recommended:

1. To complete the characterization of the illumination and the resolution obtained from using cone-shaped optical fibers with small cone semi-angles (less than 15°). Although these cone tips were easier to fabricate in very little time, the illumination obtained with them was not useful for Digital Lensless Holographic Microscopy up

to the current standards desired in the research group. The reason why these small cone tips are not adequate for achieving the resolution desired can be explained by the fact that small angles are formed during the first 7 hours of static chemical etching, and it is the effect of etchant diffusion which produces not only larger conical angles but smoother conical surface. Thus, the diffusion effect is only appreciable after prolonged etching times. However, these cones could be used as a quick and cheap alternative to image larger samples that do not require high resolution, for instance to develop a portable DLHM to test the presence of microorganisms in drinking water.

2. To complete the resolution characterization of the cone-shaped optical fibers fabricated with large numerical apertures. That is, image samples beyond the 645 lp/mm that the available USAF 1951 test target can provide. To achieve this, a high resolution test target with a minimum feature size of 274 nanometer bar width is advisable to determine the maximum resolution capacity of the Digital Lensless Holographic Microscopy with the developed cone-shaped optical fibers as point-source.

Bibliography

[1]   B. Huang, H. Babcock, and X. Zhuang, "Breaking the diffraction barrier: Super-resolution imaging of cells," *Cell*, 2010.

[2]   E. Betzig, J. K. Trautman, T. D. Harris, J. S. Weiner, and R. L. Kostelak, "Breaking the diffraction barrier: Optical microscopy on a nanometric scale," *Science (80-.).*, 1991.

[3]   S. K. Buratto, "Near-field scanning optical microscopy," *Curr. Opin. Solid State Mater. Sci.*, 1996.

[4]   B. Price, "Electron Microscopy, Second Edition, John J. Bozzola and Lonnie D. Russell. Jones and Bartlett Publishers, Inc., Sudbury, MA, 1999, 670 pages (hardback, $56.25). ISBN 0-7637-0192-0," *Microsc. Microanal.*, 2002.

[5]   W. R. Bowen and N. Hilal, *Atomic Force Microscopy in Process Engineering*. 2009.

[6]   J. A. Stroscio and W. J. Kaiser, *Scanning tunneling microscopy*, vol. 27. Academic Press, 1993.

[7]   A. Cornea and P. M. Conn, *Fluorescence Microscopy: Super-Resolution and other Novel Techniques*. 2014.

[8]   M. K. Kim, *Digital Holographic Microscopy: Principles, Techniques, and Applications*. 2011.

[9]   J. Garcia-Sucerquia, W. Xu, S. K. Jericho, P. Klages, M. H. Jericho, and H. J. Kreuzer, "Digital in-line holographic microscopy," *Appl. Opt.*, 2006.

[10]   J. Garcia-Sucerquia, "Microscopía holográfica digital sin lentes con resolución micrométrica y fuentes multiespectrales," *Rev. la Acad. Colomb. Ciencias Exactas, Físicas y Nat.*, 2015.

[11]   J. Garcia-Sucerquia, W. Xu, S. K. Jericho, M. H. Jericho, and H. J. Kreuzer, "4-D imaging of fluid flow with digital in-line holographic microscopy," *Optik (Stuttg).*, 2008.

[12]   E. Udd and W. B. Spillman, *Fiber Optic Sensors: An Introduction for Engineers and Scientists: Second Edition*. 2011.

[13]   G. Kostovski, P. R. Stoddart, and A. Mitchell, "The optical fiber tip: An inherently light-coupled microscopic platform for micro- and nanotechnologies," *Advanced Materials*. 2014.

[14]   N. I. Chkhalo, A. Y. Klimov, V. V. Rogov, N. N. Salashchenko, and M. N. Toropov, "A source of a reference spherical wave based on a single mode optical fiber with a narrowed exit aperture," *Rev. Sci. Instrum.*, 2008.

[15]   E. Betzig, A. Lewis, A. Harootunian, M. Isaacson, and E. Kratschmer, "Near Field

Scanning Optical Microscopy (NSOM): Development and Biophysical Applications," *Biophys. J.*, 1986.

[16] M. Garcia-Parajo, E. Cambril, and Y. Chen, "Simultaneous scanning tunneling microscope and collection mode scanning near-field optical microscope using gold coated optical fiber probes," *Appl. Phys. Lett.*, 1994.

[17] B. I. Yakobson, A. LaRosa, H. D. Hallen, and M. A. Paesler, "Thermal/optical effects in NSOM probes," *Ultramicroscopy*, 1995.

[18] P. Hoffmann, B. Dutoit, and R. P. Salathé, "Comparison of mechanically drawn and protection layer chemically etched optical fiber tips," *Ultramicroscopy*, vol. 61, no. 1–4, pp. 165–170, 1995.

[19] G. A. Valaskovic, M. Holton, and G. H. Morrison, "Parameter control, characterization, and optimization in the fabrication of optical fiber near-field probes," *Appl. Opt.*, 1995.

[20] Z. L. Ran, Y. J. Rao, W. J. Liu, X. Liao, and K. S. Chiang, "Laser-micromachined Fabry-Perot optical fiber tip sensor for high-resolution temperature-independent measurement of refractive index," *Opt. Express*, 2008.

[21] R. S. Taylor, C. Hnatovsky, E. Simova, D. M. Rayner, V. R. Bhardwaj, and P. B. Corkum, "Femtosecond laser fabrication of nanostructures in silica glass," *Opt. Lett.*, 2003.

[22] Y. Ju, H. Sato, and H. Soyama, "Fabrication of the tip of GaAs microwave probe by wet etching," in *ASME 2005 Pacific Rim Technical Conference and Exhibition on Integration and Packaging of MEMS, NEMS, and Electronic Systems collocated with the ASME 2005 Heat Transfer Summer Conference*, 2005, pp. 1919–1922.

[23] H. Nikbakht, H. Latifi, M. Oraie, and T. Amini, "Fabrication of tapered tip fibers with a controllable cone angle using dynamical etching," *J. Light. Technol.*, vol. 33, no. 23, pp. 4707–4711, 2015.

[24] P. Lambelet, A. Sayah, M. Pfeffer, C. Philipona, and F. Marquis-Weible, "Chemically etched fiber tips for near-field optical microscopy: a process for smoother tips," *Appl. Opt.*, vol. 37, no. 31, p. 7289, 1998.

[25] A. Barucci *et al.*, "Optical fibre nanotips fabricated by a dynamic chemical etching for sensing applications," *J. Appl. Phys.*, 2015.

[26] P. Burgos *et al.*, "Near-field scanning optical microscopy probes: A comparison of pulled and double-etched bent NSOM probes for fluorescence imaging of biological samples," *J. Microsc.*, 2003.

[27] Y. K. Cheong, K. S. Lim, W. H. Lim, W. Y. Chong, R. Zakaria, and H. Ahmad, "Note: Fabrication of tapered fibre tip using mechanical polishing method," *Rev. Sci. Instrum.*, vol. 82, no. 8, pp. 26–29, 2011.

[28] J. P. Clarkin, R. J. Timmerman, and J. H. Shannon, "Shaped fiber tips for medical and industrial applications," in *Optical fibers and sensors for medical applications IV*, 2004, vol. 5317, pp. 70–81.

[29]   R. M. Verdaasdonk and C. Borst, "{R}ay tracing of optically modified fiber tips. 2: laser scalpels," *Appl. Opt.*, 1991.

[30]   R. M. Verdaasdonk and C. Borst, "Ray tracing of optically modified fiber tips. 1: spherical probes," *Appl. Opt.*, vol. 30, no. 16, pp. 2159–2171, 1991.

[31]   L. Lilge, L. Vesselov, and W. Whittington, "Thin cylindrical diffusers in multimode Ge-doped silica fibers," *Lasers Surg. Med.*, 2005.

[32]   Y. D. Suh and R. Zenobi, "Improved probes for scanning near-field optical microscopy," *Adv. Mater.*, vol. 12, no. 15, pp. 1139–1142, 2000.

[33]   M. Xiao, R. Machorro, J. Siqueiros, and H. Escamilla, "Fabrication of probe tips for reflection scanning near-field optical microscopes: Chemical etching and heating-pulling methods," *J. Vac. Sci. Technol. B Microelectron. Nanom. Struct.*, vol. 15, no. 4, p. 1516, 1997.

[34]   S. Patanè, E. Cefalì, A. Arena, P. G. Gucciardi, and M. Allegrini, "Wide angle near-field optical probes by reverse tube etching," *Ultramicroscopy*, vol. 106, no. 6, pp. 475–479, 2006.

[35]   L. Novotny, D. W. Pohl, and B. Hecht, "Scanning near-field optical probe with ultrasmall spot size," *Opt. Lett.*, vol. 20, no. 9, p. 970, 1995.

[36]   R. C. Reddick, R. J. Warmack, D. W. Chilcott, S. L. Sharp, and T. L. Ferrell, "Photon scanning tunneling microscopy," *Rev. Sci. Instrum.*, 1990.

[37]   A. Klini *et al.*, "Reproducible optical fiber tips for photon scanning tunneling microscopy with very small (<5°) cone angle," *J. Light. Technol.*, vol. 16, no. 7, pp. 1220–1227, 1998.

[38]   S. I. Hosain, Y. Lacroute, and J. P. Goudonnet, "A simple low-cost highly reproducible method of fabricating optical fiber tips for a photon scanning tunneling microscope," *Microw. Opt. Technol. Lett.*, 1996.

[39]   M. Schürmann, "Digital In-Line Holographic Microscopy with Various Wavelengths and Point Sources Applied to Static and Fluidic Specimens," *Physics (College. Park. Md).*, 2007.

[40]   "A dynamical theory of the electromagnetic field," *Nature*. 1927.

[41]   J. W. Goodman, *Introduction to Fourier Optics, Third Edition*. 2005.

[42]   U. Schnars, C. Falldorf, J. Watson, and W. Jüptner, *Digital holography and wavefront sensing: Principles, techniques and applications*. 2015.

[43]   H. J. Kreuzer, M. H. Jericho, I. A. Meinertzhagen, and W. Xu, "Digital in-line holography with numerical reconstruction: 4D tracking of microstructures and organisms," *Pract. Hologr. Xvii Hologr. Mater. Ix*, vol. 5005, no. 902, pp. 299–306, 2003.

[44]   C. A. Trujillo and J. Garcia-Sucerquia, "Automatic method for focusing biological specimens in digital lensless holographic microscopy," *Opt. Lett.*, 2014.

[45] J. Garcia-Sucerquia, "Color lensless digital holographic microscopy with micrometer resolution," *Opt. Lett.*, 2012.

[46] K. Iizuka, *Engineering Optics*. 2008.

[47] A. M??ndez and T. F. Morse, *Specialty Optical Fibers Handbook*. 2007.

[48] K. Thyagarajan and A. Ghatak, "Optical Fiber," in *Fiber Optic Essentials*, 2007.

[49] K. Kawano and T. Kitoh, *Introduction to Optical Waveguide Analysis: Solving Maxwell's Equation and the Schrödinger Equation*. John Wiley & Sons, 2004.

[50] E. Hecht, *Optics, 4th edition*. 2001.

[51] M. K. Kim, "Digital holographic microscopy," *Springer Ser. Opt. Sci.*, 2011.

[52] P. Hariharan and P. Hariharan, *Optical Holography: Principles, techniques and applications*. Cambridge University Press, 1996.

[53] D. GABOR, "A New Microscopic Principle," *Nature*, 1948.

[54] R. K. Kostuk, "Optical Holography," in *Photonics: Scientific Foundations, Technology and Applications*, 2015.

[55] H. J. Kreuzer, M. H. Jericho, I. A. Meinertzhagen, and W. Xu, "Digital in-line holography with numerical reconstruction: 4D tracking of microstructures and organisms," in *Practical Holography Xvii and Holographic Materials Ix*, 2003.

[56] H. Lichte and M. Lehmann, "Electron holography - Basics and applications," *Reports Prog. Phys.*, 2008.

[57] M. Howellst and C. Jacobsen, "Soft X-ray Microscopes and their Biological Applications," *Q. Rev. Biophys.*, 1995.

[58] L. Denis, C. Fournier, T. Fournel, and C. Ducottet, "Numerical suppression of the twin image in in-line holography of a volume of micro-objects," *Meas. Sci. Technol.*, 2008.

[59] M. H. Jericho and H. J. Kreuzer, "Point source digital in-line holographic microscopy," *Springer Series in Surface Sciences*. 2011.

[60] H. J. Kreuzer, "Holographic microscope and method of hologram reconstruction," 2002.

[61] G. Smith, T. King, and D. Wilkins, *Optics and Photonics : An Introduction*. 2007.

[62] W. Lauterborn and T. Kurz, *Coherent optics: fundamentals and applications*. Springer Science & Business Media, 2003.

[63] N. Hodgson and H. Weber, *Laser Resonators and Beam Propagation: Fundamentals, Advanced Concepts, Applications*, vol. 108. Springer, 2005.

[64] Vincent Toal, "Introduction to Holography - Vincent Toal - Google Books," *Crc*, 2012. .

[65]   W. J. Wadsworth *et al.*, "Very High Numerical Aperture Fibers," *IEEE Photonics Technol. Lett.*, 2004.

[66]   P. G. Yan *et al.*, "Supercontinuum generation in a photonic crystal fibre," *Chinese Phys. Lett.*, 2004.

[67]   Y. Xu, X. Zhang, S. Hou, M. Liu, H. Wang, and D. Ling, "Supercontinuum generation in photonic crystal fiber with all-normal group velocity dispersion," in *2012 International Conference on Wireless Communications, Networking and Mobile Computing, WiCOM 2012*, 2012.

[68]   K. Maslov, G. Stoica, and L. V. Wang, "In vivo dark-field reflection-mode photoacoustic microscopy," *Opt. Lett.*, 2005.

[69]   J. Joannopoulos, S. Johnson, and J. Winn, *Photonic crystals: molding the flow of light.* 2008.

[70]   J. C. Knight, "Photonic crystal fibres," *Nature*, vol. 424, no. 6950, p. 847, 2003.

[71]   T. A. Birks, J. C. Knight, and P. S. J. Russell, "Endlessly single-mode photonic crystal fiber," *Opt. Lett.*, 1997.

[72]   G. E. Town and J. T. Lizier, "Tapered holey fibers for spot-size and numerical-aperture conversion," *Opt. Lett.*, 2001.

[73]   R. M. Verdaasdonk and C. M. D. Borst, "Optical characteristics of sapphire laser scalpels analysed by ray-tracing," in *Proceedings of SPIE - The International Society for Optical Engineering*, 1991.

[74]   R. M. Verdaasdonk and C. Borst, "Laser Scalpels," *Appl. Opt.*, 1991.

[75]   B. I. Yakobson, P. J. Moyer, and M. A. Paesler, "Kinetic limits for sensing tip morphology in near-field scanning optical microscopes," *J. Appl. Phys.*, 1993.

[76]   H. Nikbakht, H. Latifi, T. Amini, and Z. Chenari, "Controlling cone angle of the tapered tip fiber using dynamic etching," vol. 9157, p. 91574Q, 2014.

[77]   W. Yihong, Y. Zhiyong, Y. Tan, G. Ning, and K.-D. Wesche, "Effect of Etchant Diffusion on Tip Profiles of Glass Fiber Probes," *J. Nanosci. Nanotechnol.*, vol. 6, no. 4, pp. 1185–1187, 2006.

[78]   A. Klini *et al.*, "Reproducible optical fiber tips for photon scanning tunneling microscopy with very small (<5°) cone angle," *J. Light. Technol.*, 1998.

[79]   S. Savović, M. S. Kovačević, A. Djordjevich, J. S. Bajić, D. Z. Stupar, and G. Stepniak, "Mode coupling in low NA plastic optical fibers," *Opt. Laser Technol.*, 2014.

[80]   A. Djordjevich, S. Savović, P. W. Tse, B. Drljaca, and A. Simović, "Mode coupling in strained and unstrained step-index plastic optical fibers," *Appl. Opt.*, 2010.

[81]   COMSOL Multiphysics, "COMSOL Multiphysics." [Online]. Available: https://www.comsol.com/. [Accessed: 26-Mar-2019].

[82] COMSOL, "Introduction to COMSOL Multiphysics 5.0," *Manual*, 2010. [Online]. Available: http://cdn.comsol.com/documentation/5.0.1.276/IntroductionToCOMSOLMultiphysics.pdf. [Accessed: 28-Mar-2019].

[83] COMSOL Multiphysics, "Application Gallery:Step-Index Fiber." [Online]. Available: https://www.comsol.com/model/step-index-fiber-145. [Accessed: 26-Mar-2019].

[84] COMSOL Multiphysics, "Application Gallery: 3D Wave Propagation in Silicon Waveguide with Rib and Slot Configurations." [Online]. Available: https://www.comsol.com/model/3d-wave-propagation-in-silicon-waveguide-with-rib-and-slot-configurations-70551. [Accessed: 26-Mar-2019].

[85] ImageJ, "ImageJ User Guide," *Nat. Methods*, 2012.

[86] L. Meng, Q. Kong, K. Ji, Z. Han, H. Shen, and R. Zhu, "Characterization of beam quality of unstable laser beams with the multiple hyperbolas method," *Results Phys.*, 2019.

[87] S. Choudhary *et al.,* "Measurement of the radial mode spectrum of photons through a phase-retrieval method," *Opt. Lett.*, vol. 43, no. 24, pp. 6101–6104, 2018.

[88] L. Mandel, E. Wolf, and P. Meystre, "Optical Coherence and Quantum Optics," *Am. J. Phys.*, 1996.

[89] D. Courjon and C. Bainier, "Near field microscopy and near field optics," *Reports on Progress in Physics*. 1994.

[90] S. K. Mondal, A. Mitra, N. Singh, S. N. Sarkar, and P. Kapur, "Optical fiber nanoprobe preparation for near-field optical microscopy by chemical etching under surface tension and capillary action," *Opt. Express*, vol. 17, no. 22, p. 19470, 2009.

[91] A. Lazarev, N. Fang, Q. Luo, and X. Zhang, "Formation of fine near-field scanning optical microscopy tips. Part I. By static and dynamic chemical etching," *Rev. Sci. Instrum.*, 2003.

[92] T. Pangaribuan, K. Yamada, S. Jiang, M. Ohtsu, and H. Ohsawa, "Reproducible fabrication technique of nanometric tip diameter fiber probe for photon Scanning Tunneling Microscope," *Jpn. J. Appl. Phys.*, vol. 31, no. 9, pp. L1302–L1304, 1992.

[93] M. Insinna *et al.,* "Dynamical chemical etching for fabrication of optical fibre nanotips," *2015 Fotonica AEIT Ital. Conf. Photonics Technol.*, pp. 1–4, 2015.

[94] W. Zhu, T. Shi, Z. Tang, B. Gong, G. Liao, and J. Tully, "Dynamic selective etching: a facile route to parabolic optical fiber nano-probe," *Opt. Express*, vol. 21, no. 6, p. 6919, 2013.

[95] S. Mononobe and M. Ohtsu, "Fabrication of a pencil-shaped fiber probe for near-field optics by selective chemical etching," *J. Light. Technol.*, 1996.

[96] M. Tao, Y. Jin, N. Gu, and L. Huang, "A method to control the fabrication of etched optical fiber probes with nanometric tips," *J. Opt. A Pure Appl. Opt.*, vol. 12, no. 1, 2010.

[97]   D. R. Turner, "Etch procedure for optical fibers." Google Patents, 1984.

[98]   N. E. Dickenson, E. S. Erickson, O. L. Mooren, and R. C. Dunn, "Characterization of power induced heating and damage in fiber optic probes for near-field scanning optical microscopy," *Rev. Sci. Instrum.*, 2007.

[99]   C. Phipps, *Laser ablation and its applications*, vol. 129. Springer, 2007.

[100]   COMSOL Multiphysics, "Application Gallery: Chemical Etching." [Online]. Available: https://www.comsol.com/model/chemical-etching-44481. [Accessed: 26-Mar-2019].

[101]   D. J. Monk, D. S. Soane, and R. T. Howe, "A diffusion/chemical reaction model for HE etching of LPCVD phosphosilicate glass sacrificial layers," in *Technical Digest IEEE Solid-State Sensor and Actuator Workshop*, 1992, pp. 46–49.

[102]   A. Lazarev, N. Fang, Q. Luo, and X. Zhang, "Formation of fine near-field scanning optical microscopy tips. Part I. By static and dynamic chemical etching," *Rev. Sci. Instrum.*, vol. 74, no. 8, pp. 3679–3683, 2003.

[103]   U. . N. I. of Health, "ImageJ," *2015*. [Online]. Available: https://imagej.nih.gov/ij/index.html. [Accessed: 28-Mar-2019].

[104]   S. Q. Mawlud and N. Q. Muhamad, "Theoretical and experimental study of a numerical aperture for multimode PCS fiber optics using an imaging technique," *Chinese Phys. Lett.*, 2012.

[105]   D.-C. Chen, "Research of the measuring technique of numerical aperture of optical fiber using near infrared light," *Microw. Opt. Technol. Lett.*, vol. 50, no. 3, pp. 582–584, 2008.

[106]   M. A. Bandrés and J. C. Gutiérrez-Vega, "Ince-Gaussian beams," *Opt. Lett.*, 2004.

[107]   D. Meschede, *Optics, Light and Lasers: The Practical Approach to Modern Aspects of Photonics and Laser Physics: Second Edition*. 2008.

[108]   E. Cuche, F. Bevilacqua, and C. Depeursinge, "Digital holography for quantitative phase-contrast imaging," *Opt. Lett.*, 1999.

[109]   A. Anand, V. K. Chhaniwal, and B. Javidi, "Real-time digital holographic microscopy for phase contrast 3D imaging of dynamic phenomena," *IEEE/OSA J. Disp. Technol.*, 2010.

[110]   T. Colomb *et al.,* "Polarization microscopy by use of digital holography: application to optical-fiber birefringence measurements," *Appl. Opt.*, 2005.

[111]   B. Kemper and G. von Bally, "Digital holographic microscopy for live cell applications and technical inspection," *Appl. Opt.*, 2008.

[112]   J. F. Restrepo and J. Garcia-Sucerquia, "Automatic three-dimensional tracking of particles with high-numerical-aperture digital lensless holographic microscopy," *Opt. Lett.*, 2012.

[113]   M. H. Jericho, H. J. Kreuzer, M. Kanka, and R. Riesenberg, "Quantitative phase and refractive index measurements with point-source digital in-line holographic

microscopy," *Appl. Opt.*, 2012.

[114] P. Petruck, R. Riesenberg, and R. Kowarschik, "Optimized coherence parameters for high-resolution holographic microscopy," *Appl. Phys. B Lasers Opt.*, 2012.

[115] X. Su and W. Chen, "Reliability-guided phase unwrapping algorithm: A review," *Opt. Lasers Eng.*, 2004.

[116] S. Grilli, P. Ferraro, S. De Nicola, A. Finizio, G. Pierattini, and R. Meucci, "Whole optical wavefields reconstruction by Digital Holography," *Opt. Express*, 2009.

[117] E. Sánchez-Ortiga, P. Ferraro, M. Martínez-Corral, G. Saavedra, and A. Doblas, "Digital holographic microscopy with pure-optical spherical phase compensation," *J. Opt. Soc. Am. A*, 2011.

[118] B. Patiño-Jurado, J. F. Botero-Cadavid, and J. García-Sucerquia, "ANALYSIS OF THE DEPENDENCE OF THE NUMERICAL APERTURE ON CONE ANGLE IN A TAPERED STEP-INDEX OPTICAL FIBER," 2018.

Appendix A: Modeling Instructions for ray tracing study of cone-shaped optical fibers

In COMSOL Multiphysics™ software:

I. OPEN A NEW PROJECT

1. From the **File** menu, choose **New**.
2. In the **New** window, click **Model Wizard**.
3. In the **Model Wizard** window, click **3D**.
4. In the **Select Physics** tree, select **Optics->Ray Optics->Geometrical Optics (gop).**
5. Click **Add**.
6. Click **Study**.
7.   In the **Select Study** tree, select **Preset Studies-> Ray Tracing**.
8. Click **Done**.

II. PARAMETERS

1. In the Model **Builder window**, under **Global Definitions** click **Parameters.**
2. Type the following data:

Name	Expression	Description
wl 0.633[um]	0.633[um]	Wavelength
rcor	2.5[um]	Core radius
rcla	62.5[um]	Cladding Radius
ncl	1.45804	Refractive index Claddi
ncor	1.46147	Refractive index Core
alpha	45[deg	Cone semi-semiangle
conelencla	rcla/(tan(alpha))	height conical cladding
conelenco	rcor/(tan(alpha))	height conical core

II. GEOMETRY

1.   In the Model **Builder window**, under **Component 1 (comp1)** click **Geometry 1**.

2.   In the **Settings** window for **Geometry**, locate the Units section.

3.   From the **Length unit** list, choose **mm**.

4.   **Cylinder (cyl)**

   4.1 In the Geometry toolbar, click **Primitives** and choose **Cylinder**.

   4.2 In the **Settings** window for **Cylinder**, locate the **Size and Shape** section.

   4.3 In the **Radius** text field, type *rcor*.

   4.4 In the **Height** text field, type *1*.

   4.5 From the **Axis type** index list, choose **y-axis**.

   4.6 Right-click **Cylinder (cyl1)** and choose **Build Selected**.

   4.7 Add 5 cylinders with the following size and shape:

Cylinder	Radius	Height	x	y	z
(cyl2)	rcla	1	0	0	0
(cyl3)	rcor	1	0	0	0
(cyl4)	rcor	conelencla	0	- conelencla	0
(cyl5)	0.3	0.52	0	1	0
(cyl6)	1	Conelencore+0.5	0	-conelencla-conelenco-0.5	0

5.   **Cone (cone1)**

   5.1 In the Geometry toolbar, click **Primitives** and choose **Cone**.

   5.2 In the **Settings** window for **Cone**, locate the **Size and Shape** section.

   5.3 In the **Bottom Radius** text field, type *rcla*.

   5.4 In the **Height** text field, type *conelencl*.

   5.5 From the **Specify top size using** index list, choose **Radius**.

   5.6 In the **Top Radius** text field, type *rcor*.

   5.7 From the **Axis type** index list, choose **y-axis**.

   5.8 Right-click **Cone 1 (cone1)** and choose **Build Selected**.

6.   **Cone (cone2)**

   6.1 In the Geometry toolbar, click **Primitives** and choose **Cone**.

   6.2 In the **Settings** window for **Cone**, locate the **Size and Shape** section.

   6.3 In the **Bottom Radius** text field, type *rcor*.

   6.4 In the **Height** text field, type *conelenco*.

   6.5 From the **Specify top size using** index list, choose **Radius**.

   6.6 In the **Top Radius** text field, type *0*.

   6.7 From the **Axis type** index list, choose **y-axis**.

   6.8 Right-click **Cone 2 (cone2)** and choose **Build Selected**.

7.   **Rotate 1 (rot1)**

      7.1 In the Geometry toolbar, click **Transforms** and choose **Rotate**.

      7.2 In the **Settings** window for **Rotate**, locate the **Rotation Angle** section.

      7.3 In the **Rotation** text field, type 180

      7.4 . From the **Axis of rotation** index list, choose **x-axis**.

      7.5 Right-click **Rotate 1 (c1)** and choose **Build Selected**.

8. In the Geometry toolbar, click **Build All.**

III. MATERIALS

Material 1 (mat1)

1. In the **Model Builder** window, under **Component 1 (comp1)** right-click **Materials** and choose **Blank Material**.

2. In the **Settings** window for **Material**, type **Doped Silica Glass** in the **Label** text field.

3. Select Domains **5**, **6,** and **7**.

4. Click to expand the **Material Properties** section. In the **Material properties** tree, select **Electromagnetic Models->Refractive Index->Refractive index**, **real part (n).**

5. Click **Add to Material**.

6. Locate the **Material Contents** section. In the table, enter the following settings:

Property	value
Refractive index	ncor

Material 2 (mat2)

1. In the **Model Builder** window, under **Component 1 (comp1)** right-click **Materials** and choose **Blank Material**.

2. In the **Settings** window for **Material**, type **Pure Silica Glass** in the **Label** text field.

3. Select Domains **3** and **4**.

4. Click to expand the **Material Properties** section. In the **Material properties** tree, select **Electromagnetic Models->Refractive Index->Refractive index**, **real part (n).**

5. Click **Add to Material**.

6. Locate the **Material Contents** section. In the table, enter the following settings:

Property	value
Refractive index	ncl

Material 3 (mat2)

1. In the **Model Builder** window, under **Component 1 (comp1)** right-click **Materials** and choose **Blank Material**.

2. In the **Settings** window for **Material**, type **Air** in the **Label** text field.

3. Select Domains **1** and **2**.

4. Click to expand the **Material Properties** section. In the **Material properties** tree, select **Electromagnetic Models->Refractive Index->Refractive index**, **real part (n).**

5. Click **Add to Material**.

6. Locate the **Material Contents** section. In the table, enter the following settings:

Property	value
Refractive index	1

IV. GEOMETRICAL OPTICS (gop)

1. In the **Model Builder window**, under **Component 1 (comp1)** click **Geometrical Optics (gop)**.

2. In the **Settings** window for **Geometrical Optics**, locate the **Ray Properties** section.

3. From the **Intensity Computation** index list, choose **Using curvature tensor and ray power.**

4. **Ray Properties 1**

    4.1 In the **Model Builder window**, under **Component 1 (comp1)** click **Geometrical Optics (gop)** and click **Ray Properties 1.**

    4.2 In the **Settings** window for **Ray Properties 1,** locate the **Ray Properties** section.

    4.3 From the **Ray property specification** list, choose **Specify vacuum wavelength**.

    4.4 In the **Vacuum wavelength** text field, type w*l*

5. **Release from Grid 1**

    5.1 In the **Model Builder window**, under **Component 1 (comp1)** right-click **Geometrical Optics (gop)** and choose **Release from the Grid.**

5.2 In the **Settings** window for **Release from the Grid 1,** locate the **Initial Coordinates** section.

5.3 In the **Grid Type** $q_{y,0}$ text field, type 1,0125.

5.4 Locale the **Ray Direction Vector** section and from the **Ray direction vector** list, choose **conical**.

5.5 In the **Number of rays in wave vector space** text field, type 20000.

5.6 In the **Cone axis vector r** text fields, type **x**=0, **y**=1, **z**=0.

5.7 Locale the **Source Power** section and in **Psrc** text field, type 4 [mW].

6 **Accumulator 1**

6.1 In the **Model Builder window**, under **Component 1 (comp1)** right-click **Geometrical Optics (gop)** and choose **Accumulator.**

6.2 In the **Settings** window for **Accumulator 1,** locate the **Accumulator Setting** section.

6.3 From **Accumulator over** list, choose Elements and time.

6.4 In the **Settings** window for **Accumulator 1,** locate the **Units** section.

6.5 From **Dependent variable quantity** list, choose Intensity (W/m^2).

V. MESH 1
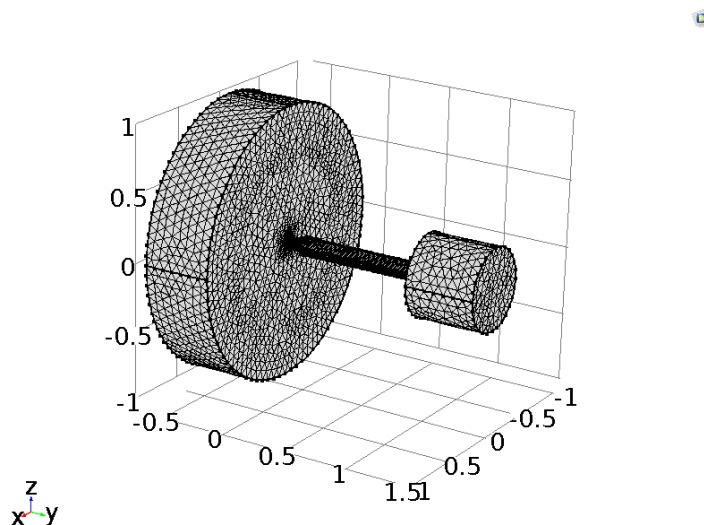
1. In the **Model Builder** window, under **Component 1 (comp1)** click **Mesh 1**.

2. In the **Settings** window for **Mesh**, locate the **Physics-Controlled Mesh** section.

3. From the **Element size** list, choose **Finer**.

4. Click **Build All.**

VI. STUDY 1

Step 1: Ray Tracing

1. In the **Model Builder** window, under **Study 1** click **Step 1: Ray Tracing**

2. In the **Settings** window for **Ray Tracing**, locate the **Study Settings** section.

3. Select the **Specify maximum path lenght** check box.

4. In the associated text field, type 0 6.

5. In the **Home toolbar**, click **Compute**.

VII. RESULTS

Cone shaped-Cone Semi-angle: 29 [deg] Spot Color: Intensity [W/m^2]
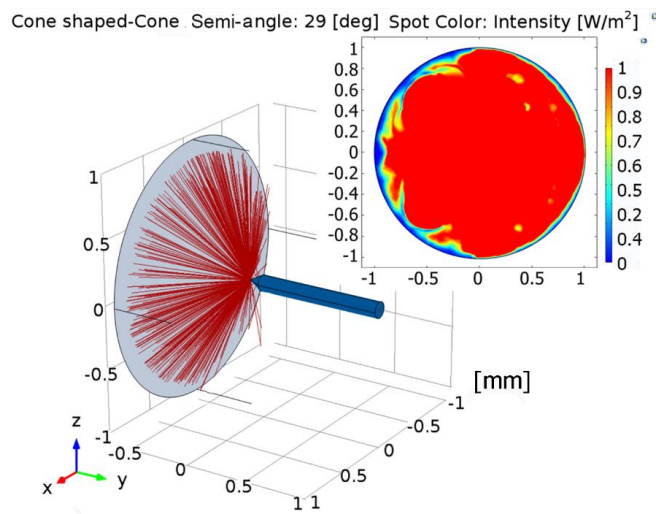
Ray Trajectories (gop)

1. In the **Model Builder** window, under **Results** right-click **Data Sets** and choose **Surface.**

2. In the **Setting** window for **Surface 1,** locate **Data** Section

3. From **Data set** index list, choose **Study 1/Solution 1.**

4. From **x- and y- axes** index list, choose **xz-plane.**

5. Locate the **Selection** section and choose **Manual** in the **Selection** index list.

6. Select the screen contour 3.

7. In the **Model Builder** window, right-click **Results** and choose **2D Plot Group.**

8. In the **Settings** window for **2D Plot Group**, locate the **Data section**.

9. From the **Data set** index list, choose **Surface 1.**

10. From the **Times (s)** index list, choose **Interpolation**

11. In the **Results** toolbar, click **Plot**.

Appendix B: Modeling Instructions for wave propagation study of cone-shaped fiber

In COMSOL Multiphysics™ software:

I. OPEN A NEW PROJECT

1. From the **File** menu, choose **New**.
2. In the **New** window, click **Model Wizard**.
3. In the **Model Wizard** window, click **3D**.
4. In the **Select Physics** tree, select **Optics->Wave Optics->Electromagnetic Waves, Beam Envelopes (ewbe).**
5. Click **Add**.
6. Click **Study**.
7. In the **Select Study** tree, select **Preset Studies-> Boundary Mode Analysis**.
8. Click **Done**.

II. PARAMETERS

1. In the Model **Builder window**, under **Global Definitions** click **Parameters.**
2. Type the following data:

Name	Expression	Description
wl 0.633[um]	0.633[um]	Wavelength
f0	c_const/wl	frequency free space wavelength
rcor	2.5[um]	Core radius
rcla	62.5[um]	Cladding Radius
ncl	1.45804	Refractive index Claddi
ncor	1.46147	Refractive index Core
alpha	45[deg	Cone semi-semiangle
conelencla	rcla/(tan(alpha))	height conical cladding
conelenco	rcor/(tan(alpha))	height conical core

II. GEOMETRY

1. In the Model **Builder window**, under **Component 1 (comp1)** click **Geometry 1**.

2. In the **Settings** window for **Geometry**, locate the Units section.

3. From the **Length unit** list, choose **mm**.

4. **Cylinder (cyl)**

    4.1 In the Geometry toolbar, click **Primitives** and choose **Cylinder**.

    4.2 In the **Settings** window for **Cylinder**, locate the **Size and Shape** section.

    4.3 In the **Radius** text field, type *rcor*.

    4.4 In the **Height** text field, type *1*.

    4.5 From the **Axis type** index list, choose **x-axis**.

    4.6 Right-click **Cylinder (cyl1)** and choose **Build Selected**.

    4.7 Add 4 cylinders with the following size and shape:

Cylinder	Radius	Height	x	y	z
(cyl2)	rcla	1	0	0	0
(cyl3)	rcor	1	0	0	0
(cyl4)	rcor	Conelencla-conelenco	1	0	0
(cyl5)	1	0.1	1+conelencla	1	0

5. **Cone (cone1)**

    5.1 In the Geometry toolbar, click **Primitives** and choose **Cone**.

    5.2 In the **Settings** window for **Cone**, locate the **Size and Shape** section.

    5.3 In the **Bottom Radius** text field, type *rcla*.

    5.4 In the **Height** text field, type *conelencl*.

    5.5 From the **Specify top size using** index list, choose **Radius**.

    5.6 In the **Top Radius** text field, type *rcor*.

    5.7 From the **Axis type** index list, choose **x-axis**.

    5.8 Right-click **Cone 1 (cone1)** and choose **Build Selected**.

6. **Cone (cone2)**

   6.1 In the Geometry toolbar, click **Primitives** and choose **Cone**.

   6.2 In the **Settings** window for **Cone**, locate the **Size and Shape** section.

   6.3 In the **Bottom Radius** text field, type *rcor*.

   6.4 In the **Height** text field, type *conelenco*.

   6.5 From the **Specify top size using** index list, choose **Radius**.

   6.6 In the **Top Radius** text field, type *0*.

   6.7 From the **Axis type** index list, choose **x-axis**.

   6.8 Right-click **Cone 2 (cone2)** and choose **Build Selected**.

7. In the Geometry toolbar, click **Build All.**

III. MATERIALS

Material 1 (mat1)

7. In the **Model Builder** window, under **Component 1 (comp1)** right-click **Materials** and choose **Blank Material**.

8. In the **Settings** window for **Material**, type **Doped Silica Glass** in the **Label** text field.

9. Select Domains **2, 4** and **6**.

10. Click to expand the **Material Properties** section. In the **Material properties** tree, select **Electromagnetic Models->Refractive Index->Refractive index**, **real part (n).**

11. Click **Add to Material**.

12. Locate the **Material Contents** section. In the table, enter the following settings:

Property	value
Refractive index	ncor

Material 2 (mat2)

7. In the **Model Builder** window, under **Component 1 (comp1)** right-click **Materials** and choose **Blank Material**.

8. In the **Settings** window for **Material**, type **Pure Silica Glass** in the **Label** text field.

9. Select Domains **1** and **3**.

10. Click to expand the **Material Properties** section. In the **Material properties** tree, select **Electromagnetic Models->Refractive Index->Refractive index**, **real part (n).**

11. Click **Add to Material**.

12. Locate the **Material Contents** section. In the table, enter the following settings:

Property	value
Refractive index	ncl

Material 3 (mat2)

7. In the **Model Builder** window, under **Component 1 (comp1)** right-click **Materials** and choose **Blank Material**.

8. In the **Settings** window for **Material**, type **Air** in the **Label** text field.

9. Select Domain **5** only.

10. Click to expand the **Material Properties** section. In the **Material properties** tree, select **Electromagnetic Models->Refractive Index->Refractive index**, **real part (n).**

11. Click **Add to Material**.

12. Locate the **Material Contents** section. In the table, enter the following settings:

Property	value
Refractive index	1

IV. ELECTROMAGNETIC WAVES, BEAM ENVELOPES (EWBE)

1. In the **Model Builder window**, under **Component 1 (comp1)** click **Electromagnetic Waves, Beam Envelopes (ewbe)**.

2. In the **Settings** window for **Electromagnetic Waves**, **Beam Envelopes (ewbe)**, locate the **Port Sweep Setting** section.

3. Clear the Enable check box.

4. **Wave Equation, Beam Envelopes 1**

   4.1 In the **Model Builder** window, under **Component 1 (comp1)>Electromagnetic Waves, Beam Envelopes (emw)** click **Wave Equation, Beam Envelopes 1.**

   4.2 In the **Settings** window for **Wave Equation**, **Beam Envelopes**, locate the **Electric Displacement Field** section.

   4.3 From the **Electric displacement** field model list, choose **Refractive index**.

5. **Port 1**

   5.1 In the **Model Builder window**, under **Component 1 (comp1)** right-click **Electromagnetic Waves, Beam Envelopes (emw)** and choose **Port.**

   5.2 In the **Settings** window for **Port 1,** locate the **Bourdary Selection** section.

   5.3 Select boundaries **1** and **4**.

   5.4 In the **Settings** window for **Port 1,** locate the **Port Properties** section.

   5.5 From **Type of port** list, choose Numeric.

   5.6 From **Wave excitation at this port** list, choose on.

   5.7 In the **Port input power** text field, type *4 [mW]*.

   5.8 Right-click **Port 1** and choose **duplicate.**

6. **Port 2**

   6.1 In the **Model Builder window**, under **Component 1 (comp1)** right-click **Electromagnetic Waves, Beam Envelopes (emw)** and choose **Port.**

   6.2 In the **Settings** window for **Port 2,** locate the **Bourdary Selection** section.
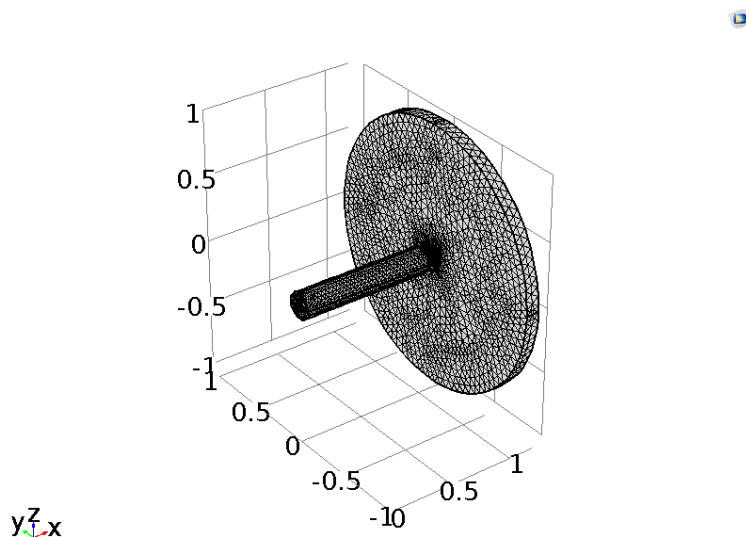
   6.3 Select the screen (**Boundary 31)**.

   6.4 In the **Settings** window for **Port 2,** locate the **Port Properties** section.

   6.5 From **Type of port** list, choose Numeric.

   6.6 From **Wave excitation at this port** list, choose off.

   6.7 Right-click **Port 1** and choose **duplicate.**

V. MESH 1

5. In the **Model Builder** window, under **Component 1 (comp1)** click **Mesh 1**.

6. In the **Settings** window for **Mesh**, locate the **Physics-Controlled Mesh** section.

7. From the **Element size** list, choose **Finer**.

8. Click **Build All.**

VI. STUDY 1

Step 1: Boundary Mode Analysis

1. In the **Model Builder** window, under **Study 1** click **Step 1: Boundary Mode Analysis**.

2. In the **Settings** window for **Boundary Mode Analysis**, locate the **Study Settings** section.

3. In **Port Name** text field, type 1.

4. In the **Search for modes around** text field, type 1.4507.

5. In the **Mode analysis frequency** text field, type *f0.*

6. Right-click in **Step 1: Boundary Mode Analysis and choose duplicate**

7. Click **Step 2: Boundary Mode Analysis**.

8. In **Port Name** text field, type 2.

9. In the **Search for modes around** text field, type 1.4505.
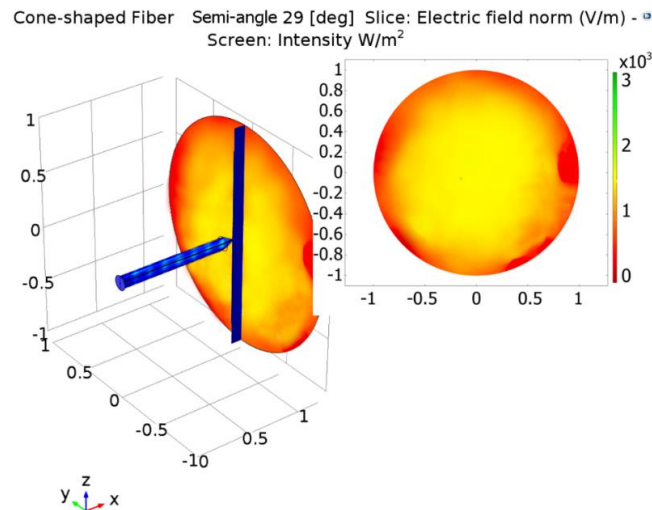
Step 3: Boundary Mode Analysis

1. In the **Model Builder** window, under **Study 1** click **Step 1: Boundary Mode Analysis**.

2. In the **Settings** window for **Boundary Mode Analysis**, locate the **Study Settings** section.

3. In **Port Name** text field, type 3.

4. In the **Search for modes around** text field, type 1.4507.

5. In the **Mode analysis frequency** text field, type *f0.*

6. Right-click in **Step 3: Boundary Mode Analysis and choose duplicate**

7. Click **Step 2: Boundary Mode Analysis**.

8. In **Port Name** text field, type 4.

9. In the **Search for modes around** text field, type 1.4505.

Step 5: Frequency Domain

1. In the **Model Builder** window, under **Study 1** click **Step 5: Frequency Domain**.

2. In the **Settings** window for **Frequency Domain**, locate the **Study Settings** section.

3. From the **Frequency unit** index list, choose Hz

4. In **Frequencies** text field, type f0.

5. In the **Home toolbar**, click **Compute**.

VII. RESULTS

Cone-shaped Fiber   Semi-angle 29 [deg]   Slice: Electric field norm (V/m) - ⊡
Screen: Intensity W/m²

Beam Envelopes (emw)

1. In the **Model Builder** window, under **Results** right-click **Data Sets** and choose **Surface.**

2. In the **Setting** window for **Surface 1,** locate **Data** Section

3. From **Data set** index list, choose **Study 1/Solution 1.**

4. From **x- and y- axes** index list, choose **xz-plane.**

5. Locate the **Selection** section and choose **Manual** in the **Selection** index list.

6. Select the screen boundary 31.

7. In the **Model Builder** window, right-click **Results** and choose **2D Plot Group.**

8. In the **Settings** window for **2D Plot Group**, locate the **Data section**.

9. From the **Data set** index list, choose **Surface 1.**

10. From the **eigenvalue** index list, choose **1.4444.**

11. In the **Expression** text field, type (3*10^8)*8.85*(10^(-12))*(ewbe.normE^2).

12. In the **Unit** text field, type W/m^2.

13. In the **Results** toolbar, click **Plot**.